

# POLITECNICO DI TORINO

Master's Degree  
in  
Nanotechnologies for ICTs



## Layered Double Hydroxides used as room temperature gas sensors for the detection of Volatile Organic Compounds

Supervisor

Dr. Matteo Cocuzza

Candidate

Arianna Nigro

Co-supervisors

Dr. Simone Marasso

Dr. Alessio Verna

Dr. Lorenzo Vigna

DECEMBER 2020



# Acknowledgements

I would like to thank my tutors, Prof. Matteo Cocuzza, Dr. Simone Marasso, Dr. Alessio Verna and Dr. Lorenzo Vigna, for their invaluable help. Despite the difficulties encountered at the beginning of this work, they guided me to reach the best possible results. I am also thankful to the whole Chilab staff, for the support provided during my experience in the laboratory.

I am truly grateful to my family, my parents, Franco e Angela, and my brother, Andrea, for having given me the chance to chase my dreams.

Thanks to all my friends, the old ones which continued to be by my side after all this time, and the new ones, which shared with me a great part of this journey.

As last, I would like to mention Marco. No words could ever explain what he did for me.

# Table of Contents

List of Tables	6
List of Figures	7
<b>1 Introduction to the project</b>	<b>14</b>
1.1 The electronic nose . . . . .	14
1.2 Thesis Content . . . . .	20
<b>2 Gas Sensors Overview</b>	<b>21</b>
2.1 Performance parameters . . . . .	21
2.2 Classes of gas sensor devices . . . . .	25
2.2.1 Conductivity sensors . . . . .	26
2.2.1.1 Conducting Polymer Composite Sensors . . . . .	27
2.2.1.2 Intrinsically Conducting Polymers . . . . .	30
2.2.1.3 Metal Oxide Sensors . . . . .	32
2.2.1.4 Micro-heater . . . . .	38
2.2.2 Capacitive sensors . . . . .	40
2.2.3 Piezoelectric sensors . . . . .	41
2.2.3.1 Quartz Crystal Microbalance sensors . . . . .	42
2.2.3.2 Surface Acoustic Wave sensors . . . . .	43
2.2.4 Optical sensors . . . . .	45
2.2.4.1 Surface Plasmon Resonance (SPR) sensors . . . . .	45
2.2.4.2 Fluorescent sensors . . . . .	45
2.2.5 Potentiometric sensors . . . . .	46
2.2.5.1 MOSFET sensors . . . . .	46
2.2.6 Calorimetric sensors . . . . .	50
2.2.6.1 Pyroelectric sensors . . . . .	51
2.2.6.2 Pellistor sensors . . . . .	51
2.2.7 Amperometric sensors . . . . .	51
2.2.8 Analytical approaches . . . . .	53
2.2.8.1 Mass Spectrometry . . . . .	53

2.2.8.2	Ion Mobility Spectrometry . . . . .	53
2.2.8.3	Gas Chromatography . . . . .	53
2.2.8.4	Infrared Spectroscopy . . . . .	54
<b>3</b>	<b>Layered Double Hydroxides</b>	<b>55</b>
3.1	Synthesis of Layered Double Hydroxides . . . . .	57
3.2	Properties of the LDH structure . . . . .	60
3.2.1	Cation and anion ordering . . . . .	60
3.2.2	Cation-Anion interactions . . . . .	61
3.2.3	Thermal Stability . . . . .	62
3.2.4	Electronic properties . . . . .	63
3.3	Morphology of LDH . . . . .	64
3.3.1	Size and Shape . . . . .	64
3.3.2	Specific Surface Area and Porosity . . . . .	69
3.4	Sensing Mechanism . . . . .	70
3.5	Applications of LDH . . . . .	73
<b>4</b>	<b>Development of LDH based gas sensors</b>	<b>77</b>
4.1	Deposition of the sensing layer . . . . .	77
4.1.1	Preparation of the solution . . . . .	78
4.1.2	Drop Casting . . . . .	78
4.1.3	Spin coating . . . . .	79
4.1.4	Ink-jet printing . . . . .	80
4.1.5	Spray coating . . . . .	83
4.1.6	Dissolution of Layered Double Hydroxides . . . . .	84
4.2	Characterization techniques . . . . .	86
4.2.1	Scanning Electron Microscopy and Transmission Electron Microscopy . . . . .	86
4.2.2	X-Ray Powder Diffraction and Fourier Transform Infrared Spectroscopy . . . . .	88
4.2.3	X-ray Photoelectron Spectroscopy . . . . .	89
4.3	Design and optimization of the sensor . . . . .	90
4.3.1	Improved design of IDE sensor . . . . .	97
4.4	Fabrication process . . . . .	104
4.4.1	Electrodes fabrication . . . . .	104
4.4.2	Dispersion of LDH powders and drop-casting of the solution	108
4.4.3	Structure characterizations . . . . .	109
<b>5</b>	<b>Gas Sensing Measurements</b>	<b>117</b>
5.1	Sensing Setup . . . . .	117
5.2	Discussion of results . . . . .	118

5.2.1	Sensor 1 - ZnAl-Cl LDH . . . . .	119
5.2.2	Sensor 2 - ZnFe-Cl LDH . . . . .	121
5.2.3	Sensor 3 - ZnAl-NO <sub>3</sub> LDH . . . . .	126
5.2.4	Sensor 4 - MgAl-NO <sub>3</sub> LDH . . . . .	126
<b>6</b>	<b>Conclusions and future works</b>	<b>130</b>
<b>A</b>	<b>Supplementary figures</b>	<b>132</b>
	<b>Bibliography</b>	<b>140</b>

# List of Tables

3.1	Summary of the influence of various parameters on the size of particles during LDH growth. . . . .	66
4.1	Geometrical parameters of the designed sensor. . . . .	96
4.2	Summary of the dispersions of LDHs realized with ethanol. . . . .	108
4.3	Data from the FTIR spectra. . . . .	112
4.4	XPS quantitative results for the analysed samples. . . . .	114
4.5	EDX quantitative results for the analysed samples. . . . .	116
5.1	Summary of the performance parameters of the tested sensors. They refer to the case of 10% concentration of the analyte. When the sensor was sensitive to more than one VOC, as in the case of ZnFe-Cl, only the values related to the best achieved performance were reported.	119

# List of Figures

1.1	Schematic representation of the human olfactory system [4]. . . . .	16
1.2	Similarities between an electronic nose and a human nose for the identification of ododrants [5]. . . . .	18
1.3	Examples of applications of electronic noses in different fields [13].	19
2.1	Sensor response to a gas pulse [17]. . . . .	22
2.2	Schematic representation of a response curve for a chemiresistive gas sensor, showing response and recovery time [14]. . . . .	24
2.3	Summary of the main categories of gas sensors, together with their main properties (MOS - metal oxide semiconductor; QCM - quartz crystal microbalance; SAW - surface acoustic wave; MOSFET - metal oxide semiconductor field effect transistor; SPR - surface plasmon resonance) [17]. . . . .	26
2.4	Summary of some examples of commercial e-noses realized with different types of gas sensors (CP - conducting polymer; IR - infra red; GC - gas chromatography; FO - fibre optic; ANN - artificial neural network; DC - distance classifiers; PCA - principal component analysis; DFA - discriminant function analysis; CA - cluster analysis; DA - discriminant analysis) [1]. . . . .	27
2.5	Example of the structure of a typical conductivity sensor [1]. . . . .	28
2.6	Schematic representation of the structure and swelling mechanism of CP composites [19]. . . . .	28
2.7	Example of a CP composite sensor obtained exploiting bulk micro-machining [21]. . . . .	29
2.8	Conducting Polymer composite sensors characterized by carbon-black polymer as sensing material [21], [19]. . . . .	30
2.9	Chemical structures of different ICPs [20]. . . . .	30
2.10	Formation mechanism of electronic core-shell structure in a n-type oxide semiconductor [22]. . . . .	33
2.11	(a) Gas sensing mechanism and (b) equivalent circuit of a n-type MOS sensor [22]. . . . .	33

2.12	Formation mechanism of the electronic core-shell structure in a p-type oxide semiconductor [22]. . . . .	34
2.13	(a) Gas sensing mechanism and (b) equivalent circuit of a p-type MOS sensor [22]. . . . .	35
2.14	Schematic representation of a SnO <sub>2</sub> sensor in a tube type configuration. The sensing material is deposited around a ceramic tube. A heater runs through the center of the tube and electrical contacts are provided at both ends [20]. . . . .	36
2.15	Schematic representation of a micro-hotplate in a (a) vertical and (b) horizontal approach [25]. . . . .	38
2.16	Schematic representation of the steps involved in the fabrication of a micro-hotplate: (a) starting Si substrate coated by SiN on both sides, (b) SiN patterning, (c) Si anisotropic etching, (d) heater deposition and patterning, (e) SiO <sub>2</sub> insulating layer deposition and patterning, (f) deposition of bonding pads and electrical contacts, (g) sensing material integration [26]. . . . .	40
2.17	Sensing mechanism of a capacitive sensor. Two states are represented: (a) no analyte molecules are present in the sensing material, (b) analyte molecules diffuse in the sensing material [17]. . . . .	41
2.18	Schematic representation of a QCM sensor [30]. . . . .	42
2.19	Schematic of a SAW sensor in (a) delay line and (b) resonator configurations [31]. . . . .	44
2.20	Representation of a fluorescent sensor realized through an optical fiber [1]. . . . .	46
2.21	Schematic representation of a GASFET [1]. . . . .	48
2.22	Schematic representation of a OGFET [32]. . . . .	49
2.23	Schematic representation of a ISFET [32]. . . . .	50
2.24	Schematic representation of a CHEMFET [32]. . . . .	50
2.25	Schematic representation of an amperometric sensor [17]. . . . .	52
3.1	Representation of the LDH structure. The present example involves Zn <sup>2+</sup> and Al <sup>3+</sup> as cations and Cl <sup>-</sup> as the intercalated anion. It is possible to notice the central metallic atoms surrounded by the hydroxyl groups shaping the various lamellas and the repetition of lamellas forming the overall LDH structure. As an addition, the cell parameters (here named a and c) are indicated [38]. . . . .	56
3.2	Arrangement of water molecules and carbonate (a) or sulphate (b and c) anions in the interlayers. OH represent the hydroxyl groups of lamellas and O are oxygens of interlayer anions. Dotted lines represent the hydrogen bonding net in the interlayers [44]. . . . .	61

3.3	TGA curve of MgAl-LDH synthesised through coprecipitation (sample 1) and hydrothermal (sample 2) methods [46]. . . . .	62
3.4	Schematic representation of a) flat-lying configuration b) stick-lying configuration [47]. . . . .	63
3.5	Band diagram of LDHs with different compositions. The dashed blue line represents the Fermi level [49]. . . . .	65
3.6	SEM images showing the comparison between LDH obtained through coprecipitation, induced hydrolysis and urea method. In detail: a) $Cu_2Cr(OH)_6Cl \cdot 2H_2O$ prepared by $CuO/CrCl_3$ induced hydrolysis, b) $Cu_2Cr(OH)_6Cl \cdot 2H_2O$ prepared by coprecipitation, c) $Mg_2Al(OH)_6(CO_3)_{0.5} \cdot 2H_2O$ prepared by coprecipitation, d) $Mg_2Al(OH)_6(CO_3)_{0.5} \cdot 2H_2O$ prepared by urea method [39]. . . . .	67
3.7	SEM images showing the effects on the particle size of a) aging time and b) reaction temperature on LDH synthesized by hydrothermal method. [50]. . . . .	67
3.8	SEM images showing the effects on the particle size of a) aging time and b) concentration of metal ions on LDH synthesized by urea method [50]. . . . .	68
3.9	SEM images of LDH structures having a) too low molar ratio b) optimal molar ratio c) too high molar ratio [37] . . . . .	71
3.10	Formation mechanism for the 3D hierarchical flower-like MgAl LDH [55]. . . . .	72
3.11	Schematic of gas sensing mechanism of $NO_2$ for CoAl-LDH sensor and related response curve [56]. . . . .	73
3.12	Different approaches for the development of LDH-based catalysts [57].	74
4.1	Schematic representation of a drop casting process [67]. . . . .	79
4.2	Schematic representation of a spin-coating deposition process [68]. . . . .	80
4.3	Schematic representation of the different categories of DOD ink-jet: a) thermal, b) piezoelectric, c) electrostatic [69]. . . . .	81
4.4	Schematic representation of the working principle of a piezoelectric DOD ink-jet printer [71]. . . . .	82
4.5	Pattern of the material to be deposited over the IDE structure. . . . .	83
4.6	Shadow mask employed in spray coating deposition realized through CleWin5 software. . . . .	85
4.7	Schematic representation of the dissolution mechanism of LDHs occurring at low pH [84]. . . . .	86
4.8	SEM (a) and TEM (b) images of NiFeAl LDHs. The first shows the morphology of the material with varying $M^{2+}/M^{3+}$ contents. The second shows the structure of nanopetals at different magnifications [65]. . . . .	87

4.9	XRD patterns of (a) NiAl and NiFeAl LDH [65] and (b) CoAl LDH [56]. . . . .	88
4.10	FTIR spectra of (a) NiAl and NiFeAl LDH [65] and (b) CoAl LDH [56]. . . . .	89
4.11	XPS spectra of NiZnAl LDH corresponding to (a) Ni 2p, (b) Zn 2p, (c) Al 2p and O1 s (d-f) [59]. . . . .	90
4.12	Schematic representation of IDEs with all their relevant parameters [92], [91]. . . . .	91
4.13	Efficiency (a) and optimization (b) parameters for a squared layout.	93
4.14	Efficiency (a) and optimization (b) parameters as function of the horizontal dimension variation when $W = G$ . . . . .	94
4.15	Efficiency (a) and optimization (b) parameters as function of the vertical dimension variation when $W = G$ and $N = 100$ . . . . .	95
4.16	Representation of an IDE characterized by (a) squared layout, (b) layout in which the vertical dimension is enhanced with respect to the horizontal one. In both cases the width of the gap corresponds to that of the electrodes. . . . .	95
4.17	Representation of the IDE (Option 2) with its dimensions. . . . .	96
4.18	Schematic representation of IDEs having rounded corners [91] . . . .	97
4.19	Efficiency (a) and optimization (b) parameters for a squared layout with rounded concave corners. . . . .	98
4.20	Efficiency (a) and optimization (b) parameters as function of the horizontal dimension variation when $W = G$ for a layout with rounded concave corners. . . . .	98
4.21	Efficiency (a) and optimization (b) parameters as function of the vertical dimension variation when $W = G$ and $N = 100$ for a layout with rounded concave corners. . . . .	99
4.22	Comparison of the efficiency (a) and optimization (b) parameters as function of the horizontal dimension variation when $W = G$ and $N = 100$ between the optimized IDE and the layout with rounded concave corners. . . . .	99
4.23	Schematic representation of an electrode with a spiral layout. . . . .	100
4.24	Efficiency (a) and optimization (b) parameters with varying number of fingers when $W$ and $G$ are fixed to $22.6 \mu m$ . . . . .	101
4.25	Efficiency (a) and optimization (b) parameters with increasing horizontal dimension $X$ when $W$ and $G$ are fixed to $22.6 \mu m$ . . . . .	101
4.26	Efficiency (a) and optimization (b) parameters as function of the horizontal dimension $X$ . For the optimized IDE, $Y = 4.5 \text{ mm}$ , while for the other options $X = Y$ . In all the three cases, $W$ and $G$ are fixed to $22.6 \mu m$ . . . . .	102

4.27	Comparison between the resistance of the electrodes for a spiral layout and an optimized IDE layout with increasing X dimension when the electrode thickness is set to 100 nm. . . . .	102
4.28	Comparison between the spiral layout with 90° corners and the layout with round corners of efficiency (a) and optimization (b) parameters as function of the horizontal dimension X. . . . .	103
4.29	Virtual mask for the direct laser writing process obtained through CleWin5 software. . . . .	106
4.30	Details of the sensors' pattern on the mask: (a) whole device and (b) zoom on a portion of the IDEs . . . . .	106
4.31	Schematic representation of the steps involved in the fabrication of the device. . . . .	107
4.32	Schematic representation of the array composed by 2 sensors. . . . .	108
4.33	PDMS mold employed to selectively deposit the LDH solution over the active area of the device. . . . .	109
4.34	FESEM images of (a),(b) ZnAl-Cl LDH, (c),(d) ZnFe-Cl LDH and (e),(f) ZnAl-NO <sub>3</sub> LDH. . . . .	110
4.35	FTIR spectrum of the four LDH compositions. . . . .	111
4.36	XPS spectra of the four different LDH compositions. . . . .	113
4.37	EDX spectra of the four different LDH compositions. . . . .	115
5.1	Schematic representation of the setup employed for the gas sensing measurements [97]. . . . .	118
5.2	(a) Real-time response of the sensors to 10% of ammonia vapours. (b) Sensitivity vs Concentration. (c) Response/Recovery time vs Concentration. (d) Three response cycles of the ZnAl-Cl-based sensor to 10% ammonia vapours. . . . .	120
5.3	(a) Real-time response of the sensors to 10% of acetone vapours. (b) Sensitivity vs Concentration. (c) Response/Recovery time vs Concentration. . . . .	122
5.4	(a) Real-time response of the sensors to 10% of ethanol vapours. (b) Sensitivity vs Concentration. (c) Response/Recovery time vs Concentration. (d) Three response cycles of the ZnFe-Cl-based sensor to 10% of ethanol vapours. . . . .	123
5.5	(a) Real-time response of the sensors to 10% of ammonia vapours. (b) Sensitivity vs Concentration. (c) Response/Recovery time vs Concentration. . . . .	124
5.6	(a) Real-time response of the sensors to 10% of chlorine vapours. (b) Sensitivity vs Concentration. (c) Response/Recovery time vs Concentration. . . . .	125

5.7	(a) Real-time response of the sensors to 10% of ammonia vapours. (b) Sensitivity vs Concentration. (c) Response/Recovery time vs Concentration. (d) Three response cycles of the ZnAl-NO <sub>3</sub> -based sensor to 10% ammonia vapours. . . . .	127
5.8	(a) Real-time response of the sensor to 10% of acetone vapours. (b) Sensitivity vs Concentration. (c) Response/Recovery time vs Concentration. (d) Three response cycles of the MgAl-NO <sub>3</sub> -based sensor to 10% acetone vapours. . . . .	128
5.9	Selectivity results of the 4 LDH-based sensors to acetone, ethanol, ammonia and chlorine vapours at 10% concentration. . . . .	129
A.1	Details of the gap distance and of the width of IDE fingers after the lift off process. . . . .	132
A.2	Images of the sensor at the end of the fabrication process. The LDH layers, as mentioned, are deposited only over the IDEs. . . . .	133
A.3	Experimental setup of the gas sensing system employed to test the response of the LDH-based sensors. . . . .	134
A.4	Real-time response curves for Sensor 1 (ZnAl-Cl LDH) to ammonia vapours at (a) 2%, (b) 4%, (c) 6% and (d) 8% concentration. . . . .	135
A.5	Real-time response curves for Sensor 2 (ZnFe-Cl) to (a) acetone and (b) ethanol at 8% concentration. . . . .	136
A.6	Real-time response curves for Sensor 2 (ZnFe-Cl) to ammonia vapours at (a) 2%, (b) 4%, (c) 6% and (d) 8% concentration. . . . .	137
A.7	Real-time response curves for Sensor 2 (ZnFe-Cl) to chlorine vapours at (a) 6% and (b) 8% concentration. . . . .	138
A.8	Real-time response curves for Sensor 3 (ZnAl-NO <sub>3</sub> ) to ammonia vapours at (a) 6% and (b) 8% concentration. . . . .	138
A.9	Real-time response curves for Sensor 4 (MgAl-NO <sub>3</sub> ) to acetone vapours at (a) 6% and (b) 8% concentrations. . . . .	139



# Chapter 1

## Introduction to the project

### 1.1 The electronic nose

In the past decades, attempts to implement technologies to reproduce human senses have gained a great interest, both from the research world and market companies, which recognise their promising applications. Nowadays, there exist different devices able to emulate all the human senses, like electronic tongues (e-tongues), electronic eyes (e-eyes) or electronic noses (e-noses).

The human nose has been used as an analytical tool in many industrial applications, to evaluate the smell of products and so to assess their quality. This process is carried out by using human sensory panels, where a group of people fills out questionnaires about the smells associated with the analysed substances, but the outcome is extremely subjective, since the sense of smell, is highly mysterious and complex being strictly linked to memories and emotions [1].

As a first improvement to this technique, gas chromatography (GC) and mass spectrometry (MS) have been employed, to help human panels in the quality evaluation of products through odour analysis, leading to more consistent results. However, these techniques are time-consuming, expensive and relatively slow, so not suitable for real-time analysis [2].

The solution to these limitations can be found through the implementation of an electronic nose based on gas sensors.

The first attempts in the development of an instrumentation capable of detecting odours dates back to 1961 with Moncrieff, but this was a mechanical nose, while the first electronic implementations were reported by Wilkens and Hatman in 1964, based on redox reactions of odorants at an electrode, Buck et al., with a modulation of conductivity by odorants and Dravieks and Trotter, with a modulation of contact potential by odorants, both in 1965. However, the concept of an e-nose as an intelligent chemical array sensor system for the detection and classification of

odorants only emerged in 1982 with Persaud and Dodd [3]. The term electronic nose, was not easily defined, but a specific definition was associated to this type of device:

*An electronic nose is an instrument, which comprises an array of electronic chemical sensors with partial specificity and an appropriate pattern-recognition system, capable of recognising simple or complex odours [3].*

This definition therefore places the architecture of the electronic nose in the field of gas sensing for the detection of individual components or mixtures of gases (details about gas sensors are provided in Chapter 2).

The basic idea behind the implementation of an e-nose is the attempt to mimic the way in which humans smell. The first step in the process of human perception of odours is sniffing, consisting in the motion of air samples containing odorant molecules past curved bony structures in the nose, called turbinates. The turbinates generate turbulent airflow patterns that carry the mixture of volatile organic compounds (VOCs) to a thin mucus layer which coats the olfactory epithelium, where the sensory cells responsible for the detection of odorants are located. VOCs pass through the mucus membrane and get immediately trapped by mucus so they start diffusing to the epithelium. The sensory cells located on this last layer are covered by cilia structures, with receptors placed on the outer membranes. These cells are specialized neurons, which get replicated every 20-30 days. VOCs can reach the olfactory epithelium either in gaseous form or as a coating on the particles that fill the air we breathe, both from the nostrils and from the mouth when food is chewed [2].

As soon as the gas molecule binds to a receptor protein, it is transformed into an odor, inducing a cascade of enzymatic reactions which involve the depolarization of the membrane of the cell. The sensory cells in the epithelium respond through the transmission of signals along axons, considered as neural "wires", which arrive up to the brain's olfactory system and terminate in a cluster of neural networks called glomeruli. Glomeruli represent the first level of central odor information processing. All sensory neurons which contain a specific odorant receptor tend to converge on two or three glomeruli in the olfactory bulb. These neurons can respond to more than one odorant, so the olfactory quality is given by the pattern of response across multiple glomeruli. The final step consists in the processing of the olfactory information first at the hypothalamus and then at higher processing centers (fig.1.1) [2].

Starting from analogies with the human nose, the electronic nose is characterized by three functional components, operating serially on an odorant sample: a sample handler, an array of gas sensors and a signal-processing system. Its output can

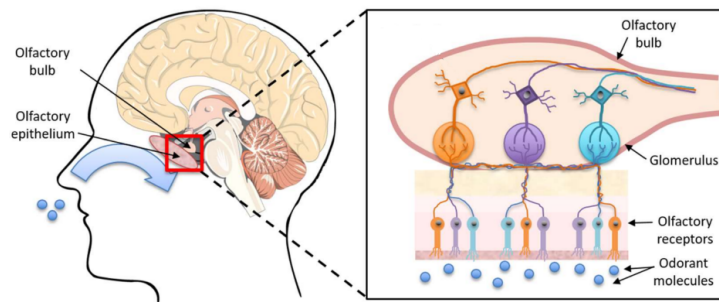


**Figure 1.1:** Schematic representation of the human olfactory system [4].

either be the identity of an odorant, an estimate of the concentration of an odorant or the characteristic properties of the odor as they are perceived by a human. As in the human nose each receptor is characterized by a different sensitivity to different odorants, each sensor in the array of an e-nose behaves in the same way, and it is just the pattern response across sensors which allows the system to identify an odor [2].

In a typical electronic nose, the array of sensors is located in a small chamber which gets filled by an air sample. The sample-handling unit exposes the sensors to the odorant, producing a response as the odorant molecules interact with the active material of the sensors, according to its specific transduction mechanism (see Chapter 2 for details). A steady-state condition is reached after a certain time interval, and in this transient, the sensor's response is recorded and delivered to a signal-processing unit. Several cycles are performed by repeating these same steps, after an exposure of the sensor to a washing gas to remove the odorant mixture from the active material [2].

Signal processing and pattern recognition are the key features in an e-nose to identify the odorant sample and eventually estimate its concentration. However, prior to device operation, it is fundamental to compile a database of expected odorants. The two mentioned steps can be subdivided in four sequential stages [2]:

- 1) *Preprocessing*, which compensates for sensor drift and reduces sample-to-sample variations.
- 2) *Feature extraction*, employed to reduce the dimensionality of the measurement space and to extract relevant information for pattern recognition. In general, in an electronic nose containing an array of  $N$ -sensors, the measurement space has  $N$ -dimensions, causing statistical problems and a high degree of redundancy, being the sensors' sensitivities overlapping. For these reasons, it is convenient to achieve a low-dimensional projection of the  $N$ -dimensions, typically on two or three informative and independent axes. Extraction of the relevant information can be performed with the use of linear transformations,

like Principal Components Analysis (PCA) or Linear Discriminant Analysis (LDA). The first, which is the most used, finds projections of maximum variance, but it ignores the identity of the odor examples in the database, so it is not optimal for classification. The second finds projections that maximize the distance between examples from different odorants and minimizes the distance between examples of the same odorant. Some examples of nonlinear transforms also exist, like Sammon maps, which attempt to find a two- or three-dimensional mapping that preserves the distance between pairs of examples on the original  $N$ -dimensional space, or Kohonen self-organizing maps, which project the  $N$ -dimensional space onto a two-dimensional mesh of processing elements, named neurons, trained to respond to similar types of odorants.

- 3) *Classification*, which is trained to identify the representative patterns of each odor. When an unidentified odor is recorded, the classification stage assigns to it a class label by comparing its pattern with those compiled during training. The methods usually employed to perform this procedure are K Nearest Neighbours (KNN), which for a given number  $K$ , finds that number of examples in the odorant database that are closest to the unidentified odorant, and assigns the odorant class given by the majority among those; Bayesian classifiers, which as a first step generate a probability density function for each odor class on the low-dimensional space, so that when in presence of an unknown odorant, they pick the class which maximizes that probability distribution; Artificial Neural Networks (ANN) consisting of several layers of neurons connected with synaptic weights, which adapt to learn the patterns of different odorants during training, while after training when an unidentified odorant is present, a pattern is compiled through different layers of neurons and the system assigns the class label that provides the largest response.
- 4) *Decision-making*, it is used if any specific knowledge is available and it may modify the classifier assignment or determine that the unknown sample does not belong to any of the odorants in the database.

From the above description it is therefore evident how the architecture of an electronic nose clearly resembles that of a human nose, where the gas sensors array represents the olfactory receptors in the epithelium, signal transduction by the specific sensing mechanism mimics the operation of the olfactory bulb and the signal processing unit emulates the recognition process computed by the brain to characterize the perceived odorants (fig.1.2).

Differently from human panels and GC or MS analytical techniques, electronic noses offer the advantages of having a reduced weight, so they are adaptable as portable devices, they can be realized through conventional fabrication processes,

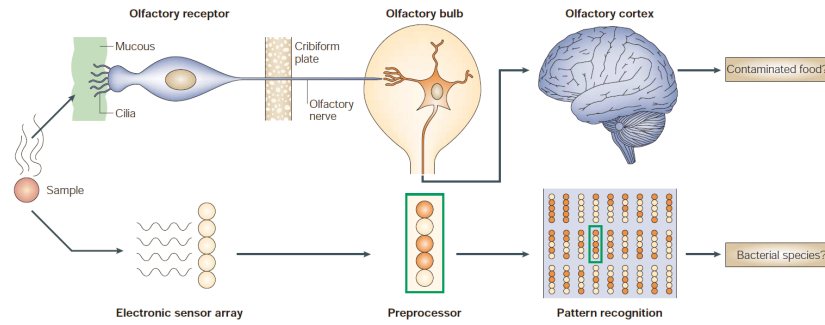


**Figure 1.2:** Similarities between an electronic nose and a human nose for the identification of ododrants [5].

leading to reduced costs and fast and easy reproducibility, they can be flexible and they allow real-time analysis.

Electronic noses find applications in many different fields. They can be used in medical care, to analyze breath, sweat and urine, so to provide a rapid diagnosis of infections [6]. In the pharmaceutical industry, the e-nose may be employed to screen incoming raw materials, to monitor production processes and maintain security in storage and distribution areas [7]. In food and beverage industry, e-noses can be used to assess the nature and quality of ingredients and to supervise the manufacturing process [8]. In safety and security applications, they may be used as an hazardous alarm for toxic and biological agents, screening of airline passengers for explosives, or examining vehicles for drugs and contraband at airports, border crossings and cargo terminals [9]. E-noses can monitor indoor air quality, and industrial and agricultural emissions and noxious environmental wastes [10] or work as smart fire alarms identifying hazardous combustion products [11]. In military applications, e-noses are studied as front-line tools to find buried land mines that threatens civilians, to detect biological and chemical agents, to monitor aging of warheads and artillery shells that could leak VOCs and induce explosions [12]. A summary with the main types of applications is provided by fig.1.3.

As it can be noticed, electronic noses have the potential to be employed in a wide variety of applications. Future trends, therefore, aim at developing devices for specific purposes, increasing their efficiency, minimizing the number of sensors needed to provide a high discrimination, integrating them with other analytical elements, like microfluidic systems, reducing instrument costs, and improve portability through miniaturization [2].

Industry sector	Application area	Specific use types and examples
Agriculture	crop protection harvest timing & storage meat, seafood, & fish products plant production pre- & post-harvest diseases	homeland security, safe food supply crop ripeness, preservation treatments freshness, contamination, spoilage cultivar selection, variety characteristics plant disease diagnoses, pest identification detect non-indigenous pests of food crops
Airline transportation	public safety & welfare passenger & personnel security	explosive & flammable materials detection
Cosmetics	personal application products fragrance additives	perfume & cologne development product enhancement, consumer appeal
Environmental	air & water quality monitoring indoor air quality control pollution abatement regulations	pollution detection, effluents, toxic spills malodor emissions, toxic/hazardous gases control of point-source pollution releases
Food & beverage	consumer fraud prevention quality control assessments ripeness, food contamination taste, smell characteristics	ingredient confirmation, content standards brand recognition, product consistency marketable condition, spoilage, shelf life off-flavors, product variety assessments
Manufacturing	processing controls product uniformity safety, security, work conditions	product characteristics & consistency aroma and flavor characteristics fire alarms, toxic gas leak detection
Medical & clinical	pathogen identification pathogen or disease detection physiological conditions	patient treatment selection, prognoses disease diagnoses, metabolic disorders nutritional status, organ failures
Military	personnel & population security civilian & military safety	biological & chemical weapons explosive materials detection
Pharmaceutical	contamination, product purity variations in product mixtures	quality control of drug purity formulation consistency & uniformity
Regulatory	consumer protection environmental protection	product safety, hazardous characteristics air, water, and soil contamination tests
Scientific research	botany, ecological studies engineering, material properties microbiology, pathology	chemotaxonomy, ecosystem functions machine design, chemical processes microbe and metabolite identifications

Figure 1.3: Examples of applications of electronic noses in different fields [13].

## **1.2 Thesis Content**

This thesis project was developed during a 8 months internship at Chilab - Materials and Processes for Micro & Nano Technologies laboratory in Chivasso (TO) in collaboration with the DISAT department of Politecnico di Torino.

The current section (Chapter 1) provides an overview of the overall project, with a brief introduction to the electronic nose and its working principles.

Chapter 2 focuses on a detailed description of gas sensors, their fundamental parameters, their implementations and different transduction mechanisms. In Chapter 3, Layered Double Hydroxides, chosen as active layer material in the realization of gas sensors for this project, are presented, with details on synthesis techniques, on their fundamental properties and morphologies, on their peculiar sensing mechanism and on their applications. Chapter 4 focuses on the design, optimization and fabrication of the gas sensors proposed for this thesis work, with details on the photolithographic process and on the deposition and subsequent characterization of the sensing layer. Chapter 5 provides a discussion on the results obtained from the gas sensing measurements. Chapter 6 finally contains a conclusive overview on the whole project and some considerations on possible future improvements.

# Chapter 2

## Gas Sensors Overview

A gas sensor is a device designed to transform a chemical information, namely the concentration of a particular gas, into an electric or optical signal [14]. Even though several types of sensors having different properties, structures, sensing and transduction mechanisms exist, they all share a common method for detection: gas molecules interact with the sensing material by absorption, adsorption or chemical reactions, inducing a chemical or physical change of the element, which is then transduced to a measurable signal [1].

Before starting the discussion about all the different categories of gas sensors, it is necessary to provide details about the parameters which determine their sensing performance.

### 2.1 Performance parameters

The general performance of the various gas sensors can be described on the basis of a predefined set of parameters, namely the so called "3 S's" (sensitivity, selectivity, stability), detection limit, response and recovery time . Here they are reported.

- 1) *Sensitivity*. It is an absolute number which provides the change in measurement signal per concentration unit of the analyte. It is a fundamental parameter to assess the quality of a sensor since it indicates how good is the device in measuring an output change associated to a change in the input. This value can be eventually extracted from the slope of a calibration plot, that is a plot of the gas concentration vs. sensor response [15]. There exist different ways to express sensitivity values, mainly depending on the type of gas sensors and on the transduction mechanism employed. As an example, in chemiresistive sensors, which exploit a variation in the resistance of the sensing material as the way of detection of a gas, sensitivity depends on a ratio between resistances, in conductometric sensors on conductances and in SAW sensors on currents,

as it will be further discussed in the following sections [16]. In the case of chemiresistive sensors, the sensor response is therefore indicated as (equation 2.5) (fig.2.1)

$$S = \frac{\Delta R}{R_b} \quad (2.1)$$

where  $\Delta R$  represents the resistance variation upon exposure to a gas, and  $R_b$  is the baseline resistance, that is the resistance value prior to exposition to the gas to detect, when only air is present [17]. From equation 2.1 it is evident that  $S$  is a number between 0 and 1.

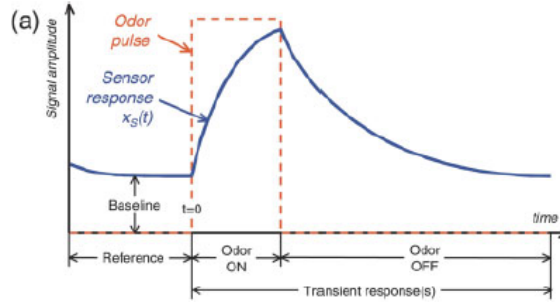


**Figure 2.1:** Sensor response to a gas pulse [17].

As it will be discussed in the following sections, two mechanisms can be responsible for the resistance variation in chemiresistive sensors, either redox reactions occurring at the active material surface, or the swelling of the material itself. Since  $\Delta R$  should always be a positive quantity, different cases should be considered. When dealing with redox reactions, according to the nature of the analyte, two options are possible [17]

$$\Delta R_{Red} = R_b - R_{gas} \quad (2.2)$$

$$\Delta R_{Ox} = R_{gas} - R_b \quad (2.3)$$

If instead just a swelling mechanism is involved

$$\Delta R = R_{gas} - R_b \quad (2.4)$$

Sensitivity can also be expressed through a percentage variation, according to equation 2.5

$$S(\%) = \left[ \frac{R_{gas} - R_{air}}{R_{air}} \right] \cdot 100 \quad (2.5)$$

The sensing response can be indicated in an alternative way, employing a physical parameter labeled  $S^*$ . As before, slight differences arise according to the characteristics of the sensing layer and of the analyte [18]

$$S_{Red}^* = \frac{I_{gas}}{I_{air}} = \frac{R_b}{R_{gas}} \quad (2.6)$$

$$S_{Ox}^* = \frac{I_{air}}{I_{gas}} = \frac{R_{gas}}{R_b} \quad (2.7)$$

when redox reactions are involved, where  $I_{gas}$  and  $I_{air}$  represent the current flowing through the sample when the sensor is exposed to the analyte and when only air is present respectively, or

$$S^* = \frac{I_{air}}{I_{gas}} = \frac{R_{gas}}{R_b} = S + 1 \quad (2.8)$$

in case of swelling. Differently from  $S$ ,  $S^*$  can be greater than 1.

- 2) *Selectivity*. It is the ability of a sensor to respond to a specific group of gases or even to a unique gas in the presence of other gases. Since sensors are usually sensitive to more than one analyte at the same time, selectivity is estimated by comparing the effects of different gases on the sensor [16].
- 3) *Stability*. It is the ability of the sensor to maintain its performance over a certain period of time. It is an important parameter to control to obtain a reliable response. As a measure of stability, drift values are used, that is the signal variation for zero concentration [16].
- 4) *Detection limit*. It is the lowest concentration value which can be detected by the sensor under definite conditions of precision and reproducibility. Together with sensitivity, it determines the quality of the performance of a sensor.
- 5) *Response and Recovery time*. The first is defined as the time needed by a sensor to reach a predefined value, generally set to 90%, of the full response in the presence of gases. Conversely, the second, is the time required to return to the baseline value after the gas is removed (fig.2.2). This last highly depends

on the sensing material, since it is strictly correlated with the desorption of the adsorbed gas molecules from its surface [16].

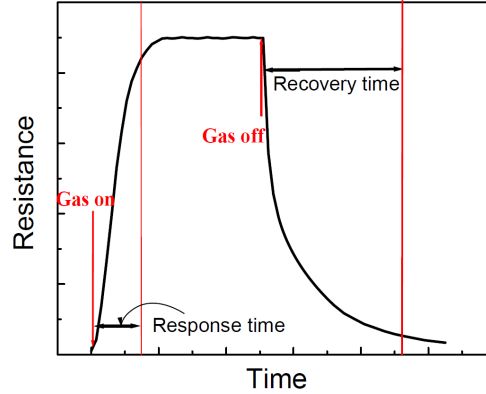


**Figure 2.2:** Schematic representation of a response curve for a chemiresistive gas sensor, showing response and recovery time [14].

These performance parameters can be influenced by several factors, like specific properties of the sensing material, temperature, humidity, gas flow rate and others. Temperature influences adsorption/desorption rates of gases on the surface of the sensing layers, in fact different adsorption/desorption parameters and reaction rates have different temperature profiles of the sensor’s response. Humidity mainly affects the sensitivity of sensors, which is highly reduced in the presence of water vapours, complicating the detection of target gases. As regarding flow rate, it also shows a significant effect on the sensing performance of the sensor. In particular, it has been found that in many cases, by increasing the total flow rate, the electrical measurable signal decreases, and vice versa [16].

Another important aspect which characterizes the performance of gas sensors, is the manipulation of the sensor’s response with respect to the baseline, needed to compensate for noise and other interference phenomena. Three methods are commonly used [17]:

- 1) *Differential.* The baseline signal  $x_s(0)$  is subtracted from the sensor’s response signal  $x_s(t)$  to remove any present noise  $\delta_A$ . The manipulated response is given by (equation 2.9)

$$y_s(t) = (x_s(t) + \delta_A) - (x_s(0) + \delta_A) = x_s(t) - x_s(0) \quad (2.9)$$

- 2) *Relative.* The sensor’s response is divided by the baseline, so eliminating the effect of multiplicative noise  $\delta_M$  and providing a dimensionless response

(equation 2.10)

$$y_s(t) = \frac{x_s(t)(1 + \delta_M)}{x_s(0)(1 + \delta_M)} = \frac{x_s(t)}{x_s(0)} \quad (2.10)$$

- 3) *Fractional*. The baseline signal is subtracted and divided from the sensor's response signal, providing a dimensionless, normalized response which compensates for sensors that have intrinsically large or small response levels (equation 3))

$$y_s(t) = \frac{x_s(t) - x_s(0)}{x_s(0)} \quad (2.11)$$

The choice of a suitable manipulation technique is highly dependent on the sensor's technology and particular sensor's application [17].

## 2.2 Classes of gas sensor devices

Gas sensors can be organized in different classes according to the principle which induces changes in the sensing element and allows detection to be performed. It is therefore possible to distinguish between: 1) conductivity sensors, exploiting an electrical conductivity variation as the measurable signal; 2) capacitive sensors, characterized by a capacitance variation; 3) piezoelectric sensors, behaving as mass-change sensing devices; 4) optical sensors, employing variations in optical properties; 5) potentiometric sensors, which measure a voltage variation; 6) calorimetric sensors, exploiting variations in thermal energy; 7) amperometric sensors, measuring a current variation; 8) analytical approaches. A summary of the mentioned categories is provided in fig.2.3.

As described in Section 1.1, e-noses are realized with specific gas sensors, according to the type of analytes to detect and on the required applications, therefore different implementation are possible. Fig.2.4 provides several examples of commercial e-noses realized with different gas sensors types.

Details about the mentioned types of sensors are provided in the following sections.

## Gas Sensors Overview

Principle	Measurand	Sensor type	Fabrication methods	Availability/sensitivity	Advantages	Disadvantages	
Conductometric	Conductance	Chemoresistor	MOS	Microfabricated, Sputtering	Commercial, many types, 5–500 ppm	Inexpensive, microfabricated	Operates at high temperature
			Conducting polymer	Microfabricated, Electroplating, Plasma CVD, Screen printing, Spin coating	Commercial, many types, 0.1–100 ppm	Operates at room temperature, microfabricated	Very sensitive to humidity
Capacitive	Capacitance	Chemocapacitor	Polymer	Microfabricated, Spin coating	Research	Applicable to CMOS-based chemosensor	Very sensitive to humidity
Potentiometric	Voltage/e.m.f.	Chemdiode	Schottky Diode	Microfabricated	Research	Integrated, Applicable to CMOS-based chemosensor	Needs Pd, Pt, Au, Ir (expensive)
	I-V/C-V	Chemotransistor	MOSFET	Microfabricated	Commercial, special order only, ppm	Integrated, Applicable to CMOS-based chemosensor	Odorant reaction product must penetrate gate
Calorimetric	Temperature	Thermal chemosensor	Thermister (pyroelectric)	Microfabricated, Ceramic fab.	Research	Low cost	Slow response
			Pellistor	Microfabricated	Research	Low cost	Slow response
Gravimetric	Piezoelectricity	Mass-sensitive chemosensor	QCM	Microfabricated, Screen printing, Dip-coating, Spin coating	Commercial, several types, 1.0 ng mass change	Well understood technology	MEMS fabrication, interface electronics?
			SAW	Microfabricated, Screen printing, Dip-coating, Spin coating	Commercial, several types, 1.0 ng mass change	Differential devices can be quite sensitive	Interface electronics?
Optical	Refractive index	Resonant-type chemosensor	SPR	Microfabricated, Screen printing, Dip-coating, Spin coating	Research	High electrical noise immunity	Expensive
	Intensity/spectrum	Fiber-optic chemosensor	Fluorescence, chemoluminescence	Dip-coating	Research	High electrical noise immunity	Restricted availability of light sources
Amperometry	current	Toxic Gas Sensor	Electrocatalyst	Composite Electrodes	Commercial ppb-ppm	Low cost noRh interference	Size

**Figure 2.3:** Summary of the main categories of gas sensors, together with their main properties (MOS - metal oxide semiconductor; QCM - quartz crystal microbalance; SAW - surface acoustic wave; MOSFET - metal oxide semiconductor field effect transistor; SPR - surface plasmon resonance) [17].

### 2.2.1 Conductivity sensors

These sensors are driven by the principle that interaction of a gas with the sensing material leads to a change in electrical conductivity (or resistance). Three main types of sensing materials are employed to realize these devices: Conducting Polymer (CP) composites, Intrinsically Conducting Polymers (ICP) and Metal Oxides (MOS). Although each of these materials is characterized by different mechanisms responsible for the change in resistance, the layout of the sensors is very similar: the sensing material (which is in direct contact with the gas to detect) is deposited over interdigitated or parallel electrodes creating electrical connections through which the resistance change is measured. For some sensing materials, a temperature higher than the ambient one is needed to properly operate, so a micro-heater is placed below the substrate to bring the sensor to the required

Manufacturer	Sensor type	No. of sensors	Applications	Pattern recognition/ comments	Website/reference/university background
Airsense analysis GmbH	MOS	10	Food evaluation; flavour and fragrance testing	ANN, DC, PCA Laptop	www.airsense.com/
Alpha MOS-Multi Organoleptic Systems	CP, MOS, QCM, SAW	6-24	Analysis of food types; quality control of food storage, fresh fish, and petrochemical products; packaging evaluation; analysis of dairy products, alcoholic beverages and perfumes	ANN, DFA, PCA Desktop	www.alpha-mos.com
Applied Sensor	IR, MOS, MOSFET, QCM	22	Identification of purity, process and quality control, environmental analysis, medical diagnosis	ANN, PCA Laptop	www.appliedsensor.com University of Linkopings, Sweden
AromaScan PLC	CP	32	Environmental monitoring, chemical quality control, pharmaceutical product evaluation	ANN Desktop	University of Manchester Institute of science and technology, UK
Array Tech	QCM	8	Diagnosing lung cancer, food analysis		University of Rome
Bloodhound sensors	CP	14	Food evaluation, flavour and fragrance testing microbiology, environmental monitoring, degradation detection	ANN, CA, PCA, DA Laptop	University of Leeds, UK
Cyrano Science Inc.	CP	32	Food quality, chemical analysis, freshness, spoilage, contamination detection, consistency in foods and beverages	PCA Palmtop	www.cyranosciences.com California institute of Technology, USA
Marconi Applied Technologies	QCM, CP, MOS, SAW	8-28		ANN, DA, PCA	University of Warwick, UK
Electronic Sensor Technology Inc.	GC, SAW	1	Food and beverage quality, bacteria identification, explosives and drug detection, environmental monitoring	SPR Desktop	www.estcal.com
Forschungszentrum Karlsruhe	MOS, SAW	40, 8	Environmental protection, industrial process control, air monitoring in textile mills, fire alarms. Quality control in food production. Automotive applications	PCA	www.fzk.de/FZK2/english
HKR-Sensorsysteme GmbH	QCM	6	Food and beverages, cosmetics and perfumes, organic materials, pharmaceutical industry	ANN, CA, DFA, PCA Desktop	www.hkr-sensor.de/ Technical University of Munich, Germany
Illumina	FO	-	Life sciences, food processing, agriculture, chemical detection	ANN	www.illumina.com Tufts University, USA

**Figure 2.4:** Summary of some examples of commercial e-noses realized with different types of gas sensors (CP - conducting polymer; IR - infra red; GC - gas chromatography; FO - fibre optic; ANN - artificial neural network; DC - distance classifiers; PCA - principal component analysis; DFA - discriminant function analysis; CA - cluster analysis; DA - discriminant analysis) [1].

operating temperature [1]. A schematic example of the typical structure of a conductivity sensor is shown in fig. 2.5.

### 2.2.1.1 Conducting Polymer Composite Sensors

Conducting polymer composites consist of conducting particles dispersed in an insulating polymeric matrix [1], so that the conductivity arises from particles while selectivity of the sensor is related to polymers [19].

The transduction mechanism of the sensor is explained on the basis of percolation theory. Upon exposure to a gas, part of it permeates into the polymer, so that the composite tends to reversibly swell to varying degrees depending on the polymer-gas interactions (fig.2.6) [20]. This expansion of the composite induces an increase in the electrical resistance of the film, which results from the disruption of conductive paths for charge carriers, naturally present in these composites [19].

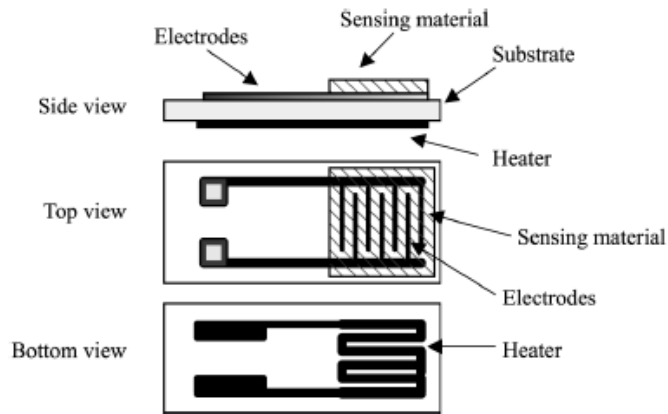


**Figure 2.5:** Example of the structure of a typical conductivity sensor [1].

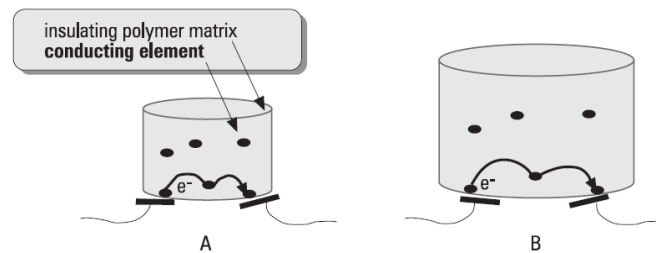


**Figure 2.6:** Schematic representation of the structure and swelling mechanism of CP composites [19].

A more complex mechanism characterizes polypyrrole-based composites, since the analyte can interact both with the insulating matrix and the conductive polymer, causing the expansion of both elements. This response can be easily monitored using a conventional ohmmeter [20].

Sensor's fabrication simply involves the realization of a thin film over electrical leads. As an example, carbon black composite sensors can be prepared by suspending the carbon black in a solution of the insulating polymer in a suitable solvent [1] and either dip coating an interdigitated electrode capacitor, dip coating or spin casting onto a glass substrate containing two separated metal leads [20]. For polypyrrole-based sensors, instead, a chemical polymerization of pyrrole using phosphomolybdic acid in a solution containing the insulating polymer is performed and the solution is then used to dip coat the substrate [20].

In some applications, instead of using a flat substrate, both bulk and surface micro-machining can be employed to produce wells on silicon substrates using patterned

silicon nitride/oxide as insulation and gold electrodes as the metal contacts. The polymer can be then simply dropped into the well using a syringe (fig.2.7) [21].

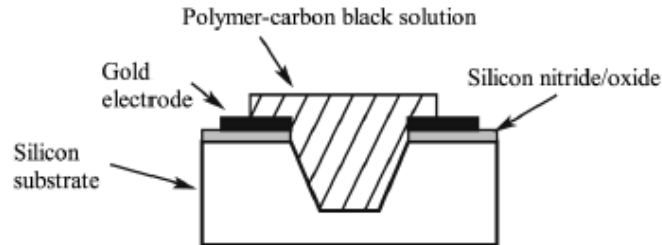


**Figure 2.7:** Example of a CP composite sensor obtained exploiting bulk micro-machining [21].

Sensitivity of these sensors is related to the vapor pressure of the analyte through an inverse proportionality relation: low vapor pressure compounds lead to very low levels (ppb), differently from high vapor pressure ones which are only detected at high ppm levels. The reason for this behaviour is identified in the higher tendency of low vapor pressure materials to reside in the polymeric matrix, lowering the detection threshold [19].

Generally CPs show operating resistances in a range of 1 – 1000  $k\Omega$ .

Response times vary from few seconds to minutes. They depend on the rate of diffusion of the gas into the polymer, property which is mainly influenced by the nature of the polymer and of the gas, the permeant concentration, the thickness of the film and temperature [1].

CP composites sensors show linear responses to concentration of different gases and good repeatability after several exposures.

Many advantages characterize this category of sensors [1]: 1) the costs for the realization of the devices are low and the process is relatively simple; 2) no heater is required since CP composites are able to operate at room temperature; 3) the signal conditioning circuitry required for these sensors is relatively simple since only a resistance change needs to be measured; 4) when employed in arrays, a high discrimination is achieved because of the wide range of polymeric materials available.

As regarding drawbacks, the main limitations relate to aging, which induces degradation of the sensor's performance, to a high sensitivity to humidity, which causes the necessity to eliminate background humidity to guarantee appreciable results, and to the poor sensing capability with particular gases (i.e. carbon-polymer composites are not sensitive to TMA) [1].

Examples of Conducting Polymer composite sensors are shown in fig.2.8.

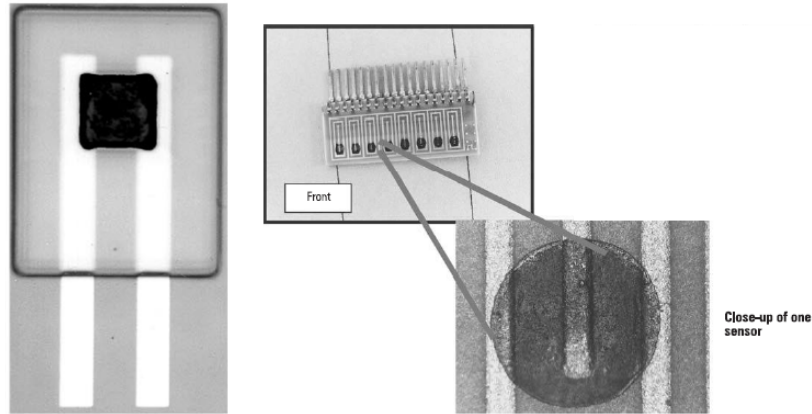


**Figure 2.8:** Conducting Polymer composite sensors characterized by carbon-black polymer as sensing material [21], [19].

### 2.2.1.2 Intrinsically Conducting Polymers

Intrinsically conducting polymers are characterized by linear backbones composed of repeating conjugated organic monomers, like acetylene, pyrrole, thiophene or aniline (fig.2.9) [20].

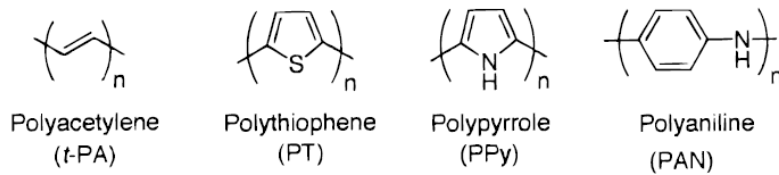


**Figure 2.9:** Chemical structures of different ICPs [20].

These materials are insulating in their neutral state, but through n-type or p-type doping, the polymers can become electrically conductive. This happens because doping generates charge carriers and alters the material's band structure, inducing an increased mobility of electrons or holes (depending on the type of doping used). In general, ICPs behave as one-dimensional conductors, since carriers mainly travel through the linear conjugated chains [20].

ICPs are employed in gas sensing applications, since their electrical properties show different responses to analytes in the vapor phase. When vapor sorption in ICPs occurs, the material undergoes swelling inducing a change in the conductivity of the polymer. This change has three contributions [20]:

$$\Delta\sigma = (\Delta\sigma_c^{-1} + \Delta\sigma_h^{-1} + \Delta\sigma_i^{-1})^{-1} \quad (2.12)$$

where

- $\Delta\sigma_c$  is the overall change in the intrachain conductivity (along the backbone) of the ICP;
- $\Delta\sigma_h$  is the change in intermolecular conductivity, due to electron hopping across polymeric chains induced by analyte sorption;
- $\Delta\sigma_i$  is the change in ionic conductivity between chains, related to proton tunneling induced by hydrogen bond interaction at the backbone and by ion migration through the polymer.

These conductivity changes are found to be also related to the physical structure of the polymer. In particular, the pathway for conduction through the polymer backbone is energetically more favourable than across different backbones [20]. ICP sensors are usually realized through electrochemical techniques, but also in-situ polymerization, conventional drop casting, inkjet printing or even 3D printing techniques may be employed. The overall structure of the sensor is similar to that shown in fig.2.5, with interdigitated electrodes, or a pair of metal leads deposited on an insulating substrate. The metal for the electrodes is usually gold (Au), while the substrate is glass. No heating element is needed (as for CP composite sensors) since the material can operate at room temperature.

The film of ICP material is deposited through electrochemical deposition, and its thickness is carefully controlled and eventually varied by monitoring the total charge passed through the deposition process [20]. The polymerization is performed in a three-electrode configuration, where the electrodes on the substrate are chosen as working electrodes. A positive potential is applied to the working electrode, initiating the polymerisation of the polymer on the substrate. The polymer is initially deposited on the two electrodes, and then it grows between them producing a complete film which bridges the electrodes as the polymerisation reactions progress [1].

The film thickness can be approximated by measuring the total charge applied during polymerisation, while the final potential applied to the material is responsible for doping [20].

As for CP composite sensors, response times depend on the sorption of vapor into the sensing material, that is on the diffusion rate of the permeant into the polymeric matrix. Generally they vary from seconds ( $\approx 30$  s) to minutes ( $\approx 240$  s) [1].

Several advantages characterize ICPs [20]: 1) reversible responses are obtained at relatively short times and at ambient temperature; 2) fabrication processes are simple and allow for miniaturization and mass production of sensors; 3) biomaterials may be incorporated in these structures; 4) ICPs are suitable for the realization of sensor's arrays since a wide range of polymers is available via electrochemical

polymerization of different monomer types; 5) the sensitivity of a sensor element can be altered by changing the polymerization conditions; 6) the oxidation state of the polymer can be altered after deposition to adapt the electronics of the polymer to a particular analyte so that an optimum charge transfer interaction takes place. As regarding drawbacks, it is necessary to mention the high sensitivity changes due to humidity which induce the need of performing operations in a controlled conditioned environment, aging which degrades sensor's response with time, and difficulties in resolving some types of analytes [1].

### 2.2.1.3 Metal Oxide Sensors

The principle behind the sensing mechanism of MOS sensors is based on a change in conductance of the oxide upon exposure and interaction to a gas. MOS sensors can be of two types: n-type (i.e. ZnO, SnO<sub>2</sub>, TiO<sub>2</sub>, Fe<sub>2</sub>O<sub>3</sub>), where electrical conduction occurs through electrons, or p-type (i.e. NiO, CuO, Co<sub>3</sub>O<sub>4</sub>), where electrical conduction occurs through holes [1].

In general, n-type semiconductors are widely used, while p-type ones, even if showing promising properties, are still principally a matter of research. Details on the behaviour of both types are provided.

- 1) **n-type MOS sensors.** When the sensing material is exposed to ambient air, at temperatures between 100 °C and 500 °C, oxygen, in atomic or molecular form, adsorbs on the surface of the n-type oxide semiconductor and ionizes into O<sub>2</sub><sup>-</sup>, O<sup>-</sup>, O<sup>2-</sup> by withdrawing electrons close to the surface of the semiconductor. In general the ionsorption species of O<sub>2</sub><sup>-</sup> are dominant at temperatures below 150 °C, O<sup>-</sup> between 150 and 400 °C, while O<sub>2</sub><sup>-</sup> above 400 °C [22]. An example of this ionsorption reaction is provided by equation 2.13 [1]



where s represents the surface. This leads to the formation of an electronic core-shell configuration, that is a n-type semiconducting region at the cores of particles and a resistive electron-depletion layer (EDL) at the shells of the particles (fig.2.10) [22]. At the same time potential barriers present between grains inhibit carriers' mobility [1].

The sensor's resistance for this material is mainly influenced by the resistive contacts between the shells of adjacent particles (fig.2.11a). Conduction occurs following a serial path, so it is possible to introduce an equivalent circuit to represent this situation, composed by a serial connection between semiconducting cores and resistive interparticle contacts (fig.2.11b) [22].

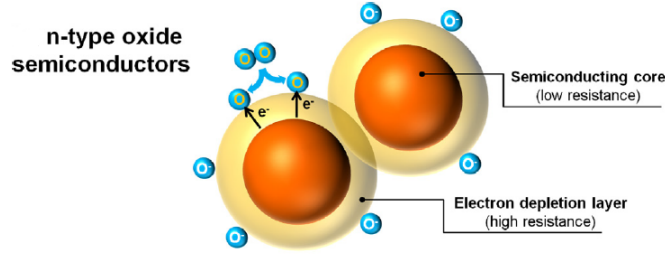


**Figure 2.10:** Formation mechanism of electronic core-shell structure in a n-type oxide semiconductor [22].

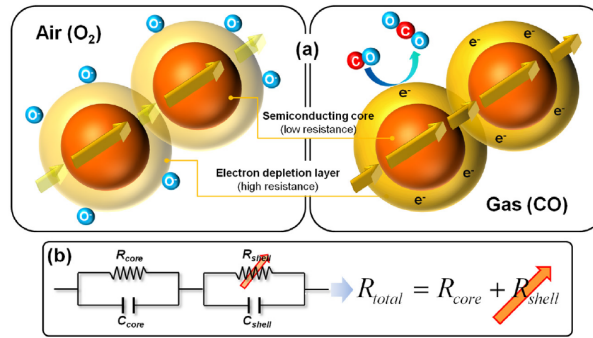
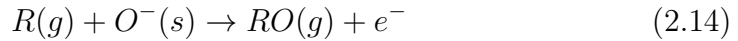


**Figure 2.11:** (a) Gas sensing mechanism and (b) equivalent circuit of a n-type MOS sensor [22].

When a n-type MOS sensor is exposed to a reducing gas (i.e.  $H_2$ ,  $CH_4$ ,  $CO$ ), the gas reacts with the oxygen adsorbed, which releases the electron previously taken from the surface of the MOS, bonding instead to the electron of the reducing gas. This induces a drop in the resistance. This reaction lowers the potential barrier, allowing electrons to flow thus increasing conductivity. Equation 2.14 describes the reaction just described [1]:



where  $R(g)$  is the reducing gas.

When the gas is an oxidising one (i.e.  $O_2$ ,  $NO_2$ ,  $Cl_2$ ), a reaction analogous to the oxygen adsorption occurs, so that the molecule (or atom) gas withdraws an electron from the MOS. In this case, if adsorption of the oxidising gas is stronger than the oxygen one, a further reduction in the conductivity of the material (and consequent increase in resistance) will occur because of a new induced decrease in its electrons. The involved reaction is represented by

equation 2.15 [1]:



where  $A(g)$  is the oxidising gas.

- 2) **p-type MOS sensors.** Differently from the n-type sensors, in this case, the adsorption of oxygen anions at the surface of the semiconductor induces the formation of a electronic core-shell configuration characterized by a hole-accumulation layer (HAL) near the surface of the material and an insulating region at the core of the particles (fig.2.12). In general, the amount of oxygen adsorbed on the surface of a p-type MOS is larger than that for its n-type counterpart [22].

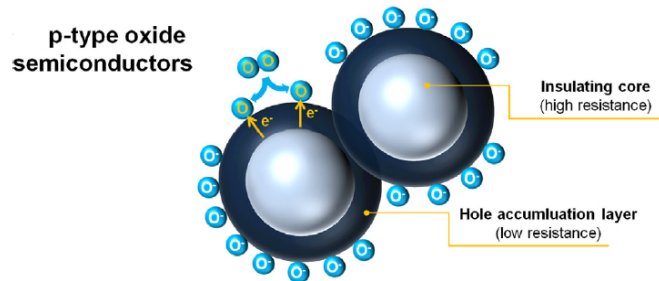


**Figure 2.12:** Formation mechanism of the electronic core-shell structure in a p-type oxide semiconductor [22].

For p-type MOS sensors, conduction occurs following parallel paths across the resistive core and along the shell regions (fig.2.13a). Also in this case it's possible to introduce an equivalent circuit to represent this situation, composed by a parallel connection between resistive cores and shell layers (fig.2.13b) [22].

When the material is exposed to a reducing gas, the electrons injected back into the material as a consequence of the reaction between the gas and the surface oxygen anions, recombine with holes decreasing the concentration of majority carriers on the shell layer with a consequent decrease in conductivity (and increase in resistance). An exception occurs when the oxide semiconductor particles are larger than twice the thickness of the HAL. In this case, the change in concentration of holes because of electron-hole recombination doesn't induce significant variations to the resistance at the interparticle contacts, in agreement with the conduction mechanism of the material, mainly occurring

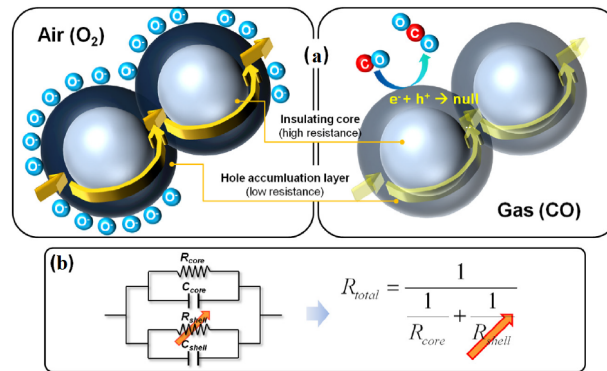


**Figure 2.13:** (a) Gas sensing mechanism and (b) equivalent circuit of a p-type MOS sensor [22].

along semiconducting shells [22].

The opposite situation verifies when exposing the sensing material to an oxidising gas: hole concentration increases in the shell layer because of the ionsorption of oxidising gas with a consequent decrease in resistance [22].

Several techniques can be employed to realize MOS gas sensors. Thin or thick films can be deposited using screenprinting, spin coating, RF sputtering or chemical vapor deposition (CVD). The sensor’s configuration can be of two types, either characterized by the usual flat substrate (fig.2.5) or by a tube type one (fig.2.14), made of alumina, glass, silicon or other ceramics, with gold, platinum, silver or aluminium electrodes. In both cases the heating element is fundamental to provide the high temperatures necessary to activate the sensing properties of metal oxides [1] (further details about the heating element will be provided in section 2.2.1.4). This necessity may represent a limitation in the fabrication of MOS sensors, so attempts to realize materials able to work at room temperature have been made. A valid solution for SnO<sub>2</sub> sensors consists in treating the sensors’ elements with an oxygen plasma. When the semiconductor surface is exposed to on oxygen plasma, which contains several oxygen species including both positively and negatively multiple charge species, it gets covered by a high concentration of oxygen that reacts with the gases and allows sensitivity at room temperature. After this treatment, it was found that the material was sensitive to CO, CCl<sub>4</sub> and CH<sub>4</sub>O at room temperature, which couldn’t be detected in the untreated case [20].

The sensitivity of metal oxide gas sensors depends on the thickness of the sensing film and on the temperature at which the sensor is operated. Thin film devices show a faster response and higher sensitivities, but are more difficult to manufacture, so

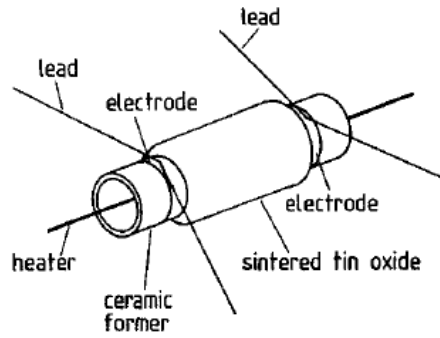


**Figure 2.14:** Schematic representation of a SnO<sub>2</sub> sensor in a tube type configuration. The sensing material is deposited around a ceramic tube. A heater runs through the center of the tube and electrical contacts are provided at both ends [20].

generally MOS sensors are based on thick film technologies [1].

Another factor which influences sensitivity is the morphology of the nanostructures. The sizes of nanoparticles in n-type MOS sensors, determine the degree of electron depletion, while assembles configuration and agglomeration strictly relate to the resistivity of the interparticle contacts and the gas accessibility. Also in the case of p-type MOS sensors these factors affect the sensing behaviour of the material, but the influence is lower than for the n-type counterpart [22].

The sensitivity for a n-type MOS sensor increases when the diameter ( $D$ ) of the MOS particles decreases to a value below twice the thickness of the EDL ( $t_{EDL}$ ) since the depletion region extends over the whole grain. The same behaviour is expected for a p-type MOS sensor, even if the precise dependence on the particle size still needs to be established [22].

As regarding the dependence on interparticle contact area, assuming that the grain size is kept constant, the sensitivity is found to decrease with decreasing values of contact area. As an example, a sensor realized through Co<sub>3</sub>O<sub>4</sub> nanofibers compared to another characterized by nanoparticles obtained through the same material after it was ultrasonically treated, showed a much higher response, even if the crystallite size was identical [22].

Both the concentration of charge carriers and the configuration of the electrical core shell appear to be fundamental to control the gas sensing response of MOS sensors. Gas response can be enhanced through a careful control of the concentration of charge carriers according to a process referred to as "electronic sensitization". In particular, the use of acceptor doping can be employed to reduce the concentration of electrons in the semiconductor in a n-type MOS sensor, letting the material become more sensitive to reducing gases. For the p-type counterpart, the use of electronic sensitization to tune the concentration of holes in the semiconductor has

not yet been widely explored [22].

Another fundamental factor which influences sensitivity is temperature. This dependence becomes clear when considering that the operation of the sensor relies on chemisorption and redox reactions at the surface of the material, both processes having rates which are function of temperature [23].

MOS sensors are characterized by several advantages: 1) higher sensitivity when compared to polymeric sensors, since they are able to detect concentrations in the ppb range; 2) very fast response and recovery times, both depending on the operating temperature and on the level of interaction between the sensor and the gas; 3) devices are small, they can be easily integrated directly into the measuring circuit and have relatively inexpensive fabrication costs [1].

They are also characterized by some limitations. In particular, they need high operating temperatures to activate their sensing properties, which is translated in an increased power consumption with respect to sensors working at room temperature. Moreover they suffer from sulfur poisoning due to irreversible binding of compounds that contain sulfur to the sensor oxide, and exhibit a limited range of coatings [22]. Differently from CP composite and ICP sensors, they are not flexible nor transparent.

Long-term stability is another problematic issue for MOS sensors. In fact, both a degradation in sensitivity over long periods of operation and a change in the resistance of the sensors verify. These problems are mainly caused by humidity or by irreversible reactions of the sensing material with the analytes. Drift induced by humidity can however be solved by performing a thermal treatment on the sensing material at temperatures above 150 °C [14].

Another limitation which characterizes MOS sensors is poor specificity to different analytes. Some solutions can however be implemented to improve this property [14]:

- *Variation of the operating temperature.* As previously mentioned, sensitivity depends on temperature. This temperature dependence of the sensitivity of different gases can be exploited to obtain the selectivity for a particular analyte.
- *Use of additives.* Again, as the sensing mechanism occurs as a consequence of an interaction between the gas and the MOS surface, by including a suitable additive to the material, selectivity is improved, since the additive works as a catalyst to enhance only specific reactions. Examples of additives commonly used are Pd, Pt, Au or Ag.
- *Incorporation of filters.* The selectivity for molecules of a specific size can be enhanced by depositing a diffusion filter layer on top of the MOS. In this way only filtered molecules can reach the surface of the sensing material and

interact with it.

#### 2.2.1.4 Micro-heater

As mentioned in the previous sections, in some cases it is necessary to activate the sensing properties of specific materials through heat release. For this reason, sensors may be equipped with a micro-heater on the back of their substrate, able to drive the sensor to the required operating temperature. In this framework, micro-hotplates become fundamental for the realization of gas sensors. The main features which are responsible for their successful application, relate to the low amount of energy required to heat the sensing layer, which results in an extremely reduced power consumption, together with the compatibility with CMOS technologies [24]. They consist of a heater, generally a Pt one, stacked between a dielectric membrane and an insulator, on which electrodes are deposited. In some cases, they may be complemented by a thermometer, used to carefully measure the temperature variations. Integration of heater and thermometer can occur in two different ways [25]: vertical approach, in which heater and thermometer are formed in different layers (fig.2.15a). The alternative is the horizontal approach, which is employed when Pt and Au are used as electrode materials. In this case, heater and thermometer can be integrated in the same layer as that including the electrodes (fig.2.15b). The main advantage of this configuration is that no additional process steps are necessary for the integration of the two mentioned elements.

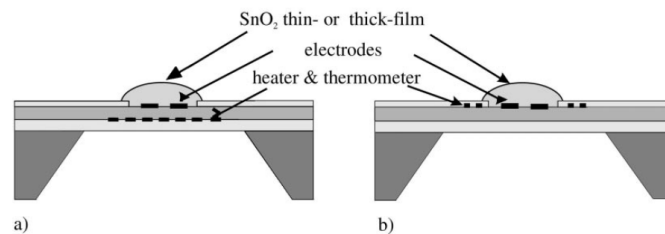


**Figure 2.15:** Schematic representation of a micro-hotplate in a (a) vertical and (b) horizontal approach [25].

Heater and thermometer can either be realized through Pt, polysilicon or p++ doped (Boron-doped) structures. Pt can be easily sputtered and patterned by lift-off process or ion beam etching, while polysilicon can be deposited through standard CVD and patterned through photolithography. As regarding p++ silicon, it may constitute an alternative to the first two solutions, but it is affected by different drawbacks, since as a consequence of the incorporation of Boron atoms in the Si crystal structure, high mechanical stresses are induced [25].

Micro-hotplates can be realized through a combination of bulk and surface micromachining. An example of the steps involved in the fabrication process is provided [26]:

- 1) The device is obtained starting from a double side polished Si wafer, coated on both sides with a low stress SiN layer (fig.2.16a).
- 2) The membrane on which the micro-hotplate will be developed is released through the application of bulk micromachining on the backside of the wafer. This procedure involves the patterning of the SiN layer through reactive ion etching, followed by the anisotropic etching of Si through potassium hydroxide (KOH) solution (fig.2.16b and c).
- 3) As the suspended SiN membrane is obtained, heaters, are deposited on top of it through magnetron sputtering and patterned through photolithography. An annealing step is performed to stabilize the electrical properties (fig.2.16d).
- 4) The heater is covered by a thick SiO<sub>2</sub> layer to ensure electrical insulation with respect to the electrodes. This layer is grown by plasma-enhanced CVD and patterned by wet etching to realize windows for the deposition of electrical contacts (fig.2.16e).
- 5) The contact pads and electrodes are finally fabricated by lift-off (fig.2.16f). The obtained structure can now be integrated onto the contact electrodes of the gas sensor and the sensing element can then be deposited on top of it (fig.2.16g).

The design of a micro-hotplate should aim at optimizing heat transfer and minimize losses. Heat transfer can occur either as heat conduction, convection or radiation. Above and below the membrane, heat transfer occurs both by conduction and by convection with the surrounding atmosphere. This last contribution represents one of the reasons of heat losses. These can be minimized through a reduction of the heated area or by coating the backside of the membrane with glossy materials, like gold, characterized by a lower emissivity than SiO<sub>2</sub>. The use of a gold coating also increases the heat conduction through the membrane, being a good thermal conductor [25].

A further solution to reduce power consumption, is to power the micro-hotplate through predefined pulses, so heating it for a very short time and living it cold for a longer one. This operation should be performed in a careful way since having negative effects on response and recovery times, which tend to increase [27]. Beside the advantage related to the low power consumption, remarks should be provided regarding the ability to withstand very high temperatures (also close to 1000 °C), and the possibility to perform a "on-chip" annealing of the coating material [28].

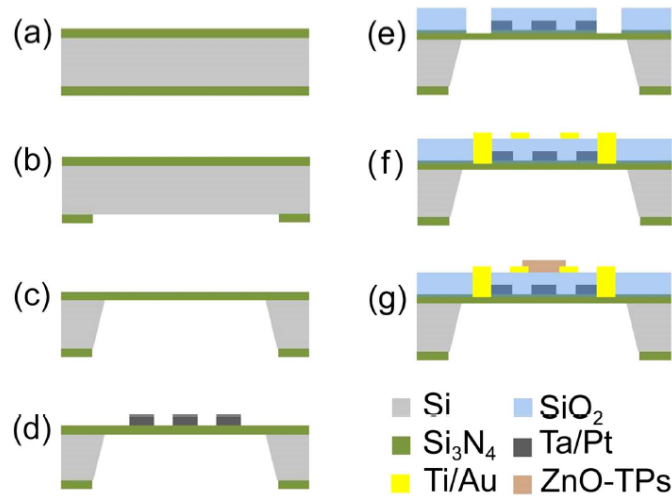


**Figure 2.16:** Schematic representation of the steps involved in the fabrication of a micro-hotplate: (a) starting Si substrate coated by SiN on both sides, (b) SiN patterning, (c) Si anisotropic etching, (d) heater deposition and patterning, (e) SiO<sub>2</sub> insulating layer deposition and patterning, (f) deposition of bonding pads and electrical contacts, (g) sensing material integration [26].

### 2.2.2 Capacitive sensors

This category of sensors provides a response to the detection of gas in the form of a variation of capacitance. Knowing that the capacitance can be expressed as

$$C = \varepsilon_0 \varepsilon_r \frac{A}{d} \quad (2.16)$$

where  $\varepsilon_0$  represents the permittivity in vacuum and  $\varepsilon_r$  represents the relative permittivity,  $A$  is the electrode area and  $d$  is the distance between electrodes (corresponding to the thickness of the dielectric layer), in order to be detected, molecules of the gas must induce a change either in the dielectric constant or in the layer thickness, since variations in the electrode area are very uncommon. In general, changes in the dielectric layer thickness are preferred [29].

Capacitive sensors can be realized by employing polymeric films or porous ceramics as sensing materials (in general the first category of materials is preferred) [29].

The sensing operation of capacitive sensors occurs in two states: in the first state only air is incorporated in the polymer, since no analyte molecules have diffused in the material (fig.2.17a). In this condition a capacitance value is measured to constitute the baseline. In the second state, the polymeric layer absorbs the gaseous analyte, inducing a change in its electrical and physical properties, which translates into a variation in capacitance (fig.2.17b) [17].

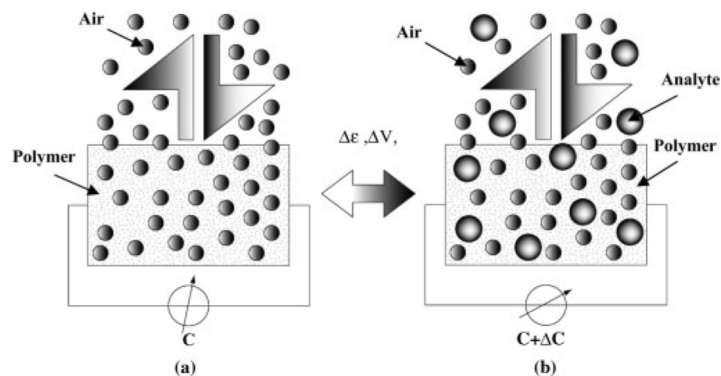


**Figure 2.17:** Sensing mechanism of a capacitive sensor. Two states are represented: (a) no analyte molecules are present in the sensing material, (b) analyte molecules diffuse in the sensing material [17].

The usual fabrication process consists in the deposition of two interdigitated electrodes on top of a substrate, which are spin coated or spray coated with polymers [17]. An heating element can also be placed on the back of the structure if the sensing material needs elevated temperatures to detect gases.

Several advantages characterize this type of sensor: 1) the capacitor structure is very simple so it enables miniaturization, high reliability and low cost; 2) amplification of capacitance is performed through oscillator circuits, simply consisting of a resistor and a capacitor, leading to a good sensitivity; 3) selective detection is easily performed. The main disadvantage of the structure, consists in an excessive sensitivity to humidity, which induces the need to operate in a controlled environment and leads to stability problems in the long-range [17].

### 2.2.3 Piezoelectric sensors

Piezoelectric sensors belong to a family of devices referred to as "mass-sensitive" sensors, for which a change in the mass of the sensing element is translated in a measurable electric signal. The fundamental mechanism which drives the response is the piezoelectric effect, typical of a particular class of materials. These materials produce a voltage when a mechanical stress is applied, and conversely they deform if a voltage is applied across them. This arrangement can be exploited as a gas sensor by applying a sensitive coating to piezoelectric materials allowing a selective absorption of certain substances. The resulting mass change is electrically measured as a frequency shift [20].

There are two types of piezoelectric sensors exploited in gas sensing: bulk acoustic wave (BAW) devices, often referred to as quartz crystal microbalance (QCM) as

representing the most used device, and surface acoustic wave (SAW) sensors. In both cases, sorption of gas molecules in the sensing coating induces changes in the propagation of the acoustic waves leading to variations in the resonant frequency. For BAW sensors, the acoustic wave propagates through the bulk of the crystal, in a direction perpendicular to the surface, while for SAW sensors, motion occurs only at the surface [20].

A description of both configurations is provided.

### 2.2.3.1 Quartz Crystal Microbalance sensors

In QCM sensors, a quartz crystal is made to oscillate at a characteristic resonant frequency when it is excited by the application of a suitable AC voltage. The device is composed by a monocrystalline quartz slice, having a diameter  $\sim 1$  cm, cut along certain crystallographic planes. Electrodes, generally made of Au, are evaporated onto both surfaces of the crystal [17]. A sensing coating able to absorb gas upon exposure, increasing its own mass, is finally deposited on the surface of the crystal. This increase in mass alters the resonant frequency of the quartz crystal, whose variation is registered to provide a measure of the analyte [1]. Fig.2.18 shows the structure of the device.

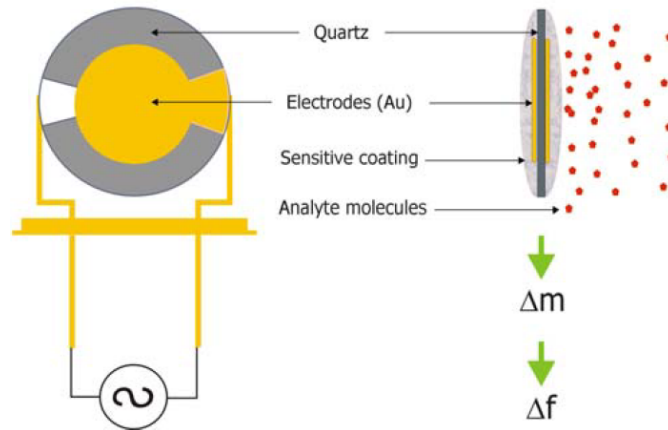


**Figure 2.18:** Schematic representation of a QCM sensor [30].

The relation between the frequency variation and the mass of the film deposited on the crystal surface can be described through the Sauerbrey equation:

$$\Delta f = f_0^2 \frac{-\Delta m}{A \sqrt{\rho_q \cdot \mu_q}} \quad (2.17)$$

where  $\Delta f$  is the frequency variation,  $\Delta m$  is the mass variation after gas molecules'

absorption,  $f_0$  is the resonant frequency of the crystal,  $A$  is the electrode area, also called active area,  $\rho_q$  and  $\mu_q$  are the density and shear modulus of quartz respectively [17].

The Sauerbrey equation can be rewritten in a simplified form under the assumption that the frequency variation is given in  $Hz$ , the resonant frequency in  $MHz$ , the mass variation in grams and the area in  $cm^2$  [17]:

$$\Delta f = -2.3 \cdot 10^6 f_0^2 \frac{\Delta m}{A} \quad (2.18)$$

According to equation 2.18, a higher sensitivity, defined as the ratio between the frequency and the mass variations, is achieved with a combination of high resonant frequency and small active area. QCM devices generally operate in a frequency range 5-30 MHz. Sensitivity to several types of analytes is easily achieved in QCM, and selectivity can be tuned by choosing the appropriate coating membrane.

For the fabrication of the device, micromachining is generally used, and coatings, whose thickness generally ranges between 10 nm and 1  $\mu m$  can be deposited through spin coating, airbrushing, inkjet printing or dip coating [1].

The advantages of using QCM relate to fast response times ( $\sim 10$  s), good sensitivities and selectivities because of the wide range of available coatings, and good batch to batch reproducibility.

However they are also characterized by several disadvantages, including complex fabrication processes and interface circuitry, poor signal to noise ratio performance because of surface interferences and the size of the crystal [1].

### 2.2.3.2 Surface Acoustic Wave sensors

SAW devices are composed of a piezoelectric substrate with two interdigitated electrodes, an input one acting as a transmitter and an output one acting as a receiver, deposited on top of it. A sensitive membrane is deposited between them [1]. Two types of configurations can be realized [31]:

- **Delay line configuration.** In this case the sensitive membrane creates a delay in time between input and output signals based on its extension (fig.2.19a).
- **Resonator configuration.** To the usual design, two grafting electrodes outside each interdigitated electrode are placed, forming a resonant cavity in between. In this case the sensing coating is deposited as to contact both electrodes (fig.2.19b).

In both cases, the sensor is stimulated by applying an AC voltage to the input electrode which creates an acoustic wave that propagates along the crystal surface

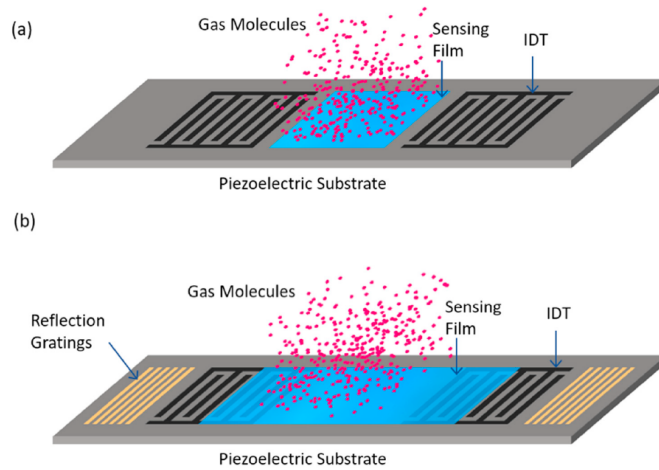


**Figure 2.19:** Schematic of a SAW sensor in (a) delay line and (b) resonator configurations [31].

and induces a deformation of the piezoelectric substrate. The mass of the gas sensitive coating changes upon interaction with a gas and causes a frequency alteration. The change in frequency is described as:

$$\Delta f = \frac{\Delta f_p c_v K_p}{\rho_p} \quad (2.19)$$

where  $\Delta f_p$  is the change in frequency caused by the sensing membrane,  $c_v$  is the vapor concentration,  $K_p$  is the partition coefficient and  $\rho_p$  is the density of the membrane used [1].

The substrates are usually realized from ZnO, LiNbO<sub>3</sub>, or quartz, due to their natural piezoelectric properties, while the sensitive membrane can be polymeric or liquid crystal, even if recent studies also refer of the use of phospholipids and fatty acids [1].

Fabrication processes rely on photolithography, with deposition of coatings occurring through airbrush, screen printing, dip coating and spin coating techniques. The thickness of the membrane generally ranges from 20 to 30 nm [1].

The advantages of using SAW sensors are numerous: 1) they show very high sensitivities and low detection limits, which depend on the choice of the membrane as for QCM sensors; 2) a broad variety of gases can be detected due to the wide range of available coatings; 3) selectivity can be easily tuned through the choice of an appropriate membrane; 4) fast response times are generally achieved; 5) fabrication processes are compatible with planar IC technologies [1].

As regarding the limitations of SAW devices, the main problems relate to poor signal to noise ratio since they operate at high frequencies, complexity in the

circuitry required to drive them and difficult reproducibility. They also show a poor long-term stability and a high sensitivity to humidity. The main differences in performance compared to QCM sensors consist in a better sensitivity since they tend to work at higher frequencies, in a range of 100 to 400 MHz, and are characterized by a reduced base mass [1].

## 2.2.4 Optical sensors

Optical sensors perform detection of analytes by measuring a change in optical properties. Several transduction mechanisms can be employed to detect the analyte, fluorescence intensity and lifetime, polarization, spectral shape, absorbance, wavelength and reflectance [20]. Some examples of widely used devices are reported.

### 2.2.4.1 Surface Plasmon Resonance (SPR) sensors

This category of sensors exploit SPR, that is an optical phenomenon in which incident light excites a charge-density wave at the interface between a high conductive metal and a dielectric material if specific conditions determined by the permittivities of the two materials are satisfied. These sensors are sensitive to a change in the refractive index of a surface [17].

In general, the SPR can be measured using the Kretschmann configuration, which consists of a prism having a thin gold metal layer deposited on its base, coated with a sensing membrane, usually deposited through spin coating. Excitation is induced through illumination from a light source and the SPR reflection spectrum, that is the intensity of reflected light versus angle of incidence with respect to the normal of the interface between metal and dielectric, is measured. Reflected light is measured through a CCD camera attached to a computer.

The main advantage of this sensor is represented by a high resistance to electrical noise, but the realization costs are extremely elevated [17].

### 2.2.4.2 Fluorescent sensors

In this configuration, the sensor is constituted by an optical fiber with a 2  $\mu\text{m}$  diameter, whose sides or tips are coated with a fluorescent dye encapsulated in a polymeric matrix (fig.2.20).

As the sensor is exposed to a gas, interaction occurs, leading to polarity alterations in the fluorescent dye translated in variations of the material's optical properties. These changes are measured and analysed and are used as response mechanism for gas detection [1].

Sensitivity depends both on the type of fluorescent dye and on the polymer used to support it. The choice of a suitable polymer should be performed based on

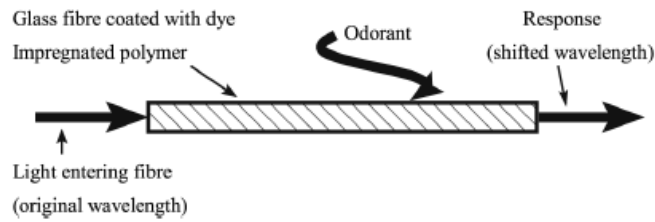


**Figure 2.20:** Representation of a fluorescent sensor realized through an optical fiber [1].

different fundamental properties, namely polarity, hydrophobicity, porosity and swelling tendency. The polymer can be eventually modified by the addition of adsorbants to improve the response and lower the detection limit of the sensor. The main advantages of fluorescent gas sensors relate to very fast response times, less than 10 s, the compact and lightweight characteristics of the fibers, which allow them to be easily employed in arrays, and, as for SPR sensors, a good immunity to electrical noise. As regarding limitations, the main problems are due to the necessity of very complex electronics and software, leading to high costs, a restricted availability of light sources to drive the sensor, and short lifetime due to photobleaching [1].

A variation to the fluorescent sensor can be performed by employing a colorimeter coupled to an optical fiber. In this case, changes in absorption and emission of radiation and polymer swelling, induced by variations in refractive index of fiber coatings, are monitored optically [17].

## 2.2.5 Potentiometric sensors

This category of sensors works by converting physical and chemical changes in an electrical signal, in particular by measuring the variation in the voltage applied across electrodes. The most employed configuration exploits a metal-oxide-semiconductor field-effect transistor (MOSFET) [1].

### 2.2.5.1 MOSFET sensors

MOSFET sensors exploit the same technology of the transistors usually employed in analog and digital electronics applications. The basic structure consists of a metal gate, usually made of Al, on top of an oxide layer, generally represented by  $\text{SiO}_2$ , and a p-type Si base with n-doped channels at its two sides, which constitute source and drain regions.

To understand the sensing feature of a MOSFET sensor it is necessary to introduce a set of equations which describes the behaviour of the device [32]:

- *Threshold voltage.* It is defined as the voltage applied between gate and source contacts to turn on the device (equation 2.20)

$$V_{th} = V_{FB} - \frac{Q_d}{C_{ox}} + 2\phi_p \quad (2.20)$$

where  $V_{FB}$  is the flat-band voltage,  $Q_d$  is the total bulk depletion charge per unit area,  $C_{ox}$  is the oxide capacitance per unit area and  $\phi_p$  is the bulk potential, that is the potential difference between the doped bulk silicon and the intrinsic silicon [32].

- *Flat band voltage.* It is fundamental to provide a definition for this quantity since entering the expression of the threshold voltage and determining its dependence on the metal and semiconductor work functions (equation 2.21)

$$V_{FB} = \phi_M - \phi_S \quad (2.21)$$

where  $\phi_M$  and  $\phi_S$  are the metal and silicon work functions respectively.

- *Work function.* It is the minimum thermodynamic work needed to remove an electron from a solid to a point in vacuum immediately outside the solid surface

$$\phi = -e\varphi - E_F \quad (2.22)$$

where  $e$  represents the electron charge,  $\phi$  is the electrostatic potential in vacuum, and  $E_F$  is the Fermi level inside the material.

- *Drain current.* It represents the current flowing in the channel of the device from source to drain terminals, and, according to the region of operation of the device, it is expressed as (equations 2.23 and 2.24)

$$I_{DS} = \mu C_{ox} \frac{W}{L} \left[ (V_G - V_{th})V_D - \frac{1}{2}V_D^2 \right] \quad (2.23)$$

in the unsaturated region ( $V_D < V_G - V_T$ )

$$I_{DS} = \frac{1}{2} \mu C_{ox} \frac{W}{L} (V_G - V_{th})^2 \quad (2.24)$$

in the saturated region, where  $\mu$  is the electron mobility in the channel,  $W$  is the width of the channel and  $L$  is its length,  $V_G$  and  $V_D$  are the voltages applied to gate and drain.

From equations 2.20 and 2.21, it is evident that the threshold voltage strictly depends on the metal work function, so on the type of metal used to realize the gate. This dependence can be therefore exploited to let the device work as a sensor. In particular, a shift in the threshold voltage occurs upon interaction of the gate material with a given gas [1].

To exploit this property, some variations to the structure of the device need to be performed. These often involve alternative configurations of the gate or its direct omission. Different solutions are possible:

- **Gas sensitive FET (GASFET)**. It is the most used configuration. The structure is the same as that of the MOSFET except for the gate, which is now constituted by a catalytically active metal (fig.2.21).

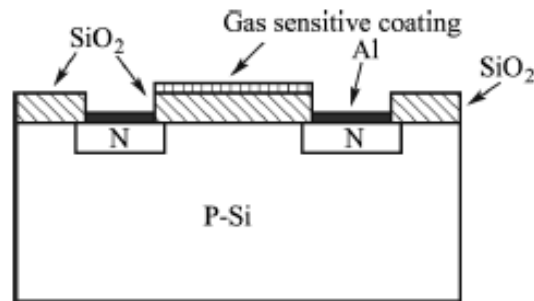


**Figure 2.21:** Schematic representation of a GASFET [1].

It is based on the principle that adsorption of gas molecules on the sensing surface, induces a variation in the metal and semiconductor work functions. This variation is related to the polarization of the surface and interface of the metal/oxide layer, and is influenced by the metal gate configuration, either continuous, as in the case of thick films, or discontinuous, as for thin films. Detection occurs mainly for hydrogen-containing gases, and according to the two mentioned configurations some differences arise: 1) on a continuous surface, the metal catalyzes dehydrogenation reactions of gases employing oxygen as an electron acceptor. Hydrogen is therefore adsorbed on the metal surface and can diffuse towards the metal/oxide interface, where a dipole layer is created, which induces a variation in the metal/semiconductor work function. 2) On a discontinuous surface, changes are due both to the hydrogen dipole layer and to adsorbates on the metal surface and on the exposed portions of the oxide layer [20].

The changes in work function and consequently in threshold voltage, are proportional to the analyte concentration, so they can be exploited as the response mechanism for the gas.

GASFETs are produced by standard microfabrication techniques, incorporating the deposition of the gas sensitive catalytic layer. The three main employed materials used for the realization of the catalytic layer are Pd, which has a good sensitivity to hydrogen, Pt and Ir, highly sensitive to ammonia and ethanol. By modifying the operating temperature of the device, it is possible to enhance the catalytic activity of the sensor for particular analytes. Also polymers can be employed as sensitive coatings, with the advantage of being able to operate at room temperature [33].

- **Open Gate FET (OGFET).** It is constituted by a MOSFET in which the metal gate is simply omitted, letting the oxide be directly exposed to the analyte (fig.2.22). The gas adsorption on the surface of the oxide layer results in dissociation of gas molecules, which get transported along the surface under the influence of the electric field arising from the application of a drain-source voltage. The response of the sensor is given by a variation of the drain-source current, which, as shown in equations 2.24 and 2.23, also depends on the metal and semiconductor work functions [32].

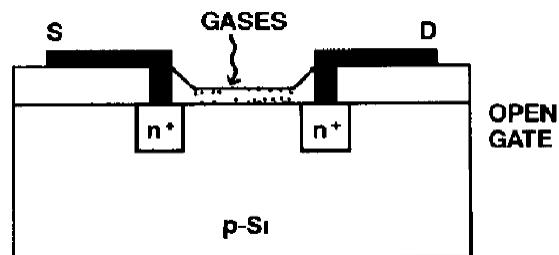


Figure 2.22: Schematic representation of a OGFET [32].

- **Ion Sensitive FET (ISFET).** It is similar to a normal MOSFET but the oxide is replaced by an oxide-electrolyte system (fig.2.23). Both sensitivity and selectivity depend on the properties of the interface between the insulator and the electrolyte. It may be also required to apply modifications to the insulator surface to achieve specific sensitivities, by employing ion implantation or by a chemical treatment [32].

The main limitations of this device consist in the need for an encapsulation membrane, which leaves exposed only the gate, to protect the structure from humidity induced degradation and is hardly compatible with microtechnology, and the high fabrication costs [32].

- **Chemically sensitive FET (CHEMFET).** A CHEMFET can be considered as a variation of a ISFET, in which a coating consisting of an organic membrane is introduced (fig.2.24). This device therefore combines a conductive

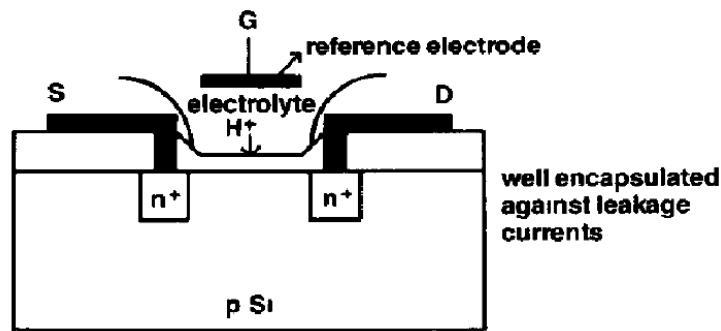


Figure 2.23: Schematic representation of a ISFET [32].

chemical sensitive layer to a potential-sensitive FET structure. The membrane is fabricated by a simple dip coating process in a suspension of the organic material. Unfortunately the sensitive membrane could represent a problematic issue for CHEMFETs, since it may undergo loosening and detachment which is a serious limitation for the life-time of the device [32].

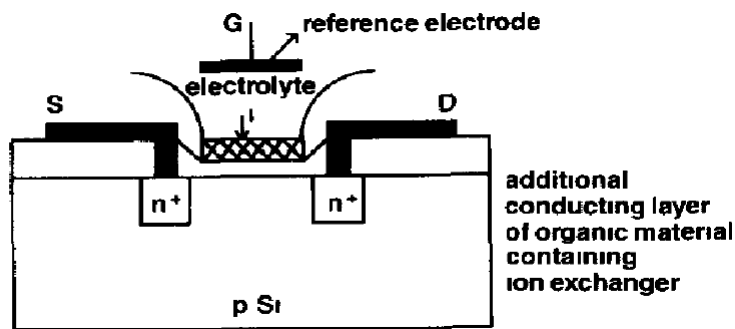


Figure 2.24: Schematic representation of a CHEMFET [32].

Several advantages characterize MOSFET sensors since they can be produced through microfabrication techniques, resulting in good reproducibility, possibility of integration in CMOS technology and low fabrication costs. However they can suffer from drift and instability problems depending on the sensing material used, and it is strictly necessary to control the environment in which the sensor operates, since its sensing properties can be easily influenced by humidity and temperature variations [1].

## 2.2.6 Calorimetric sensors

This class of devices exploits thermal energy variations as the way to detect physical or chemical changes induced by the presence of a gas. The reasons behind this

choice can be found in heat exchange intrinsic characteristics. In fact, whenever there's a chemical interaction between a solid surface and a molecule, some energy is exchanged in the form of heat, so if this surface belongs to a sensor system, the heat flow can provide an instrument for monitoring the process. On the other side, differently from the sensing mechanisms described in the previous sections, heat is always accompanied by dissipative phenomena, which induce a loss of information [34]. These devices are characterized by highly reduced costs of fabrication, but they generally provide a slow response [17]. Two configurations exploit this thermal technology.

### 2.2.6.1 Pyroelectric sensors

The sensors generally consist of micro thermometers constituted by a semiconductor body with a temperature-depending conductivity, coated with a catalytic layer, that absorbs the analyte of interest. Detection of a gas occurs by recording the heat coming from the reaction of the analyte with the coating. The concentration of the absorbed gas is proportional to the quantity of heat generated [17].

### 2.2.6.2 Pellistor sensors

They typically consist of a catalytic bead, with a diameter lower than a millimeter, surrounding a thin coil of Pt wire, which acts as a resistance thermometer. When the coil is heated at temperatures close to 500 °C, if getting in contact with a hydrocarbon, the catalytic oxidation of the analyte is induced, with the consequent release of heat. This heat is localized to the surface of the bead, and part of it gets lost in the surrounding, while the remaining part is detected. This last is responsible for a temperature raise in the sensor, which is in turn detected by the Pt wire and is translated in a change in its resistance. To measure the resistance changes with a good accuracy, the sensor is usually placed in a Wheatstone Bridge, that is an electrical circuit composed by four resistors, three having a known resistance value, and the fourth representing the unknown element to measure [17].

As an alternative to the Wheatstone Bridge, an electronic control circuit can be employed. It keeps the resistance fixed to a constant value, and it detects the amount of energy which needs to be provided to keep the sensor in this predefined condition, which results to be lower when a reaction occurs at the sensor's surface. Pellistors are less temperature sensitive than pyroelectric sensors, but they tolerate much higher temperatures and exhibit a better long-term stability [17].

## 2.2.7 Amperometric sensors

This class of devices exploits amperometry, an electrochemical analysis in which the signal of interest is a current which linearly depends on the concentration of the

analyte. The structure of the devices consists of a cell, containing three electrodes dipped in an electrolyte, named working, reference and counter electrodes (fig.2.25) [35].

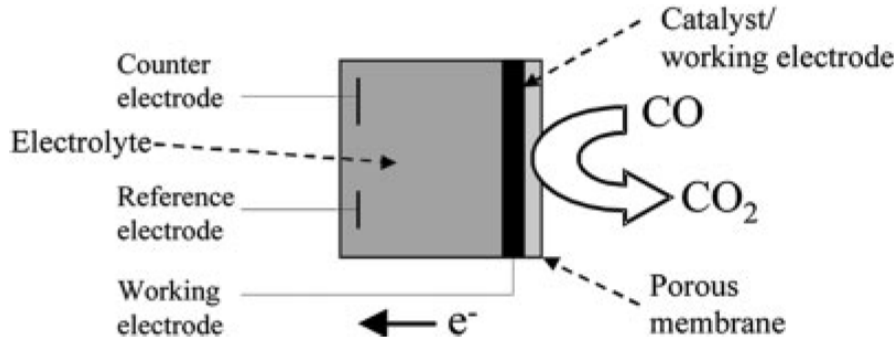


**Figure 2.25:** Schematic representation of an amperometric sensor [17].

As the analyte approaches the working electrode, it gets oxidized (electrons are transferred from the analyte to the working electrode) or reduced (electrons are transferred from the working electrode to the analyte). This charge transfer mechanism is measured as a current and its direction depends on the properties of the analyte and can be controlled through the electric potential applied at the working electrode. A counter reaction occurs at the counter electrode to maintain charge neutrality within the sample, and a current flows between it and the working electrode [35]. The relation between the rate of reaction and the measured current can be described through equation 2.25 [17]

$$W = \frac{QM}{Fn} \quad (2.25)$$

where  $W$  is the mass of the substance,  $M$  is its molecular mass,  $Q$  is the charge per unit electrode area,  $F$  is the Faraday's constant and  $n$  is the number of electron equivalents per mole of the analyte. It is therefore evident the proportionality relation between current ( $dQ/dt$ ) and the amount of analyte  $W$  supplied to the working electrode, which is in turn related to its overall concentration [17].

Selectivity of the sensor can be tuned by choosing different potentials, electrolytes, working electrodes catalysts or by applying selective membranes.

Measured current values range between  $\mu A$  and  $pA$  for ppm level reactants, while response times range from milliseconds to several minutes according to the gas [17]. The main advantages of amperometric sensors refer to high sensitivities, good control over selectivity, reduced costs and sizes, fast response times and long lifetimes [35].

## 2.2.8 Analytical approaches

As an alternative to all the detection mechanisms discussed in the previous sections, different analytical approaches can be employed. They allow to gain a larger amount of information, but their implementation is not always simple, since they are expensive, bulky and non-portable. The main examples are reported.

### 2.2.8.1 Mass Spectrometry

Mass spectrometers can be employed as devices for the identification of pure chemicals. In these sensors, the compounds get ionized through interaction with reagent ions or through thermoionic emission of electrons, and the resulting molecule ions are then separated according to their mass-to-charge ratio ( $m/q$ ) through the application of electric and magnetic fields. The ions finally collide at an electron multiplier, which provides amplification of the signal, and the current is measured. Although mass spectrometers provide a high accuracy and are able to detect analytes which couldn't be sensed with conventional techniques, their operation requires a vacuum environment, leading to increased costs and sizes [8].

### 2.2.8.2 Ion Mobility Spectrometry

It works following the same principle of mass spectrometers, but the separation of target molecules according to differences in their mass-to-charge ratio is complemented by differences in mobilities. This means that different collision cross sections, depending on size and shape, have an influence on the separability of ions. To induce ionization, it is possible to employ radioactive  $\beta$  emitters or UV photoionization. In both cases, after a series of ion-molecule reactions, a molecule with a high proton affinity reacts in humid air under proton transfer to a positively charged ion [8].

After ionization, ions are pulsed into a drift tube, isolated from atmospheric air, which through a uniform weak electric field induces an acceleration. The movement is slowed down by collisions, until ions reach the detector at the end, generating a current which is measured over the time of flight. In this way, information about analyte concentration and identity can be obtained.

Since collisions with ambient air are used, there is no need for vacuum [8].

### 2.2.8.3 Gas Chromatography

In gas chromatography, a column consisting of a capillary tube with an inner diameter in a range from 25 to 250  $\mu\text{m}$  and a length from 1 to 30 meters is employed. The inside wall of the column is coated with a thin polymeric film. As the analyte travels down the tube, it interacts with the film, which blocks its

motion towards the outlet. The transport time delays of the various molecular constituents of the gas, vary with their physical and chemical properties, like boiling point, vapour pressure, polarity or polarizability, causing them to separate as they emerge from the outlet. In this way, the transport time delay generates a molecular spectrum of constituents. A sensor is placed at the end of the column and it generates a current response as soon as each constituent gas, emerges [2].

To increase separation speed, different parameters can be adapted, like increasing the gas flow rate, reducing the thickness of the stationary phase or using a faster carrier gas. It is important to balance these variations, in order to avoid problems regarding sensitivity and costs [8].

It is possible to combine the gas chromatography with a mass spectrometer. In this case, the molecules emerging from the outlet of the column can be fragmented in the mass spectrometer to produce a characteristic pattern which improves their identification. The spectra resulting from the analysis are compared to a set contained in a database to help the identification of the specific chemical compound [2].

#### 2.2.8.4 Infrared Spectroscopy

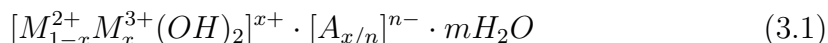
Through this technique, upon interaction of infrared light with the analyte, molecular vibrations and high energy levels are excited. Analysing the resulting characteristic absorption bands, the type of chemical bonds can be determined, and chemicals can be identified by a unique fingerprint spectrum. Two methods are currently employed for gas detection [8]:

- *Photoacoustic Infrared Spectroscopy.* A modulation of the intensity of an infrared source induces a temperature variation and the resulting expansion and contraction of the gas is measured as audible frequencies with a microphone.
- *Filter-based Infrared Spectroscopy.* The absorbed energy of a narrow band-passinfrared beam is measured.

## Chapter 3

# Layered Double Hydroxides

Layered double hydroxides (LDHs) represent an emerging class of 2D lamellar materials belonging to the group of hydrotalcite-like (HT) compounds, or anionic clays. [36] LDHs are characterized by a lattice structure consisting in the stacking of charged brucite-shaped layers containing divalent metal ions  $M^{2+}$  (e.g.  $Ca^{2+}$ ,  $Zn^{2+}$ ,  $Mg^{2+}$ ,  $Ni^{2+}$ ) occupying the centers of edge-sharing octahedra, surrounded by six  $(OH)^-$  hydroxyl groups. Part of the divalent cations are substituted by trivalent metal ions  $M^{3+}$  (e.g.  $Al^{3+}$ ,  $Fe^{3+}$ ,  $Cr^{3+}$ ,  $In^{3+}$ ), leading to the formation of positively charged sheets. To maintain the global electrostatic neutrality, the positive charge needs to be compensated by the presence of exchangeable anions  $A^{n-}$  (e.g.  $CO_3^{2-}$ ,  $Cl^-$ ,  $SO_4^{2-}$ ) between the layers together with  $H_2O$  molecules. The overall formula describing the LDH structure can be written as [37]:



where

- $M^{2+}$  and  $M^{3+}$  are the divalent and trivalent cations respectively;
- $A^{n-}$  are the organic or inorganic anions;
- m is the number of interlayer water molecules;
- x is the surface charge determined by the molar ratio  $M^{3+}/(M^{2+} + M^{3+})$ , and it is generally in the range 0.2 – 0.33.

It is evident from 3.1 that a wide variety of materials with different properties can be obtained by changing the nature of the two cations, their molar ratio or by inserting in the interlayer different molecular anions. These possibilities make

LDHs suitable for a wide range of applications (see section 3.5). The lamellar structure of the material is depicted in fig. 3.1 .

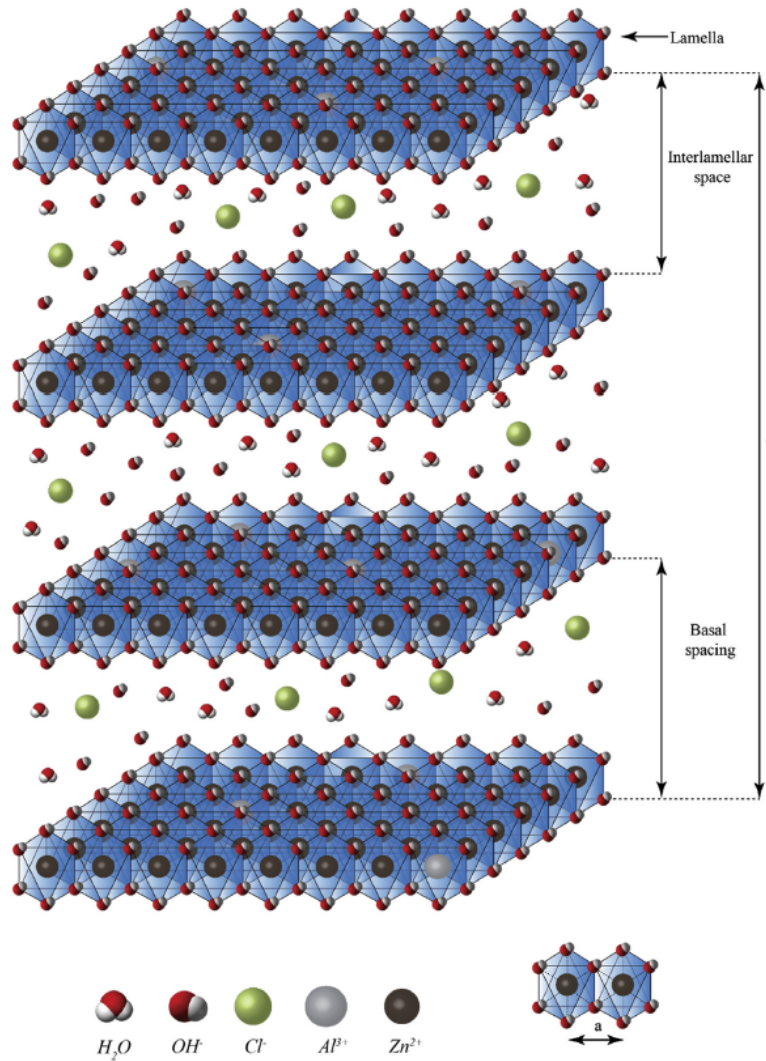


**Figure 3.1:** Representation of the LDH structure. The present example involves  $Zn^{2+}$  and  $Al^{3+}$  as cations and  $Cl^-$  as the intercalated anion. It is possible to notice the central metallic atoms surrounded by the hydroxyl groups shaping the various lamellas and the repetition of lamellas forming the overall LDH structure. As an addition, the cell parameters (here named  $a$  and  $c$ ) are indicated [38].

### 3.1 Synthesis of Layered Double Hydroxides

The synthesis of LDHs represents a simple and inexpensive process. A wide range of processes and techniques can be implemented, according to the specific physical and chemical properties that the material should possess to be suitable for the designed applications. A general overview of the most common synthesis methods is here provided [39]:

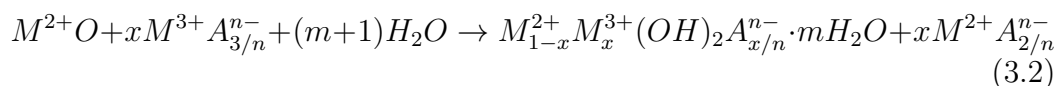
- 1) **Coprecipitation:** it allows to achieve the direct synthesis of LDHs with a wide range of possible interlayer anions. Although several variations can be applied to the process, four essential components are always required [40]:
  - a soluble source of divalent cations;
  - a soluble source of trivalent cations;
  - a source of interlayer anions, generally in the form of a soluble ionic compound (i.e.  $NaNO_3$ ,  $Na_2CO_3$ );
  - a base strong enough to cause precipitation of the LDH.

In the most general synthesis procedure, a base is added to an aqueous solution containing the suitable amount of  $M^{2+}$  and  $M^{3+}$ . The process should be carried on at constant pH to obtain LDH with a high chemical homogeneity. This technique leads to the formation of materials characterized by high crystallinity, small particle size, high specific surface area and high average pore diameter.

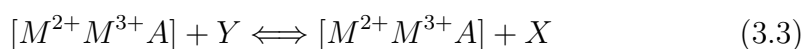
In the standard coprecipitation method, supersaturation of the precipitating agent is reached rapidly and maintained during the reaction, inducing the continuous nucleation of mixed hydroxides simultaneously with the growing and aggregation, leading to a wide particle size distribution. The process can be improved by using a base retardant as precipitating agent, so that the nucleation step is separated from the particle growth. The best choice lies in urea ( $CO(NH_2)_2$ ). The so-called "urea method" allows to control the pH through the rate of the hydrolysis of urea to ammonium ions, which is highly dependent on temperature. It is particularly well suited to the preparation of LDHs with a high charge density. Between the disadvantages, the LDHs prepared through this method contain some carbonate anions in their interlayers, being carbonate a product of the urea hydrolysis reaction [40].

The coprecipitation method may be limited by competitive reactions like precipitation of metal salts in the case of oxoanions with high metal ion affinity.

- 2) **Induced hydrolysis:** Selected oxides containing divalent metal ions are contacted drop-wise with acidic solutions of trivalent metal salts. These solutions induce the progressive dissolution of the oxides, leading to the precipitation of LDHs when the pH is buffered by the oxide or hydroxide suspension. The mentioned reaction can be written as:



- 3) **Reconstruction:** this synthesis technique is based on the so-called "memory effect", that is the LDH containing a volatile anion is calcined into a mixture of oxides to be then re-hydrated in an aqueous solution containing the anion to be intercalated. Structure recovery is strictly related to temperature, rate and duration of the calcination step. The method is suitable mainly for the preparation of hybrid LDH with large organic anions, like dyes.
- 4) **Sol-gel method:** a certain amount of  $M^{2+}$  alkoxide is dissolved in ethanol and HCl, while a certain amount of  $M^{3+}$  acetylacetonate is dissolved in ethanol mixed with a small amount of HCl as well. HCl is needed to induce the complete dissolution. The second mixture is then added drop-wise to the first one, under stirring. The pH of the mixture is adjusted to 10 by drop-wise addition of ammonia. The mixture is kept in constant agitation and refluxed until the gel is obtained. With the present method, samples with larger  $M^{2+}/M^{3+}$  ratios and higher specific surface areas with respect to classical coprecipitation can be obtained, even though they show a lower degree of crystallinity.
- 5) **Anion-Exchange Reactions:** the lamellar structure of LDH is highly favorable to anion diffusion. This property can be exploited to prepare new LDH phases by anionic exchange reactions. The reaction can be expressed as:



The system is bivariant in isothermal and isobar conditions. The reaction is favoured for in-going anions with a high charge density. The best precursors for these reactions are nitrate and chloride containing LDHs. Also organic anions can be directly intercalated by exchange reactions on LDH precursors with inorganic anions.

This technique is simple from an experimental point of view, since in general it should just be necessary to proceed with the stirring of an aqueous suspension

of an LDH precursor in the presence of an excess of the salt of the anion to be intercalated. The pH of the reaction can be controlled so to favour specific exchanges, together with washing and drying conditions [41].

- 6) **Synthesis of LDH-based nanocomposites:** to incorporate a polymer in LDH it is possible to employ different methods, according to the specific choice of the polymer. Between the various possibilities there are: i) intercalation of the polymer with subsequent in-situ polymerization (i.e polyaniline (PANI)) ii) direct intercalation of polymer chains via coprecipitation (i.e poly styrene sulphonate (PSS)), iii) transformation of the host material into a colloidal dispersion and re-stacking in the presence of the polymer, iv) reconstruction of the LDH structure in the presence of the polymer.
  
- 7) **LDH with intercalated nanoparticles:** the overall structure is synthesized via reduction of nanoparticles with organic reagents (i.e glucose, ethanol, ascorbic acid) in the presence of the LDH. This method allows to obtain uniform crystals with a narrow range of diameters.
  
- 8) **Hydrothermal, Microwave and Ultrasound treatments:** these treatments can be applied to completed samples to control structural or textural properties. i) Microwaves can be used already during synthesis to accelerate both growing and aging steps leading to a higher degree of crystallization, specific surface area and porosity. The increase strictly depends on the duration of microwave exposure. The effectiveness of the treatment depends on the nature of the LDH structure, since charge distribution and the presence of water molecules in the interlayer space lead to a good absorption of microwaves, favouring long-range ordering. ii) Ultrasound irradiation leads to improvements in the crystallinity of the sample and in absorption capacities. iii) Hydrothermal treatment is used to increase both the crystallinity of the sample and ion-exchange rate of low-affinity anions. In addition, it provides beneficial effects on the chemical composition of LDH.

## 3.2 Properties of the LDH structure

To fully understand some of the properties that characterize the behaviour of LDHs, it may be interesting to provide a general description of specific features related to the material's structure. Here they are reported.

### 3.2.1 Cation and anion ordering

Exploiting XRD (X-Ray Diffraction) and XAS (X-Ray Absorption Spectroscopy) analysis techniques, it is found that LDH structures lack of long-range ordering. This comes from the characteristics of octahedral layers, which are compressed along the vertical axis (*c* axis as named in fig.3.1), and expanded along the plane. This compression is limited by the approach of  $\text{OH}^-$  groups shared among the edges. To ensure cation ordering in the structure, cation-cation repulsion should be minimized employing a counter rotation of the upper and lower octahedral triads. However this distortion is incompatible with the flatter of the layers along the *c* axis. For these reasons, ordering is observed only for cations having similar atomic radii (i.e. Mg/Ga), since they allow to avoid important octahedra distortions and further decreases of the OH-OH groups distance [42].

At the same time, even in the absence of long-range ordering, a high degree of local ordering is observed. In this condition,  $M^{3+}$  cations never take neighbouring positions. These features are consistent as long as the cation pattern is characterized by frequent defects. Defects responsible for these features can be of two types: i) cation vacancies or ii) substitutional defects, in which a  $M^{2+}$  cation may be substituted into a site which should ideally be occupied by a  $M^{3+}$  one [43].

The interlayer anions may also show a regular distribution. Results from structural studies point out two principal cases [44]: i) carbonate anions (i.e.  $\text{CO}_3^{2-}$ ) are positioned in the interlayers so that their oxygen atoms form hydrogen bonds with the  $\text{OH}^-$  groups of the various lamellas. This is characteristic of structures where the oxygen atoms of the anion are positioned at equal distances from the OH-sheets near the lines which join the hydroxyls of the adjacent layers. The same rules apply also for other anions arranged in a 2D triangle (i.e.  $\text{NO}_3^-$ ) ii) Sulphate anions, in which the basal oxygens of the tetrahedra form hydrogen bonds with hydroxyls of either the upper or the lower interlayer surface only. The same rules also apply to other anions with a similar structure, like  $\text{CrO}_4^{2-}$ .

Figure 3.2 illustrates the various cases.

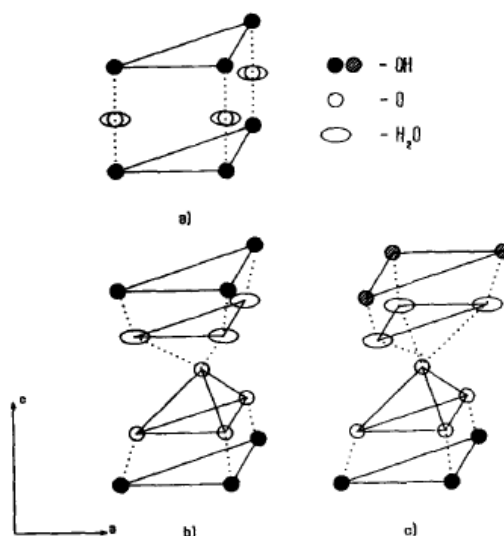


**Figure 3.2:** Arrangement of water molecules and carbonate (a) or sulphate (b and c) anions in the interlayers. OH represent the hydroxyl groups of lamellas and O are oxygens of interlayer anions. Dotted lines represent the hydrogen bonding net in the interlayers [44].

### 3.2.2 Cation-Anion interactions

In LDH, both electrostatic interactions and hydrogen bonding occur between the hydroxyl surface groups and anions. The interaction depends on the ordering of the metal cations in the layer and the chemical nature of the anions. In general oxoanions strongly interact with the hydroxyl surface groups, because of symmetry compatibility between the oxoanions polyedra and the octahedral layers. Optimal hydrogen bonds form when the  $\text{OH}^-$  units are arranged face to face or corner to corner. Strong interactions between the anions and the layers may lead to modification to molecular dynamic (as an example by intercalating  $\text{CO}_3^{2-}$ ,  $\text{SO}_4^{2-}$  or  $\text{ClO}_4^-$  into Mg/Al LDH, a lowering of the symmetry of the anions is expected because of hydrogen bonding with intercalated water molecules and  $\text{OH}^-$  groups) [39]. This is not the case of interlayer nitrate anions (i.e.  $\text{NO}_3^-$ ), which just slightly interact with interlayer water molecules or the hydroxide layers of the lamellas, leading to no visible change on the symmetry of the molecule [45]. If dealing with organic anions a strong interaction is expected because their anionic groups are hydrogen bonded to the surface hydroxyl groups, while their hydrophobic hydrocarbon chains are pushed away from the hydrophilic layer surface [39].

### 3.2.3 Thermal Stability

In general, LDH show a similar thermal decomposition behaviour even though they are characterized by a different composition. When heated, they tend to release the interlayer water up to a limiting temperature, usually close to  $250^{\circ}\text{C}$ , followed by dehydroxylation of the hydroxide layers and decomposition of the interlayer anions at higher temperatures. Although a certain amount of interlayer water is lost during heating, the layer structure remains stable, without collapsing [39]. An example of a TGA (Thermal Gravimetric Analysis) curve showing the mentioned mechanism is shown in fig.3.3.

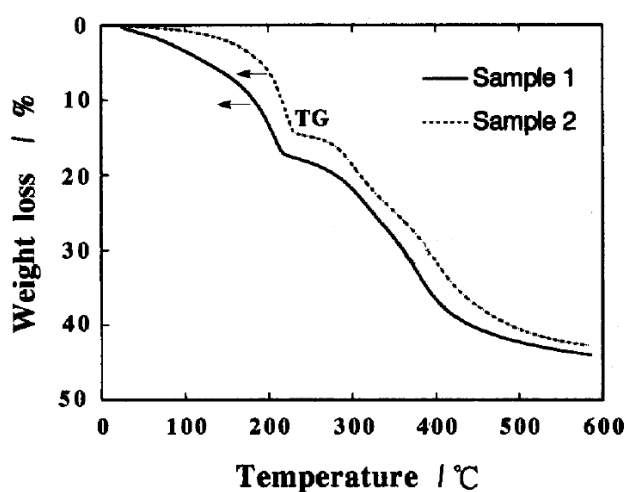


**Figure 3.3:** TGA curve of MgAl-LDH synthesised through coprecipitation (sample 1) and hydrothermal (sample 2) methods [46].

Thermal stability slightly changes according to the composition of the samples. In particular, it is found that it increases in the order  $\text{CoAl} < \text{ZnAl} \approx \text{CuAl} < \text{MgFe} \approx \text{NiAl} < \text{MgAl} \approx \text{MgCr}$ .

Also decomposition temperatures show small changes according to the specific LDH composition, as an example the highest value occurs for MgAl or MgCr LDH, around  $400^{\circ}\text{C}$ , while the lowest one occurs for CoAl around  $200^{\circ}\text{C}$  [39].

Thermal decomposition of LDH can also be affected by the nature of interlayer anions. A brief comparison can be performed between nitrate and carbonate forms of MgAl LDH, as an example. In both cases, a change in thermal stability is experienced, in particular, it increases with the increase of molar ratio ( $x$ ) in the case of nitrate forms, while the opposite occurs for the carbonate forms. This difference can be attributed to the arrangement of the interlayer nitrate ions [39]. There exist two options: i) when the  $x$  value is low, the anions adopt a "flat-lying"

configuration (fig.3.4a), that is they arrange parallel to the brucite-like layers. This configuration is possible because there is enough interlayer space to accommodate the low number of nitrate anions [47]. In this case, the hydroxyl groups in the layers are more similar, so  $NO_3^-$  anions experience a one-step continuous decomposition and the dehydroxylation and decomposition of nitrate anions occurs sequentially [48]. ii) When  $x$  reaches a certain threshold, the gallery space is insufficient for all nitrate anions to be accommodated in parallel to the layers, so that the strong repulsion among them forces a new orientation, named "stick-lying" configuration (fig.3.4b). In this case, nitrate anions alternatively stick to the top and bottom planes of the same gallery hydroxyl groups of the brucite-like layers, so that hydroxyl groups are divided into two classes, namely one which directly contacts with nitrate anions and the other which does not [47]. This arrangement induces the  $NO_3^-$  decomposition in two steps, leading to a discrete process. In this case, dehydroxylation and decomposition of nitrate proceed simultaneously [48].

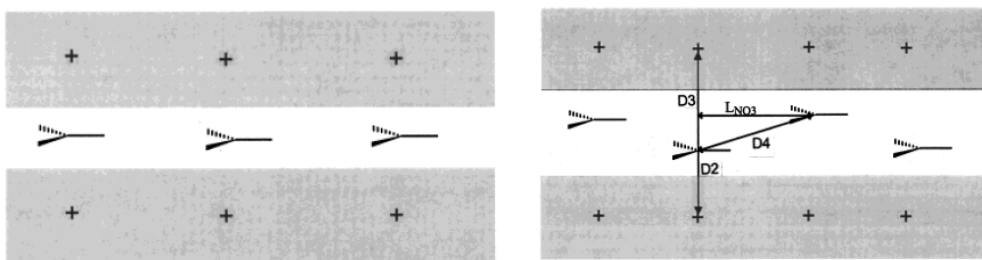


**Figure 3.4:** Schematic representation of a) flat-lying configuration b) stick-lying configuration [47].

As a further aspect, also grafting can modify the thermal stability of LDH. In fact, contraction of basal spacings is experienced when anions are grafted to the hydroxide layers, inducing an increase in the thermal stability [39].

### 3.2.4 Electronic properties

Before discussing the electronic properties of LDH, it may be useful to introduce a set of equations needed to determine the main quantities involved [49]:

- Band gap energy, that is the energy difference between the conduction band minimum and valence band maximum of the electronic structure

$$E_g = E_{CBM} - E_{VBM} \quad (3.4)$$

- The energy difference between the Fermi level and the CBM, defined as

$$x = E_{CBM} - E_F \quad (3.5)$$

By evaluating the band diagram of LDHs with different compositions, it is found that the Fermi level always falls in the forbidden zone, meaning that they can be classified as exhibiting a semiconducting behaviour. The  $E_g$  value shows little variations when changing the divalent and trivalent metal cations. As an example, for the same  $M^{2+}$ , Ga-based LDHs have smaller band gap energies than Al-based ones. This difference can be explained by the fact that Ga has 3d orbitals, differently from Al, which give a significant contribution both to the VBM and CBM, leading to a lower energy separation between the two. Similar considerations can be performed by varying the  $M^{2+}$  keeping  $M^{3+}$  fixed. In particular, Ni-based LDHs show the smallest band gap energy, followed by Co-based, Zn-based and Mg-based LDHs. Also in this case, differences come from electronic structure. In fact  $Mg^{2+}$  has no d-orbital and  $Zn^{2+}$  has a completely filled one, while both  $Co^{2+}$  and  $Ni^{2+}$  have unoccupied d-orbitals, leading therefore to smaller band gaps than the previous two [49].

By considering the  $x$  value (3.5), it is found that in all the cases, except for NiGa-LDH, the Fermi level is close to the VBM, meaning that NiGa-LDH is a n-type semiconductor, while the others are p-type semiconductors. Fig.3.5 shows some examples.

The n and p nature of LDHs determines the main charge carrier for electric conduction: in a n-type semiconductor, the number of free electrons is greater than that of holes, so electrons represent the majority carriers; in a p-type semiconductor instead the number of holes is larger than that of electrons, so that they represent the majority carriers.

As regarding other possible influences on the electronic structure, except for the choice of the cations, it is found that both molar ratio and the choice of interlayer anions do not lead to meaningful variations [49].

### 3.3 Morphology of LDH

According to the synthesis method chosen, LDH structures may be characterized by different morphological properties.

#### 3.3.1 Size and Shape

As mentioned in the previous sections, coprecipitation method leads to a high degree of crystallinity with a wide range of sizes. Sizes of the particles can be better

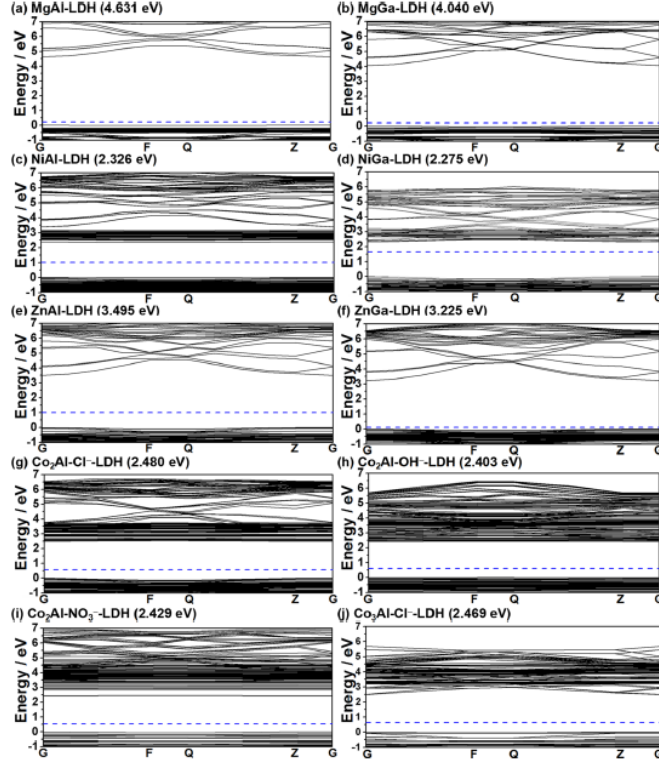


**Figure 3.5:** Band diagram of LDHs with different compositions. The dashed blue line represents the Fermi level [49].

controlled employing a hydrothermal treatment or precipitation by urea hydrolysis. Between the parameters which affect the size of the particles, total metal ion concentration, aging time, reaction temperature, precipitation rate and pH of the reaction need to be considered. From a theoretical point of view, the size of the product crystals as a result of a nucleation process can be determined by the following equation [50]

$$L = \left( \frac{cv}{8N} \right)^{1/3} \quad (3.6)$$

where  $L$  represents the crystal size,  $c$  is the concentration,  $v$  is the molecular volume and  $N$  is the number of crystal.

In general, as aging time is prolonged, the size of the particles increases, since particles may go through further crystal growth or intergrowth by the aggregation with other primary particles generating secondary particles.

As regarding temperature, its effect on the growth rate can be expressed as [50]

$$\frac{dL}{dt} = Ce^{-\frac{1}{RT}} \quad (3.7)$$

where  $C$  is a constant, and  $T$  is the reaction temperature. From 3.7 it is evident that a higher reaction temperature leads to a larger size.

Larger particles are also obtained when the precipitation rate is lower. A low precipitation rate is associated with a low degree of supersaturation, defined as [50]

$$S = \frac{c}{c_{eq}} \quad (3.8)$$

where  $c$  is the actual concentration of the supersaturated solution and  $c_{eq}$  is the equilibrium concentration of the saturated solution. It is possible to state that the nucleation rate increases uniformly with  $S$ , therefore a low degree of supersaturation results in a decrease in nucleation rate, that is in the number of crystal, inducing the formation of larger particles, as a consequence of 3.6.

This is the case of particles synthesized by urea method, since the slow hydrolysis of urea leads to larger crystal sizes, compared to those treated hydrothermally, as an example.

Particle size decreases as the total metal concentration increases. Recalling 3.6, it is evident that  $L \propto (c/N)^{1/3}$ . Once more,  $S$  is proportional to the concentration during the precipitation process in the supersaturated solution, so a higher concentration leads to an increase in the number of nuclei exceeding the critical nucleus radius  $r_c$ . These nuclei can participate to the crystal growth because they induce a decrease in free energy. In a highly supersaturated solution,  $r_c$  becomes smaller, leading to a large increase in the number of nuclei exceeding  $r_c$  compared with the increase in concentration. For these reasons, an increment in concentration leads to a reduction of crystal size [50].

All these features are summarized in table 3.1.

Aging time	Reaction Temperature	Total metal concentration	Precipitation rate	Size
↑	-	-	-	↑
-	↑	-	-	↑
-	-	↑	-	↓
-	-	-	↑	↓

**Table 3.1:** Summary of the influence of various parameters on the size of particles during LDH growth.

Figures 3.6, 3.7 and 3.8 provide an example of the effect of the various features just mentioned on the crystal structure of the material.

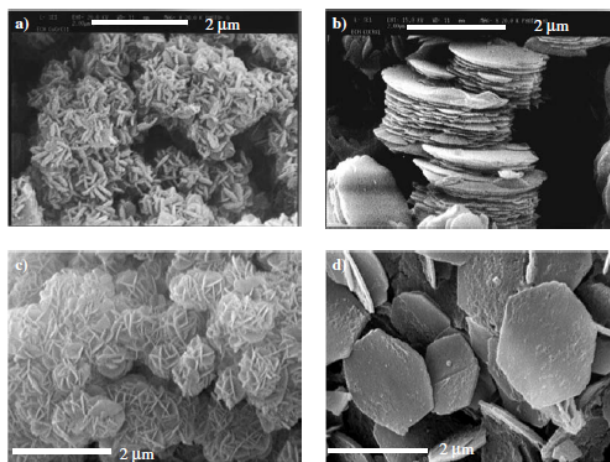


**Figure 3.6:** SEM images showing the comparison between LDH obtained through coprecipitation, induced hydrolysis and urea method. In detail: a)  $Cu_2Cr(OH)_6Cl \cdot 2H_2O$  prepared by  $CuO/CrCl_3$  induced hydrolysis, b)  $Cu_2Cr(OH)_6Cl \cdot 2H_2O$  prepared by coprecipitation, c)  $Mg_2Al(OH)_6(CO_3)_{0.5} \cdot 2H_2O$  prepared by coprecipitation, d)  $Mg_2Al(OH)_6(CO_3)_{0.5} \cdot 2H_2O$  prepared by urea method [39].

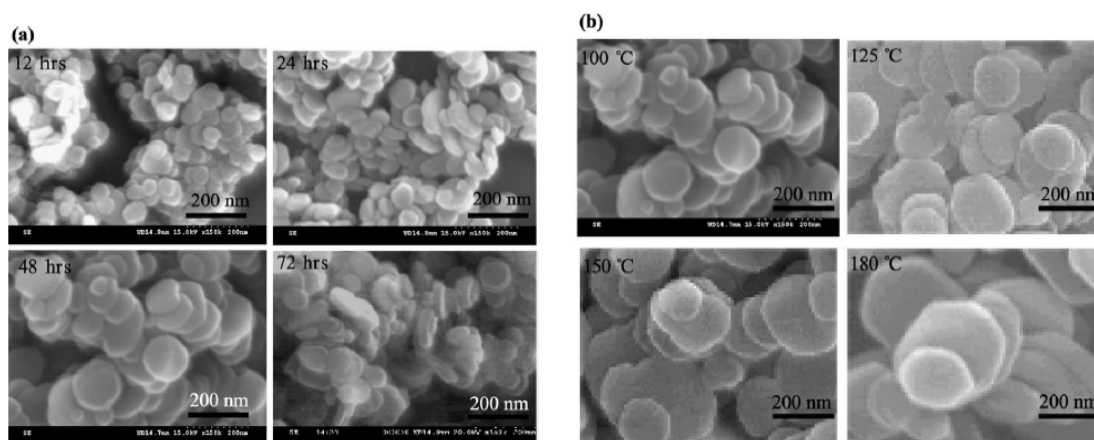


**Figure 3.7:** SEM images showing the effects on the particle size of a) aging time and b) reaction temperature on LDH synthesized by hydrothermal method. [50].

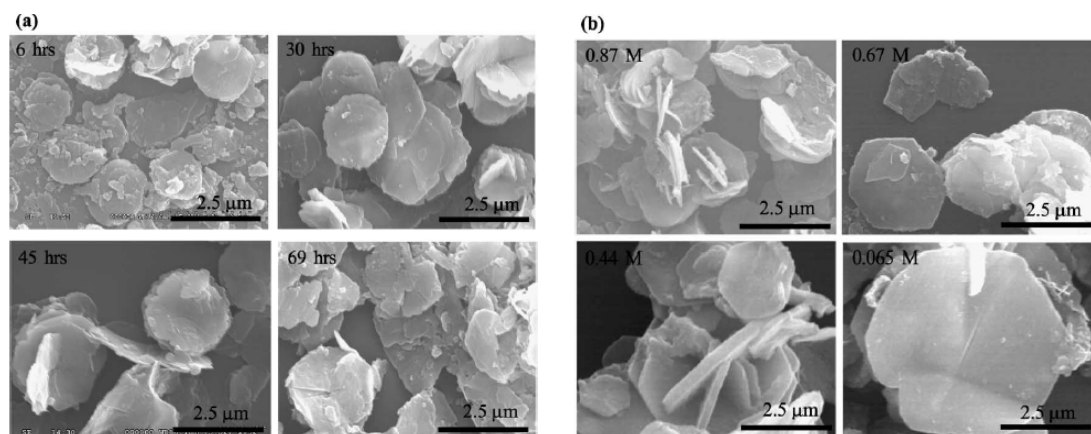


**Figure 3.8:** SEM images showing the effects on the particle size of a) aging time and b) concentration of metal ions on LDH synthesized by urea method [50].

### 3.3.2 Specific Surface Area and Porosity

The specific surface area of a single LDH layer can be expressed as [39]

$$S = a^2 \sqrt{3} 10^{-18} \frac{N}{M} \quad (3.9)$$

where  $N$  is the Avogadro's number,  $a$  is the cell parameter and  $M$  is the molecular weight of the unit formula.

The theoretical values calculated through 3.9 are usually large, (i.e. 1000 – 2000  $m^2g^{-1}$  for Al-based LDH), but experimental values obtained through the BET (Brunauer-Emmett-Teller) technique are much smaller (i.e. 80  $m^2g^{-1}$ ). This limitation arises because the internal surfaces are often inaccessible, because of a strong electrostatic interaction between positively charged layers and intercalated anions which leads to a tight stacking of sheets [33].

Several factors affect the specific surface of LDH, like the synthesis method employed, the type of solvents involved in the process, the specific composition of the LDH or the application of pre-treatments and thermal processes to the sample.

Synthesis by coprecipitation at constant pH allows to obtain LDH with a high level of crystallinity and purity, therefore it leads to an agglomeration of primary particles with a very low specific surface area. At the same time, the use of water/polar organic solvent media (i.e. water/alcohol medium with ethanol, propanol, isopropanol or ethylene glycol) for precipitation is an efficient way to enhance the specific surface area [33].

By comparing samples on which a hydrothermal treatment is performed to the others, a decrease in the specific surface area is observed in the first case. This happens because the treatment on samples induces a better crystallization compared to the un-treated ones, which are more amorphous with a larger surface area development [51].

Thermal decomposition of LDH precursors leads to the formation of a high surface area. The reason is found in the phases of the process; as an example, in the case of Mg/Al-based LDH intercalated to  $CO_3^{2-}$  anions, below a certain temperature  $T_1$ , weakly held water molecules of hydration are desorbed. At temperatures higher than  $T_1$ ,  $H_2O$  and  $CO_2$  are formed by dehydroxylation of  $OH$  groups within brucite layers and by decarboxylation of interlayer  $CO_3^{2-}$  respectively. In this condition, the evolution of these gaseous products creates a significant porous structure, which results in an increase in surface area.

In this framework, it is possible to provide an explanation to the larger surface areas related to higher amounts of Al in Al-based LDH: Al rich samples contain larger amounts of  $CO_2$  because higher  $CO_3^{2-}$  anions are needed to compensate the positive charge, causing larger surface areas [52].

As a final remark, it is possible to state that calcined solids show a large specific

surface area. The increase occurs up to a limiting value, above which a decrease is instead observed because of sintering or phase changes induced by the high temperature [53].

Porosity of the material is strictly related to specific surface area. The same considerations can be therefore performed, together with small additional comments. In particular, pore size and volume increase with calcination and thermal treatment induces the formation of pores with a more defined and regular size distribution and lower diameters [51].

In addition, as simple anions are replaced by more complex ones in LDH samples, porosity is enhanced [54].

Both surface area and porosity are key features which make LDH a suitable and interesting material for the realization of gas sensors, as it will be discussed later.

### 3.4 Sensing Mechanism

The good results in the use of LDHs as sensing material in gas sensors can be explained on the basis of the material structure, already mentioned in section 3.3. LDH structures are characterized by a peculiar arrangement of the layers so as to form a gallery pathway facilitating carrier diffusion transportation throughout the entire particle bulk, together with a high surface area and good permeability, strongly influenced by a high porosity.

These features appear to be beneficial in gas sensing applications to improve the response time, compared with polycrystalline metal oxide sensors, whose charge carriers need to overcome the energy barrier formed at the interface of adjacent grains by thermionic emission to maintain their movement from one grain to another.

The best performance of the material in gas sensing is achieved when the structure assumes a characteristic hierarchical 3D flower-like arrangement. To ensure this structure, the best  $M^{2+}/M^{3+}$  ratio should be chosen. If the molar ratio is too low, the structure is characterized by thick and irregular sheets with heavy stack induced by the high density of layer charge. If the molar ratio is too high, the low substitution of  $M^{3+}$  in the  $M^{2+}(OH)_2$  layers induces the formation of LDHs with a highly reduced porosity. If the molar ratio is set to its optimum value (generally dependent on the specific type of metal cations involved), a structure with a perfect hierarchical flower-like morphology is obtained. In this case thin LDH nanosheets assemble uniformly and connect to each other to form a stable and ordered architecture, with a high porosity [37]. Fig.3.9 shows examples of LDH structures in the three mentioned cases.

These features can be further enhanced during the synthesis process by employing

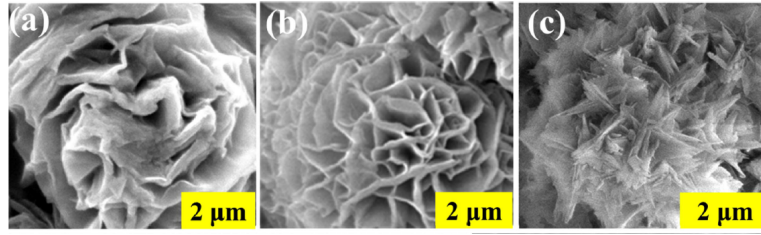
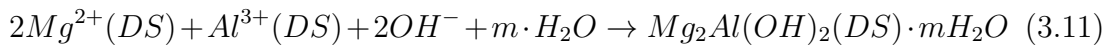
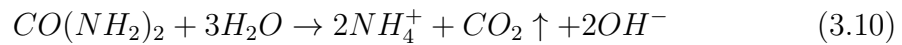


**Figure 3.9:** SEM images of LDH structures having a) too low molar ratio b) optimal molar ratio c) too high molar ratio [37]

sodium dodecyl sulfate (SDS) as template and intercalating agent to control the morphology of the LDH structure. The SDS molecule behaves as an anionic surfactant which has hydrophilic groups and can provide coordination sites when it is placed into an aqueous solution. To explain the formation mechanism of hierarchical structures in the presence of SDS, an example involving MgAl LDH is provided [55]. In aqueous solution, the  $DS^-$  ions self assemble into many spherical micelles;  $Mg^{2+}$  ions in the hydrothermal solution coordinate with the sulfated groups on the micelle surface because of electrostatic attraction. These coordination complexes further react with  $OH^-$  ions released by urea hydrolysis, forming LDH crystal nuclei attached to the spherical micelles. Under hydrothermal conditions,  $M(OH)_2$  brucite-like layers crystallize gradually from these performed LDH nuclei inducing a flower-like hierarchical structure. When  $Al^{3+}$  partially replaces  $Mg^{2+}$  during crystallization, the positive layers are formed. These layers attract the negatively charged sulfated groups, causing the intercalation of  $DS^-$  ions [37]. The chemical reactions involved can be described as [55]:



A graphical representation of the process is shown in fig.3.10.

Apart from the properties mentioned at the beginning of the sections, other comments should be provided regarding the good gas sensing properties of LDHs. It should be mentioned that the hydrogen bond between surface hydroxyl group and interlayer water molecules is equivalent to bridge connecting adjacent positively charged layers, leading to the formation of channels for the effective and fast transportation of carriers [56].

To explain the gas sensing mechanism, it is necessary to recall that, as mentioned

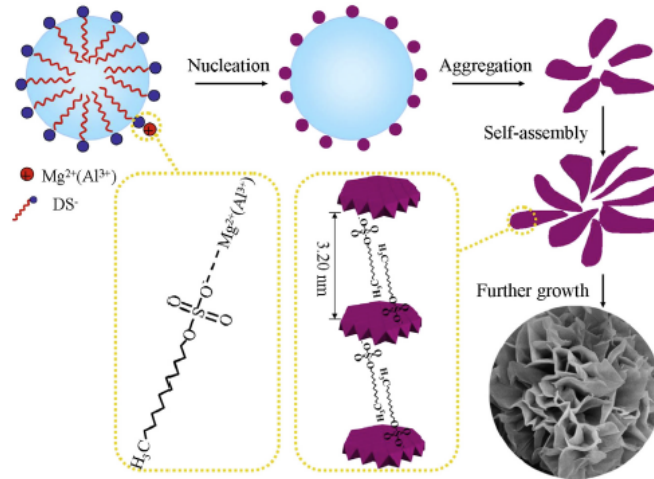


**Figure 3.10:** Formation mechanism for the 3D hierarchical flower-like MgAl LDH [55].

in section 3.2.4, LDH show a p-type semiconducting behaviour. The mechanism of gas sensing involves three steps, namely adsorption, charge transfer and desorption. When the LDH-based sensor is exposed to air, oxygen molecules are adsorbed on the surface of the p-type material and are ionized to form  $O_2^-$  by capturing surface electrons (eq.3.12 and 3.13), creating a hole accumulation layer (HAL) at the surface. This induces a decrease in the conductance and an increase in the resistance of the sensing material.

Upon exposure to an oxidising gas, because of its higher electron affinity, it withdraws free electrons from the LDH nanostructure (eq. 3.14) and at the same time it reacts with  $O_2^-$  (eq. 3.15), leading to an increase in the hole density, which translates in a rapid decrease in resistance.

An example of the process described is provided, considering the case of CoAl-LDH used to detect  $NO_2$  [56]:

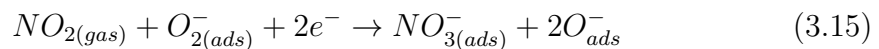
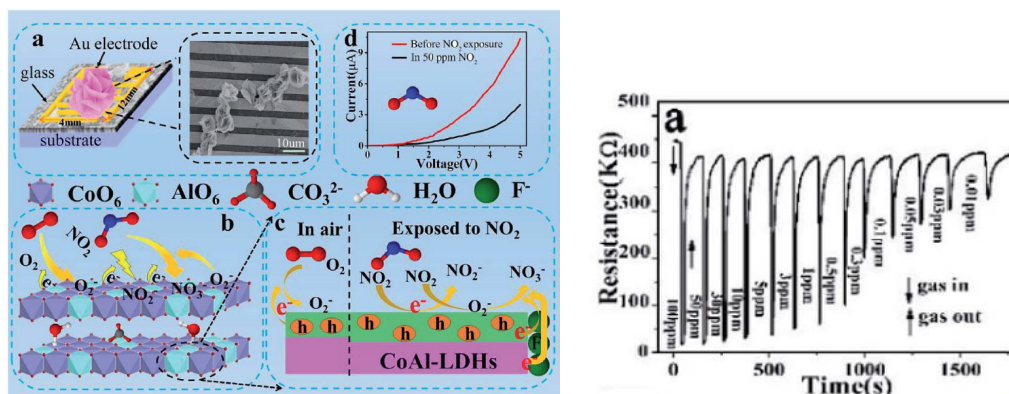


Fig.3.11 shows a schematic of the gas sensing mechanism described.



**Figure 3.11:** Schematic of gas sensing mechanism of  $NO_2$  for CoAl-LDH sensor and related response curve [56].

The opposite situation occurs when the material is exposed to a reducing gas: a decrease in the hole density is induced, with a consequent decrease in conductivity and increase in resistance.

Briefly summarising, the good gas sensing performance at room temperature for LDH-based sensors can be related to two main factors: i) the morphology of the material, which provides several diffusion channels, enabling a fast diffusion of the gas also in the internal part. ii) The high porosity, which enhances not only diffusion of the gas, but also adsorption. In fact, the gas can be adsorbed at the outer and inner surfaces and on the entire porous walls. iii) The large specific surface area provides a large number of active sites for adsorption, leading to a high response [56].

### 3.5 Applications of LDH

The simplicity in the synthesis processes, the use of cheap and non-harmful precursors, the ability to work without limitations in a wide range of environmental conditions, together with all the features analyzed in the previous sections, make LDHs very appealing materials to be employed in a wide range of applications. Their application in the realization of gas sensors has already been discussed, so a brief summary of other potential uses is also provided.

- **Catalytic Applications.** LDHs possess a wide range of features that make them good catalysts and catalyst supports. Between the advantages, there's

the ease in removal of LDHs from the reaction mixture once a reaction has been catalyzed, and the possibility to recover them for next reaction cycles. In principle LDHs can be employed as catalysts according to four main strategies (fig.3.12) [57]:

- As supporting surface. The insertion of new species provides the material of a reactivity that it didn't possess. In this case, LDHs are used to achieve a chemical confinement, an enhancement of catalyst selectivity but there's no direct participation to the reaction steps.
- As a source of catalytically active species. LDHs are transformed in new materials with the required catalytic properties. The usual transformation occurs into mixed metal oxides as a consequence of a thermal stress, which induces the loss of the typical structural features of LDHs. It is therefore a useful choice when the lattice is limiting the interaction between the metal centers and the reactants.
- As absorbers. The catalytic species are absorbed in the interlayer galleries and can be then exchanged with the external environment. LDHs act therefore as a reservoir or create a catalytic environment, but the active role is due to another chemical species.
- Pristine LDH. The catalytic properties belong to the material as it is, without any inclusion of other species.

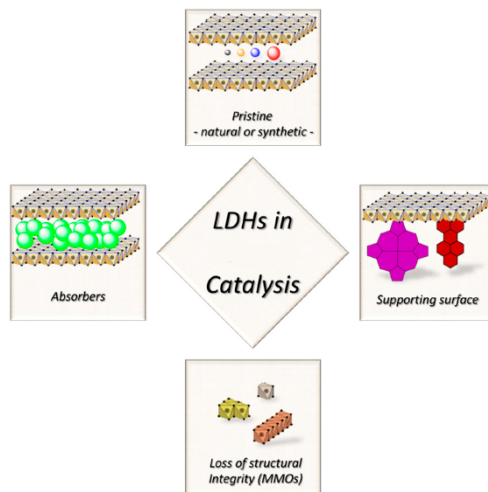


**Figure 3.12:** Different approaches for the development of LDH-based catalysts [57].

- **Medical applications.** A first example consists in the use of LDHs as antacids for the treatment of gastric or duodenal ulcers, because of their

prolonged buffering effect and their bile-bending ability [39].

LDHs are also successfully employed in the design of drug delivery systems, due to their biocompatibility, pH-dependent stability, ability to intercalate a wide variety of biomolecular anions and low toxicity. In this case, it is necessary the realization of inorganic-organic hybrid materials in which bioactive species are stored in the interlayer space, protected from light and oxygen, and can be released after an appropriate chemical signal. Drug-intercalated LDHs dispersed in biological fluids with  $\text{pH} \sim 7$  can release the guest species via ion-exchange reactions, with a release rate which depends on factors like drug shape and size, arrangement of drug anions in the interlayer region, selectivity of the LDH towards the anions in the release medium, dimension of the LDH particles and specific layer composition. LDHs can also improve the solubility of the drug, in fact in a medium at acid pH, the LDH structure slowly dissolves and the drug is released anion by anion in the medium [58].

- **Additives fro Polymers.** Synthetic LDH can be used as acid neutralizers or HCl scavengers in stabilizer packages for PVC. The reaction between HCl and LDH occurs in two steps, namely the interlayer anions react with HCl and then the LDH decomposes, giving rise to metal chlorides.

LDHs are also employed as flame retardants in polymers. They are preferable from an environmental point of view to halogen-based solutions, moreover they show a superior performance compared to other inorganic hydroxides, like magnesium and aluminum hydroxides.

For these applications, to achieve a good mixing between polymers and additives, the LDH/polymer nanocomposites are synthesized by templating or by in-situ polymerization. In the first case, the synthesis is computed by coprecipitating LDH in solution in the presence of soluble polymers. Formation of LDH and the incorporation of the polymer occur simultaneously. LDHs are good materials for templating because they can be synthesized at room temperature or under conditions which do not cause polymer decomposition. In the second case, polymerization consists of intercalating monomer anions or polar monomer molecules followed by polymerization. In this case, appropriate monomers should be used [39].

- **Environmental Applications.** When dealing with solutions to treat pollutants, LDHs can eliminate a variety of contaminant and toxic substances directly from the environment through anion-exchange, reconstruction and adsorption. They can be also employed to remove metal cations from aqueous solutions. In the case of transition metal cations, the process consists in a substitution with another cation, achieved by shaking the mixture of an aqueous solution of the appropriate salt and the chosen LDH at room temperature.

As a second possibility, the buffer effect is employed, that is adding a specific LDH to aqueous solution leads to an increase in pH which causes metal cations in the solution to precipitate as metal hydroxides [39].

- **Future Trends.** The use of LDHs as materials in the realization of biosensors is a field worth exploring because of their excellent biocatalytic properties and the possibility of producing hybrid materials with enzymes. It is in fact possible to realize hybrid LDHs containing redox active molecules as enzyme immobilization matrices.

Realization of new functional materials, through intercalation into LDHs is another possible promising future trend. Examples are intercalation of fluorescent anions or luminescent anions into LDH matrices, or intercalation of  $C_{60}$  followed by co-intercalation with toluene or hexane into organo-LDH to enhance materials' photoluminescence [39].

## Chapter 4

# Development of LDH based gas sensors

The sensors for this thesis work were designed and optimized in order to specifically work with LDH as sensing layer. The aim is to realize an array of electronic devices, with a minimum of two individual units, each characterized by LDH having a different chemical composition, capable of detecting a specific gas, so as to achieve a basic version of an e-nose. Four different LDH compositions were employed and characterized to test their performances in gas sensing: ZnAl-Cl, ZnFe-Cl, ZnAl-NO<sub>3</sub> and MgAl-NO<sub>3</sub>.

Each individual sensor consisted of Au interdigitated electrodes (IDEs) deposited on top of a Silicon wafer provided with a thin layer of oxide obtained through a thermal oxidation to work as an insulating substrate, and of the LDH sensing layer. The following section provides an overview on the techniques commonly employed to fabricate and characterize LDH-based gas sensors and a specific focus on the devices designed and realized for this thesis work.

### 4.1 Deposition of the sensing layer

As mentioned in the previous chapters, the sensing layer is the key element which allows the sensor to interact with the analyte and provide a response. In section 3.4 the peculiar properties of LDHs which are responsible for their promising applications in gas sensing have been described, in particular their hierarchical ordered 3D structure and porosity. It is therefore important to optimize the deposition process in order to enhance these behaviours, so as to lead to the best performance for the sensor.

As literature suggest, LDHs are a class of materials which can be easily deposited by employing a wide range of techniques, from spin coating [59] and dip coating [60],

to layer by layer self-assembly [61] or screen printing [62]. In this thesis work, four techniques are selected and analysed, chosen according to the available equipment or to specific features which may enhance the properties of the material, namely drop casting, spin coating, ink-jet printing and spray coating.

This section deals both with the preparation of the formulation to deposit and on the characteristics of the selected deposition techniques.

#### **4.1.1 Preparation of the solution**

In order to proceed to the deposition of the material to form the sensing layer, a stable suspension of LDHs in a proper solvent should be obtained. LDHs synthesized through the conventional techniques described in section 3.1 show an intrinsically hydrophilic nature, due to their characteristic high surface charge resulting in the adsorption of water molecules on the surface of each layer. For this reason, they can be dispersed in polar solvents only [63]. However, several approaches exist to modify the property of the surface of LDHs from hydrophilic to hydrophobic. As a first option, interlayer anions can be exchanged with organic surfactant anions, like dodecyl sulfate (DDS) or dodecyl benzene-sulfonate (DBS), which induce an increase in the interlayer spacing adding a hydrophobic phase between lamelle [64]. However this approach is not suitable for all the types of LDHs, so as an alternative a simple washing procedure using specific solvents may be employed. In this way, no modifications involve the LDH composition, structure and particle size, but it introduces an hydrophobic tendency to the nanoparticles. This variation occurs because after the washing step with proper solvents, the water molecules placed on the surface of LDH platelets are removed and substituted by molecules of the washing solvent [63].

Generally, a stable suspension of LDHs can be obtained by dispersing the material's powder either in distilled water or ethanol. According to the properties that the dispersion should possess to be properly deposited and lead to a sensing film of good quality, the mass fractions should be carefully controlled. An appropriate choice could be to disperse 5 mg of LDH powders into 0.1 mL of distilled water [65] or, alternatively in ethanol, leading to mass fractions (wt%) in a range from 5% to 6%, and to proceed with a sonication step for a few minutes (i.e. 5 minutes), so obtaining a suspension which is stable for a period up to 6 months [66].

#### **4.1.2 Drop Casting**

Drop casting represents a fast and simple deposition technique for small substrates, like in the present case, which makes possible to control the characteristics of the deposited film avoiding wasting of material. A drop of solution is deposited through a dispenser having a controlled diameter over the substrate, and it is evaporated

under controlled conditions of temperature and pressure (fig.4.1). Evaporation can occur simply by leaving the substrate under ambient conditions, or it can be induced by placing it over an heating element.

A limitation of this technique relates to possible non uniformities in the deposited film or variations in its thickness because of different evaporation rates.

No particular restrictions characterize this deposition technique, but employing solvents which are volatile and not subjected to de-wetting leads to a better quality for the deposited film. In general alcohols are preferred to the use of water as solvents.

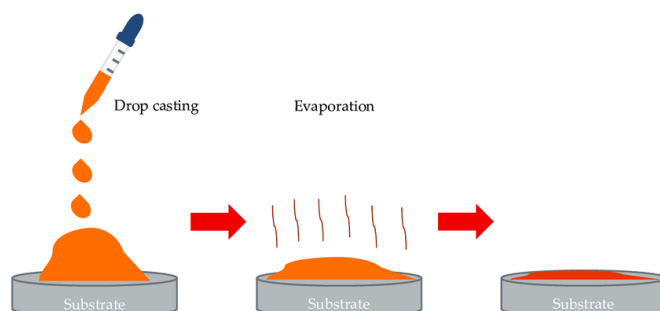


**Figure 4.1:** Schematic representation of a drop casting process [67].

When dealing with LDHs, a dispersion of the materials' powder in ethanol is preferred, and a small amount of the suspension ( $\sim 50 \mu L$ ) is dropped over the IDEs and it is dried at  $60^\circ C$  for 4 hours. The resulting film is characterized by a thickness which ranges between  $30 \mu m$  and  $40 \mu m$  [65].

The process should be controlled so that the dropped solvent spreads over the fingers and covers the whole sensing area, excluding therefore the contact pads.

When applied to this specific work, drop casting represents the best choice since it allows to deposit in a simple and fast way coatings of different LDHs components on the array of sensors.

### 4.1.3 Spin coating

Spin coating is one of the techniques mainly employed for the deposition of thin films characterized by a good uniformity. It allows to achieve a careful control over the thickness of the material being deposited and it is a fast technique, since only a few seconds per coating are necessary. The working principle will be explained in detail in Section 4.4.1 for the deposition of the photoresist: the process is performed inside a spin-coater, provided by a rotating platform over which the sample is fixed in a vacuum environment. A certain amount of solution is deposited on

top of the substrate, at its centre, and it spreads all over as a consequence of the centrifugal force arising through the rotation. By tuning the speed and duration of the rotation, the excess of solution is flung off the substrate leading to a film of the desired thickness. The process is completed after a drying step which evaporates the residual solvent (fig.4.2).

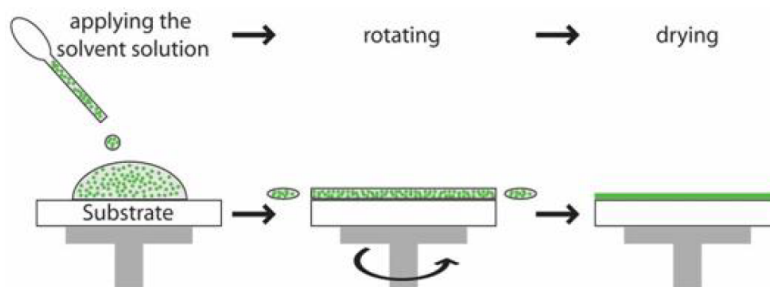


**Figure 4.2:** Schematic representation of a spin-coating deposition process [68].

This technique is characterized by some drawbacks as well. In particular, it involves a high wasting of material, in fact less than 10% of the solution remains on the substrate after centrifugation. Moreover it is not suitable for substrates with large dimensions and it requires rigid samples to guarantee the correct uniformity for the deposited film.

When dealing with LDHs, in a typical spin coating process, 50  $\mu\text{L}$  of the solution are dropped over the centre of the substrate, and the rotation of the plate occurs in two steps: 1) 600 rpm for 10 s, 2) 1500 rpm for 30 s. The resulting film is finally dried in a vacuum oven at 60°C for 4-5 hours. In this way, a thickness in a range of 40-50  $\mu\text{m}$  can be obtained [59].

#### 4.1.4 Ink-jet printing

This printing technique allows a direct patterning of the substrate through the ejection from a nozzle of droplets of a material in the form of a colloidal solution. Two main classifications for ink-jet printing exist, continuous (CIJ) or drop-on-demand (DOD). In the first case, a vibrating piezo crystal induces a continuous stream of drops, which are subjected to an electrostatic field that determines their direction. They are either deposited on the substrate or they are collected in a reservoir to be reused. CIJ is characterized by a high speed but it leads to a relatively low resolution. In the second case, drops are ejected from the nozzle only when they are required through the generation of a pressure pulse. According to the method employed to generate the pulse, three main categories can be identified: thermal ink-jet (fig. 4.3a), in which a resistive element located in the chamber containing the ink is heated causing the ink to vaporize so creating a bubble which induces

the ejection of the droplet; piezoelectric ink-jet (fig. 4.3b), in which the pressure pulse is mechanically induced through the deformation of a piezo crystal under the application of an electric field; electrostatic ink-jet (fig. 4.3c), in which drops are ejected under the influence of an electrostatic field acting between an electrode and the orifice of the nozzle. According to the ejection mechanism, different requirements may be necessary for the inks [69].

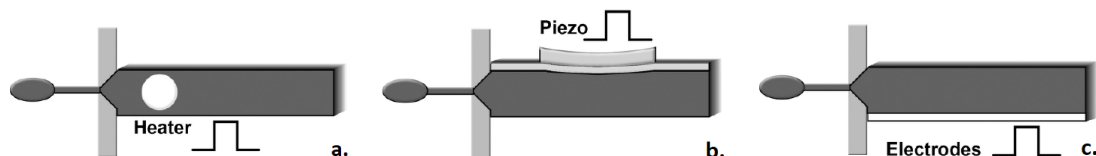


**Figure 4.3:** Schematic representation of the different categories of DOD ink-jet: a) thermal, b) piezoelectric, c) electrostatic [69].

Several advantages characterize ink-jet printing technique. In particular, the whole process can be carefully controlled so to realize patterns having a high resolution, and a low wastage of material occurs, since only the necessary droplets are ejected and the eventual residual solution is collected and reused.

As regarding the limitations, clogging of the nozzle because of ink particles aggregation close to the orifice is frequent, and it requires careful washing operations to be freed; moreover, only a restricted selection of inks is compatible with the requirements.

In order to avoid spreading of the deposited solution, leading to a low resolution pattern, surface properties of the substrates can be modified by employing a plasma treatment [70].

In the present case, the piezoelectric DOD ink-jet mode was considered. A pattern can be replicated on a substrate, which is mounted on a movable support, starting from a digital model, and it is obtained through the combination of arrays of droplets (fig.4.4).

As mentioned, inks employed in ink-jet printing should satisfy specific requirements to be compatible with nozzles. These include limitations on the sizes of the particles of the material dispersed in solvents, on viscosity and surface tension of the fluid. In this particular case, the considered instrumentation is a Microfab Jetlab 4, characterized by the following requirements [72]:

- *Particle diameter.* It should be lower than the diameter of the orifice, corresponding to  $50\ \mu\text{m}$ . As a limiting case,  $d_{\text{particle}} \geq 5\% d_{\text{orifice}}$  could be accepted only if the solution has a low concentration of particles, but some instability in drop generation may arise.

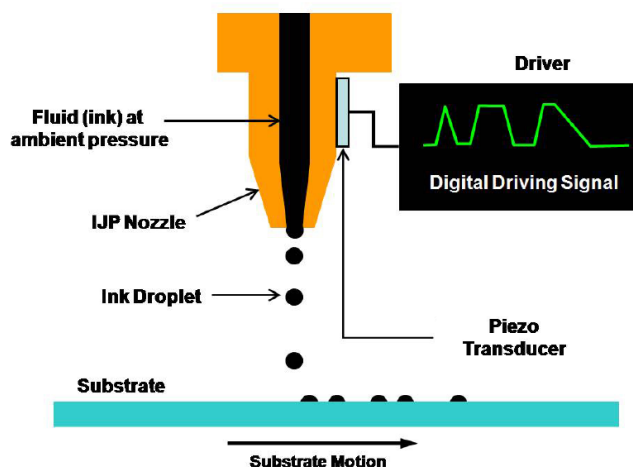


**Figure 4.4:** Schematic representation of the working principle of a piezoelectric DOD ink-jet printer [71].

- *Viscosity.* It should be in a range of 0.5 to 40 cP.
- *Surface tension.* It is limited between 20 and 70 dy/cm (0.02-0.07 N/m).

Fluids with properties which are outside these ranges may be eventually employed as inks, but with increased printing difficulty and lower performance.

LDHs dispersions appear to be suitable candidates to be employed as inks, being generally characterized by:

- sizes of particles vary according to the metal cations and to synthesis method employed, but being comprised in range from few nm ( $\sim 10$  nm) [73] to a few  $\mu\text{m}$  ( $\sim 5 \mu\text{m}$ ) [74]. Since the preparation of the solution involves a sonication step, no large aggregates of particles are expected, which may cause clogging of the orifice.
- Viscosity ( $\eta$ ) can be tuned by choosing appropriate solvents and it can be influenced by the size of the crystal plates, the post-synthesis treatments employed or the intercalated anions. Generally, for mass fractions up to 15%,  $\eta$  ranges close to 25 cP, and it increases for larger wt% values [75].
- Surface tension ( $\gamma$ ) is strictly related to the LDHs composition and to the concentration of the solution, and it varies between 69.5 dy/cm and 73.5 dy/cm [76].

Starting from the discussion on the characteristics of the sensing area which will be provided in Section 4.3, the pattern to print could simply consist of a rectangular

shaped element, having a width corresponding to the L parameter and a height equal to Y (fig.4.5).

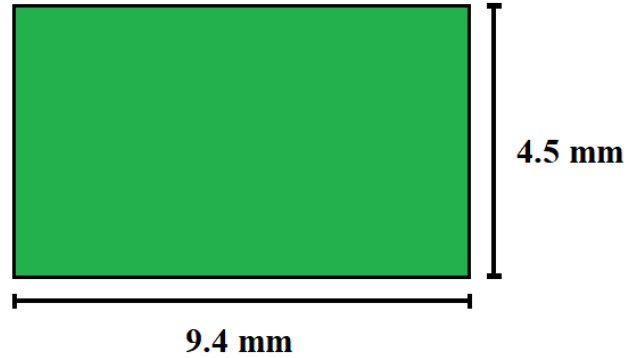


**Figure 4.5:** Pattern of the material to be deposited over the IDE structure.

#### 4.1.5 Spray coating

Spray coating represents a low cost technique for the deposition of thin films. As for inkjet printing, the process consists on the release and subsequent deposition and spreading of multiple droplets on a substrate. This technique is rapid and of easy application, but it is a stochastic process, so the control of the repeatability and uniformity of the deposited layers does not represent a simple task. It is possible to improve the controllability of the process by employing a plasma treatment on the substrate, by heating it or by imposing an ultrasonic vibration, which improve droplet spreading and mixing, leading to the formation of a more uniform and continuous film. As an alternative, an increase in the flow rate or in the number of spray passes should lead to a film having an better uniformity but a higher thickness [77]. Also in this case, the solution to deposit should fulfill specific requirements to be ejected from the nozzle. In addition, in order to obtain films with a precise pattern, a mask should be employed, to protect the areas which should not be covered by droplets of material and leaving exposed only the sensing area [78].

According to the process which induces the ejection of droplets from the orifice of the nozzle, several categories of spray coating can be identified. In thermal spray, a heating source is employed to heat the material present in a reservoir, so that the coating results from melted or partially melted particles [79]. The heating mechanism can either be combustion through oxygen and a fuel gas or the use of plasma, which is generated through an arc discharge. An alternative technique still belonging to the thermal spray category is cold spray, which consists in the release of a high pressure gas through a nozzle, whose particles are accelerated by

means of a supersonic steam at atmospheric pressure. A second category is aerosol deposition, also named vacuum kinetic spray. It is similar to cold spraying, but in this case the substrate is placed in a vacuum chamber which draws the atomized particles through a nozzle directed towards the substrate. This technique employs smaller particles compared to the others and it allows to work at lower speeds and temperatures and it induces a higher porosity in the deposited coatings, even though it is characterized by a low deposition efficiency [80].

When dealing with LDHs, cold spray is the best deposition choice, avoiding to heat the material which may cause alterations to its structure. The idea of using this technique is related to the characteristic lamellar shape and porosity of the deposited films [79], which could further enhance the intrinsic properties of LDH structures and induce an improvement in the gas sensing capability of the film, with higher sensitivities and faster response times. By recalling the discussion of the previous section, the dispersion of LDHs in suitable solvents leads to solutions fulfilling the compatibility requirements of these types of nozzles.

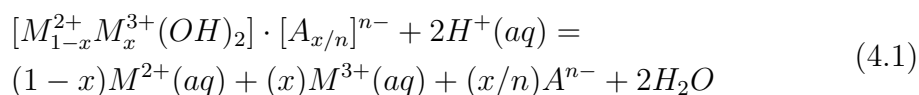
As mentioned, a mask should be employed to provide a correct definition of the pattern. The most common choice involves the use of shadow masks, placed at a certain distance away from the part to be sprayed, and in front of the spray stream, so protecting selected areas from it. In general the mask is not directly contacted to the substrate in order to avoid sticking between the two elements as the material is deposited [79].

A model of a mask suitable for the sensor designed in this work (as it will be discussed further on) is shown in figure 4.6. It is characterized by a pattern in which gaps correspond to the areas where the material needs to be deposited, while the rest of the structure is protected.

#### **4.1.6 Dissolution of Layered Double Hydroxides**

In some cases it may be necessary to pattern the already deposited film so as to achieve specific geometries. This operation is computed by employing an etching process.

LDHs tend to dissolve in acidic media specifically characterized by pH values lower than 5. A general expression for the dissolution process is represented by (equation 4.1) [81]



The reason behind this pH dependence can be found in the LDHs structures. In fact, they are characterized by surface hydroxyl groups which may undergo

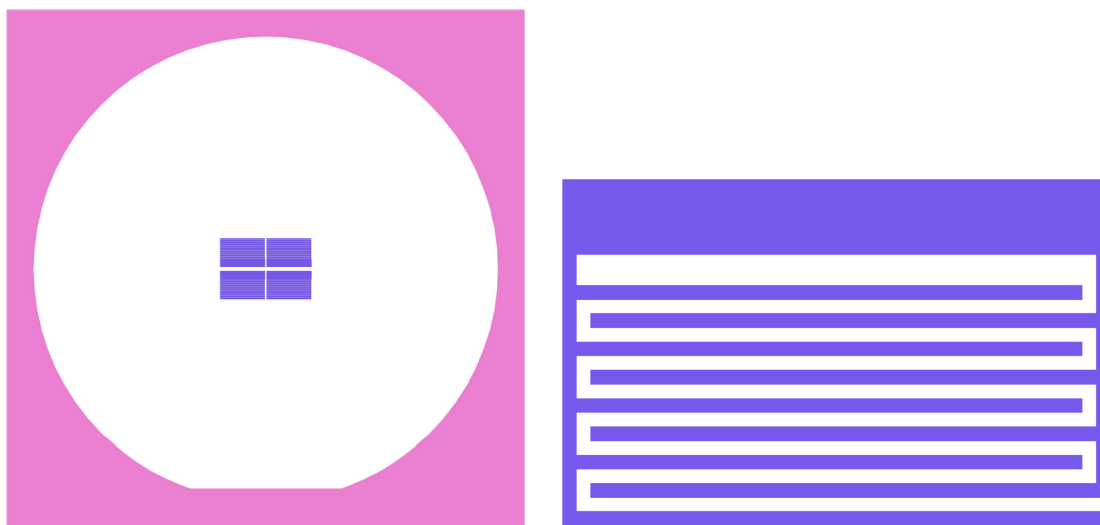


**Figure 4.6:** Shadow mask employed in spray coating deposition realized through CleWin5 software.

protonation/deprotonation reactions. Surface protonation increases the dissolution rate because it weakens the bond between metals and oxygen. When the pH is lowered, the concentration of the protonated sites on the material surface increases, as well as the dissolution rate. In principle, dissolution can be modeled as a two steps mechanism, initially involving a quick surface acid-base equilibrium, followed by a slow detachment of the metal cations from the protonated active sites [82].

The specific metal cations have an influence on the dissolution of the material. In particular, the degree of solubility of LDHs is found to be maximum when the divalent metal cation is  $Mg^{2+}$ , and it lowers when dealing with  $Co^{2+}$  or  $Ni^{2+}$ , while for trivalent metal cations,  $Al^{3+}$  shows a higher solubility tendency than  $Fe^{3+}$ . This behaviour is related to the free energy, in fact the larger the negative value of the free energy of the dissolution reaction, the more soluble the LDHs tend to be. Similar observations can be performed for different interlayer anions, whose nitrate and sulfate forms induce increases in solubility [81].

Dissolution is mainly achieved by employing a nitric acid solution ( $HNO_3$ ). It allows to carefully control the whole process, since at first only small vacancies are formed, generally obtained by removing divalent metal cations, while as the reaction continues, a complete collapse of the structure is achieved. The etching effect is stronger with higher  $HNO_3$  concentrations. As an example, a controlled etching of CoFe LDH is achieved as long as the  $HNO_3$  volume is below 3.0 mL, while by exceeding this value, a complete collapse of the structure occurs [83].

In general, the dissolution of the material starts from the borders of the platelets

and proceeds towards the internal region (fig.4.7) [84]. After the acid treatment, the space between particles of LDHs increases, while the plate thickness decreases, leading to a decline in their agglomeration. At the same time, hydrogen bond force between particles decreases as a consequence of the elimination of some hydroxyl groups from the surface of the material [85].

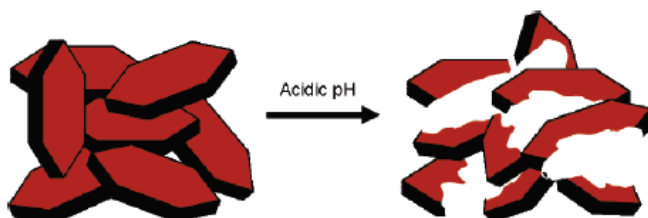


**Figure 4.7:** Schematic representation of the dissolution mechanism of LDHs occurring at low pH [84].

## 4.2 Characterization techniques

In order to achieve information about the composition and the structure of LDHs, both in the initial form of powders and in the final deposited film, as to better understand the gas sensing performance, several analytical techniques can be employed. A brief description of some of them, based on the trends present in literature, is provided.

### 4.2.1 Scanning Electron Microscopy and Transmission Electron Microscopy

Scanning Electron Microscopy (SEM) and Transmission Electron Microscopy (TEM) are two characterization techniques employed to provide information on the morphologies and structures of the materials, which employ a high energy electron beam as a source to induce the formation of an image. As the e-beam is focused on the surface of the sample, the interaction between incoming electrons and the specimen induces the formation of different signals according to the nature of the interaction, which can either be elastic, when the incident electrons scatter with the atomic nuclei of the sample or with the outer shell electrons having similar energy but still maintain their initial energy, or inelastic, when several scattering events occur, resulting in the primary beam electrons transferring part of their energy to the atoms of the sample [86].

SEM allows to achieve a compositional and topographical analysis together with a

morphological one, according to the type of signal collected, either coming from backscattered electrons (BSE), which undergo different elastic scattering events to finally escape from the surface with an energy greater than 50 eV, or secondary electrons (SE), loosely bound electrons emitted from ionized atoms as a consequence of inelastic scattering, managing to escape to vacuum with low energies (3-5 eV) [86].

TEM, involves a reconstruction of the diffraction pattern generated from scattering between incoming electrons and the sample crystal structure by means of a set of lenses and apertures. Different types of images can be obtained employing TEM analysis, according to the features that one wants to analyse: in bright field, contrast is enhanced by selecting only the unscattered electron beam through an aperture, so that the resulting image is characterized by dark features corresponding to areas of scattered and absorbed electrons, and bright ones which transmit electrons; in dark field, the imaging of crystal defects is enhanced by collecting only scattered electrons, so that areas where electron transmission occurs appear black, while the others are brighter; diffraction images are a result of scattering as the beam passes through the sample and provide information on whether the material structure is crystalline and ordered, imaging a regular array of dots, or amorphous, imaging diffuse ring diffraction patterns [87].

Examples of applications of these techniques found in literature to study LDHs show that SEM is employed to investigate the morphology of the samples, with a focus on whether they manage to successfully aggregate in 3D hierarchical flower-like structures, while TEM provides further details on the constituent nanopetals and on their characteristic porosity (fig.4.8).

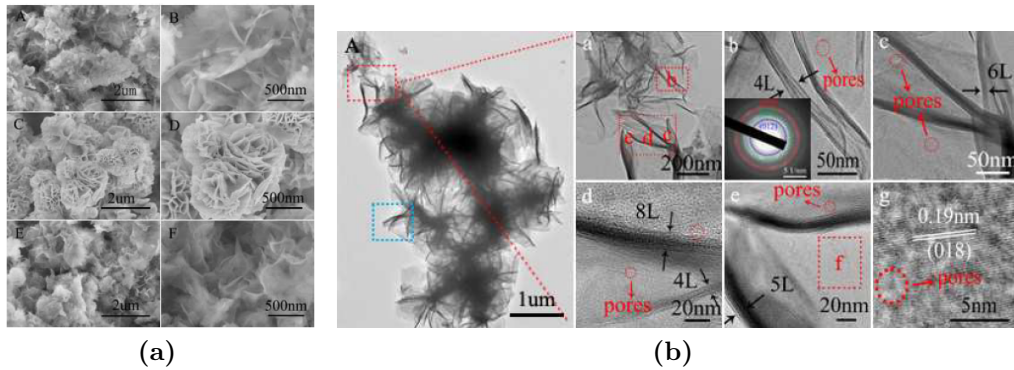


**Figure 4.8:** SEM (a) and TEM (b) images of NiFeAl LDHs. The first shows the morphology of the material with varying  $M^{2+}/M^{3+}$  contents. The second shows the structure of nanopetals at different magnifications [65].

## 4.2.2 X-Ray Powder Diffraction and Fourier Transform Infrared Spectroscopy

XRD and FTIR are employed to investigate the crystal phase of as-prepared samples. XRD is generally used to get structural information of the bulk of the material, since it allows to identify the crystallinity fraction and the size of crystal grains together with their orientation. The analysis working principle is based on the study of the diffraction of incident X-rays by the crystallographic planes of the specimen. The resulting pattern shows the intensity of the detected X-ray radiation as a function of the deflection angle. A peak is present whenever a specific requirement is met, named Bragg's law, which identifies the condition to have constructive interference for the radiation [88]. Several databases exist which collect the angular positions and intensity of diffraction peaks for different materials, so that information about the sample under test is achieved by comparing the XRD spectrum with the known ones. Figure 4.9 shows some examples of XRD patterns for LDHs.

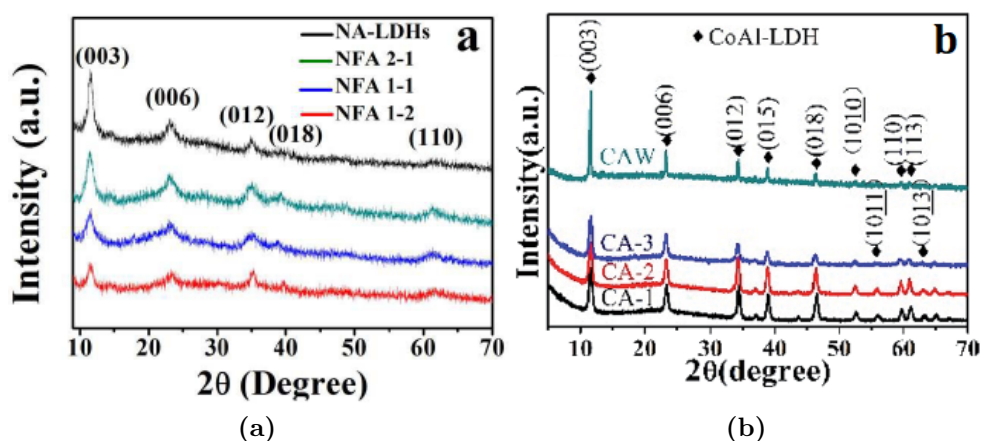


**Figure 4.9:** XRD patterns of (a) NiAl and NiFeAl LDH [65] and (b) CoAl LDH [56].

FTIR spectra provide information on the chemical composition of the samples. The source for the analysis is represented by an IR radiation, which passes through the specimen getting partially absorbed and partially transmitted. The measured signal provides a spectrum which represents the molecular composition of the sample. The resulting pattern shows transmittance as a function of the radiation wavenumber. It is characterized by four regions, which indicate different types of bonds: single bonds (i.e. O-H, C-H, N-H) are detectable at higher wavenumber, while triple and double bonds at middle wavenumber values. In the low wavenumber region, a

complex pattern of vibration is visible, which is characteristic of the molecule as a whole, so it is employed for its identification [89]. In the case of LDHs, spectra are characterized by a broad absorption peak at high wavenumber, corresponding to stretching vibrations of surface hydroxyl groups and of interlayer water molecules, followed by stretching modes for the specific interlayer anions in the intermediate region, and by bending vibrations of metal-oxygen bonds in the low wavenumber one (fig. 4.10).

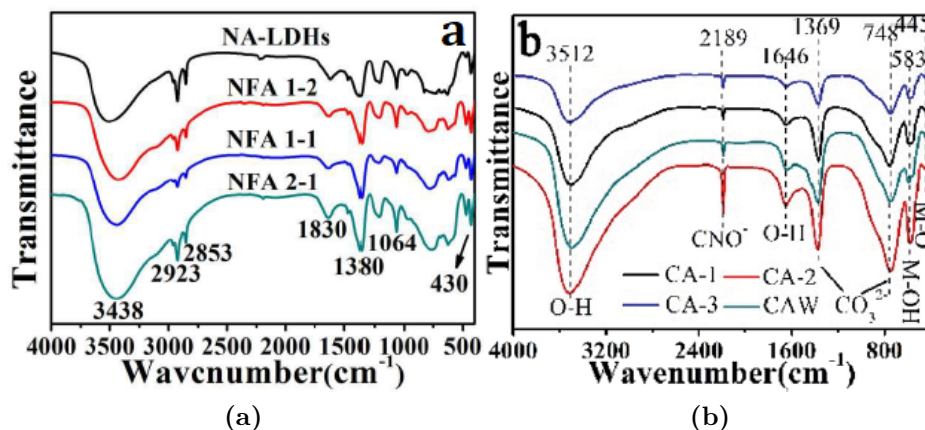


**Figure 4.10:** FTIR spectra of (a) NiAl and NiFeAl LDH [65] and (b) CoAl LDH [56].

### 4.2.3 X-ray Photoelectron Spectroscopy

XPS is a technique employed to compute the elemental surface analysis of materials. The basic working principle is the photoelectric effect, which consists in the emission of photoelectrons by atoms which were previously excited through the absorption of photons. The excitation source is therefore represented by photons, but electrons are collected and their energy spectrum is analysed. The XPS spectrum shows the intensity of the detected electron signal as a function of the binding energy of electrons. The resulting peaks are characteristic of elements, so a clear identification of components is possible, together with their chemical surrounding [90]. As for XRD, a reference database of known elements is provided.

XPS analysis of LDHs involves the evaluation of the spectra of the main chemical components of the structure, namely the two metal cations, the oxygen species and the interlayer anions. The spectra of the metal cations show peaks characteristic of the specific constituents, accompanied by eventual shifts which indicate the effective incorporation of neighbouring species (fig. 4.11 a-c). As regarding oxygen spectra, they are generally composed of three peaks, the first ( $BE \sim 528.3 -$

530.1 eV) corresponding to the lattice oxygen, the second ( $BE \sim 531.5 - 532.9$  eV) corresponding to oxygen vacancies structure, and the third ( $BE \sim 533.5 - 534.9$  eV) corresponding to chemisorbed oxygen (fig. 4.11 d-f) [59].

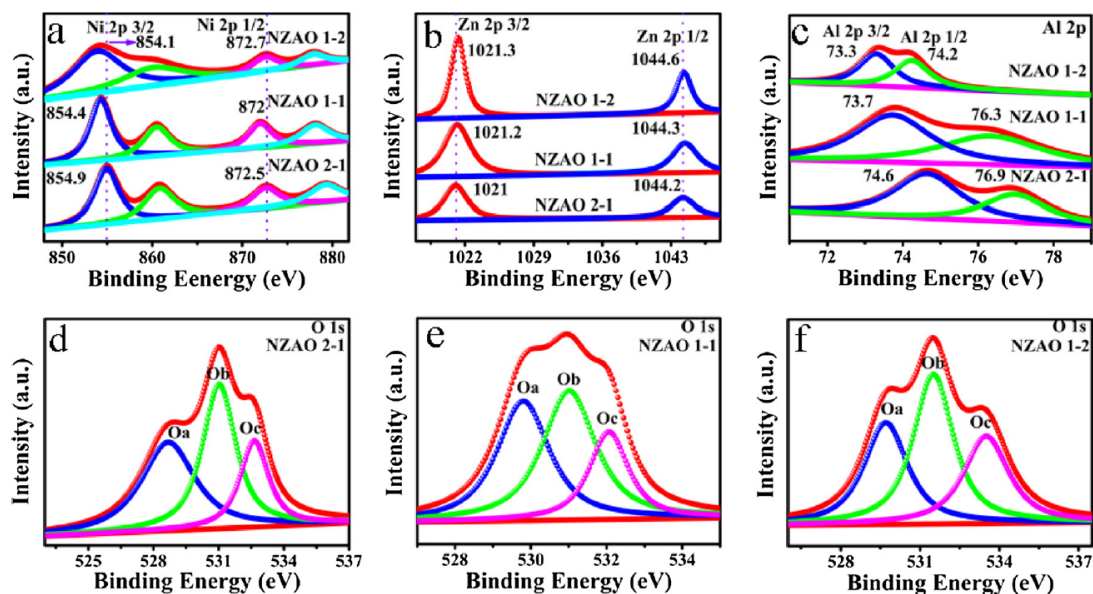


**Figure 4.11:** XPS spectra of NiZnAl LDH corresponding to (a) Ni 2p, (b) Zn 2p, (c) Al 2p and O1 s (d-f) [59].

### 4.3 Design and optimization of the sensor

The choice of implementing a sensor consisting of IDEs relies on their ability to provide a careful control over both sensing and electrical properties through the optimization of the sensing area, identified as the area in the gap between any two subsequent fingers of the array. It is an important feature to optimize since it is strictly related to the response and sensitivity of the sensor; in fact, even though the sensing material is generally deposited over the entire surface of the IDEs, the only portion which actually reacts with the analyte is the one lying in the sensing area. Current flows from one IDE's finger to another placed across the gap, and essentially no current is measured on the part of the sensing layer deposited on top of the electrodes [91].

In this type of configuration, the IDE array can be modeled as a chain of individual resistors arranged in parallel. The overall resistance of the structure should include

three main terms [92]

$$R_{Tot} = R_{Sensing} + R_{Electrode} + 2R_{Contact} \quad (4.2)$$

where  $R_{Sensing}$  is the resistance of the sensing layer,  $R_{Electrode}$  is the resistance of the electrodes and  $R_{Contact}$  is the contact resistance between the sensing layer and the electrodes. In general,  $R_{Electrode}$  is small compared to the other two terms, so it can be safely neglected, while the contact resistance acquires a dominant role only when dealing with extremely dense thin films. As a consequence, in the present case, the total resistance can be simply approximated as [92]

$$R_{Tot} \approx \rho \cdot \frac{G}{N \cdot L \cdot t} \quad (4.3)$$

where  $\rho$  is the resistivity of the sensing material,  $G$  is the width of the gap between any two IDEs,  $N$  represents the number of fingers in the array,  $L$  is the length of the sensing area, and  $t$  is the thickness of the fingers (fig.4.12).

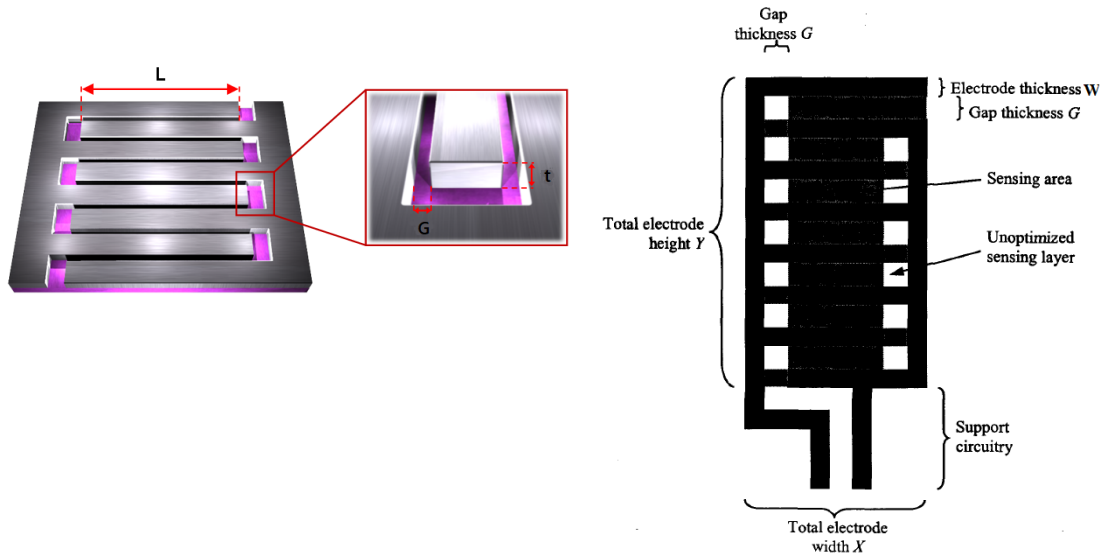


**Figure 4.12:** Schematic representation of IDEs with all their relevant parameters [92], [91].

In addition, it is important to mention that not the whole sensing area contributes in the same way to the reaction with the analyte. This happens because the width of the gap between fingers is not constant overall the structure, in particular it is fixed to a predefined value for any two parallel portions of the fingers, but increases at their corners, arriving to a maximum of 1.4142 times greater values. This increase may cause the material deposited in these corner areas to be inactive

in response to the analyte. This happens because, according to equation 4.3, the resistance of the sensing layer is directly proportional to the width of the gap between IDEs, therefore the regions around the corners appear to be more resistive compared to those along the parallel sides, so that the current will prefer flowing across the gaps where the resistance of the structure is minimal, allowing only a negligible amount to flow along the path between the corners [91].

Starting from these observations, it is useful to evaluate the portion of the IDEs which actually participate to the sensing operation in order to properly design a sensor. To this aim two parameters can be introduced:

- *Efficiency of the sensor*, defined as [91]

$$\varepsilon = \frac{A_{Sensing}}{A_{Tot}} \quad (4.4)$$

where  $A_{Sensing}$  is the effective sensing area and  $A_{Tot}$  is the total area of the device. Considering the model of the generic IDEs shown in figure 4.12, equation 4.4 can be re-written as

$$\varepsilon = \frac{\frac{GY}{G+W}(X - 2G - W) + G^2 + GW}{XY} \quad (4.5)$$

where  $X$  and  $Y$  represent the width and height of the device respectively, and  $W$  is the width of each finger.

Theoretically it should be a number comprised between 0 and 1, but in reality it reaches a maximum practical limit corresponding to [91]

$$\varepsilon_{max} = \frac{G}{G + W} \quad (4.6)$$

Because of the presence of these two limits,  $\varepsilon$  becomes a parameter to measure a relative efficiency, but it does not provide an absolute result for the optimization of the sensor.

- *Optimization of the sensor*, it is introduced to overcome the limitations of the efficiency parameter, and it is defined as [91]

$$\Theta = \frac{\varepsilon}{\varepsilon_{max}} \quad (4.7)$$

Like  $\varepsilon$ ,  $\Theta$  is a number between 0 and 1, reflecting how well the sensor is optimized, but it is not limited by any practical limit, providing an absolute result.

When designing a device, one should aim at maximizing both parameters, but when this is not possible, a design characterized by a good efficiency but a poor optimization should be preferred since leading to a better performance. The design implemented for this specific work is therefore obtained starting from the previous considerations. The proposed structure consists of a  $11\text{ mm} \times 8\text{ mm}$  substrate on top of which an array of IDEs composed by 100 fingers, characterized by a pitch of  $45.2\ \mu\text{m}$  ( $W = G = 22.6\ \mu\text{m}$ ) is realized. The thickness of the electrodes should be chosen considering the specific resistivity of the sensing layer, which varies according to the LDHs composition, between  $10^2\ \text{ohm} \cdot \text{m}$  and  $10^4\ \text{ohm} \cdot \text{m}$ , so it can be set to  $100\ \text{nm}$  since leading to correctly measurable resistance values. Several options were evaluated before proceeding to the choice of a specific design, which are here briefly discussed:

- 1) *Option 1.* A squared layout in which X and Y have the same extension is realized, considering three different options for W and G: 1)  $W = G$ , 2)  $W = 3/2 \cdot G$  as suggested in [93], and 3)  $W = 2 \cdot G$ . Three possible values are considered for X and Y, namely  $4.5\ \text{mm}$ ,  $6\ \text{mm}$  and  $9.5\ \text{mm}$ , all leading to equivalent results in terms of efficiency and optimization parameters. Both  $\varepsilon$  and  $\Theta$  were evaluated considering the mentioned cases, as function of a variable number of fingers. Results are shown in figure 4.13.

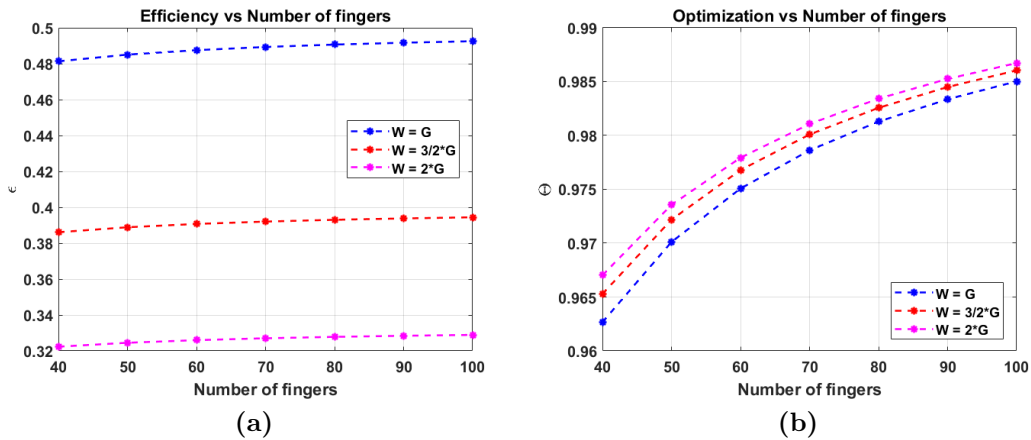


**Figure 4.13:** Efficiency (a) and optimization (b) parameters for a squared layout.

In this case, the maximum efficiency values correspond to 0.5, 0.4 and 0.33 for the three different cases. Even though the best optimization is achieved when  $W = 2 \cdot G$ , the highest efficiency corresponds to the case  $W = G$ , making it the preferred choice for this layout. In all the cases, the variation of the number of fingers leads to no large improvements in the efficiency, while a high

N corresponds to the best optimization value. Unfortunately the efficiency value is low, so efforts can be made to improve it. A schematic representation of this layout is shown in figure 4.16a.

- 2) *Option 2.* Starting from the observations of the previous point, some modifications are performed with the attempt of improving the efficiency of the device. It is decided to fix the height of the device, considering the number of fingers equal to 100, and let the horizontal dimension X vary. As before three different values for Y and three different options for W and G are considered. Results are shown in figure 4.14. Only the case corresponding to equal electrodes width and sensing gap is reported, since as before, the other two options lead to lower efficiency values.

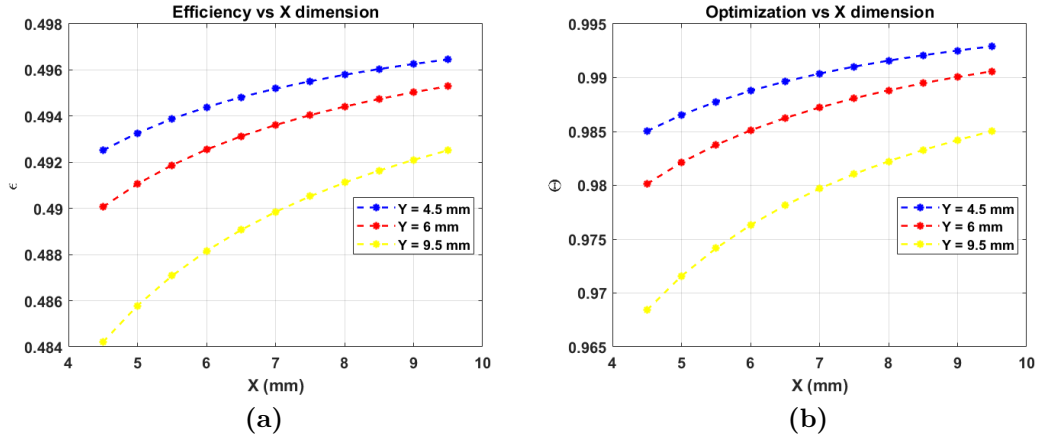


**Figure 4.14:** Efficiency (a) and optimization (b) parameters as function of the horizontal dimension variation when  $W = G$ .

As it is possible to observe from figure 4.14, when enlarging the device along the horizontal dimension X, higher  $\varepsilon$  and  $\Theta$  values are achieved. In particular, the highest values occur for the lowest aspect ratio ( $Y/X = 0.47$ ).

This design, still characterized by a low efficiency, leads to an improvement if compared to the previous option.

- 3) *Option 3.* For this solution the same procedure as in the previous point is applied, but now considering a variation of the height of the device and keeping the width to a fixed value (fig.4.16b). Results are shown in figure 4.15.

As it is possible to notice, both the efficiency and optimization parameters remain constant as the height of the electrodes increases, with minimum variations  $\Delta\varepsilon = 2 \cdot 10^{-5}$  and  $\Delta\Theta = 4 \cdot 10^{-5}$ , and as expected, the highest aspect ratio structures are associated to the worst behaviours.

These results can be explained by observing that when increasing the Y dimension, both the sensing area and the total sensor area increase at the same rate, so their ratio ( $\varepsilon$ ) remains basically unchanged [91].

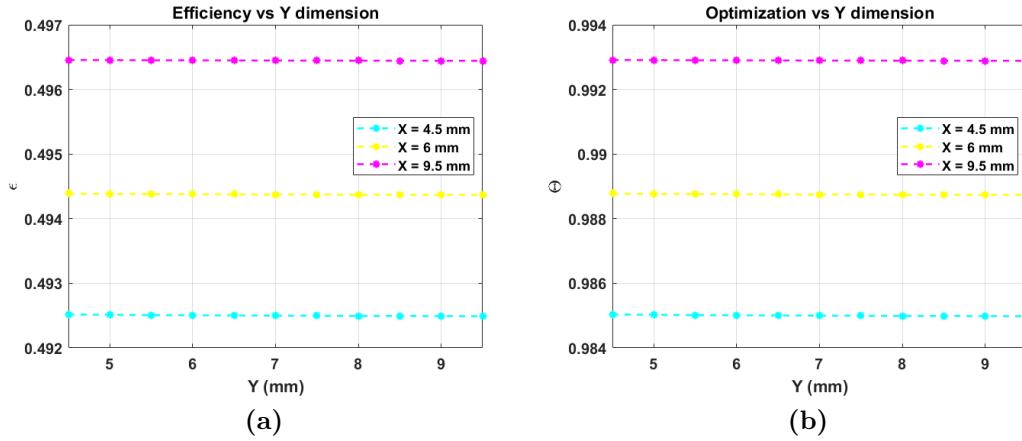


**Figure 4.15:** Efficiency (a) and optimization (b) parameters as function of the vertical dimension variation when  $W = G$  and  $N = 100$ .

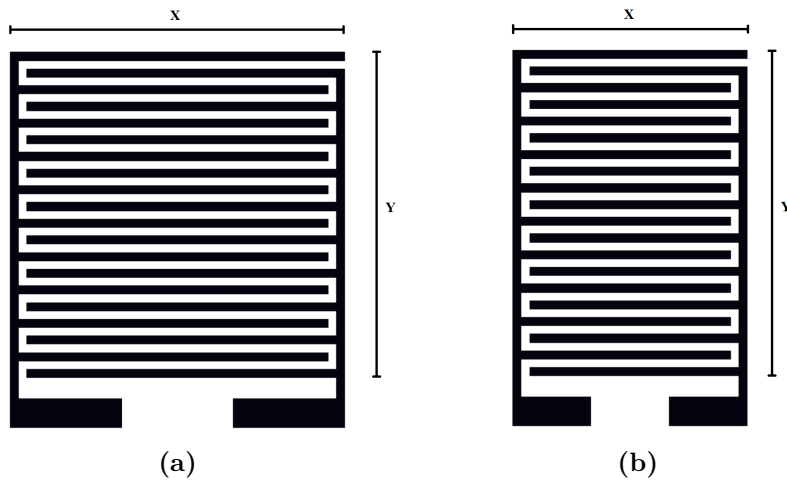


**Figure 4.16:** Representation of an IDE characterized by (a) squared layout, (b) layout in which the vertical dimension is enhanced with respect to the horizontal one. In both cases the width of the gap corresponds to that of the electrodes.

Based on these remarks, the design associated to the best expected performance for the device aims at maximizing the width of the IDEs compared to the height

but still keeping the number of fingers fixed to a large enough value (fig.4.17). Therefore, as mentioned at the beginning of the section, the developed device is characterized by (table 4.1)

Substrate's width (mm)	11
Substrate's height (mm)	8
Contact pads' width (mm)	3.5
Contact pads' height (mm)	1.3
X(mm)	9.5
Y (mm)	4.5
G ( $\mu\text{m}$ )	22.6
W ( $\mu\text{m}$ )	22.6
t (nm)	100
N	100

**Table 4.1:** Geometrical parameters of the designed sensor.

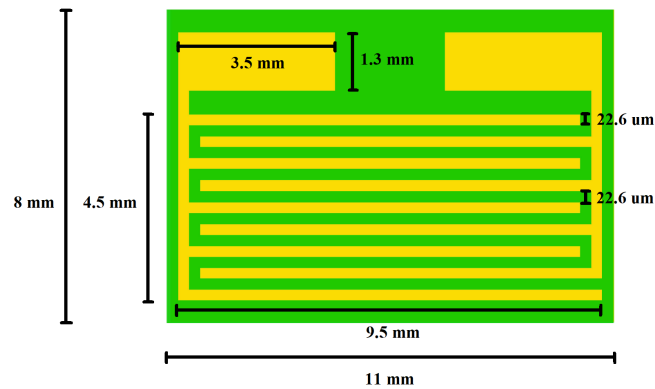


**Figure 4.17:** Representation of the IDE (Option 2) with its dimensions.

### 4.3.1 Improved design of IDE sensor

As it is evidenced in the previous section, even though the design of the proposed generic IDE structure shows good optimization values, the efficiency is poor, and it just slightly improved when considering the final chosen layout. This section therefore focuses on the analysis of possible alternative designs, with the aim of achieving higher efficiency and optimization values.

#### 1) Introduction of round concave corners to the standard IDE design.

The efficiency of a standard IDE sensor depends on the size of the sensing area, which, as mentioned in the previous section, is limited because of the non constant G distance. A simple solution to this problem is represented by the use of round concave corners in the IDEs (fig.4.18). In this way, G is constant throughout the structure, and the current can flow equally at all points.

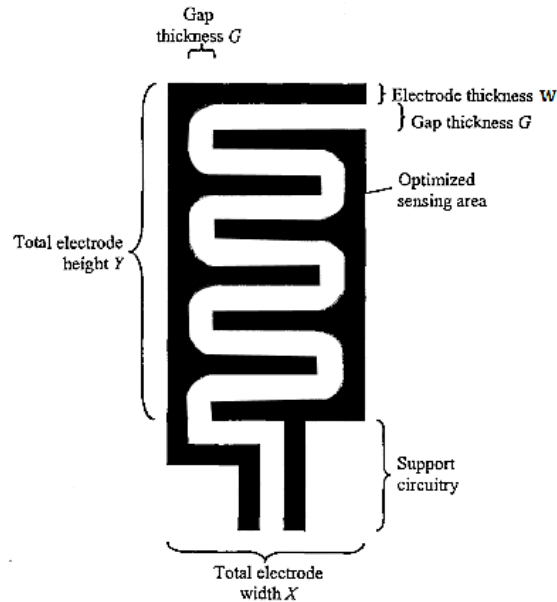


**Figure 4.18:** Schematic representation of IDEs having rounded corners [91]

The expression for the efficiency of the sensor becomes [91]

$$\varepsilon = \frac{\frac{GY}{G+W}(X - (2 - \frac{\pi}{2})G - W) + G^2 + GW}{XY} \quad (4.8)$$

According to equation 4.8, an increase in the efficiency of the sensor is expected because the multiplicative term for G, which gets subtracted from X has become approximately equal to 0.5, smaller than the case of 90° corners fingers.

Figures 4.19, 4.20 and 4.21 show the three cases corresponding to a square design with different options for  $W$  and  $G$ , and a rectangle design with varying  $X$  and  $Y$  dimensions, characterized by  $W = G$ . Good improvements in both  $\varepsilon$  and  $\theta$  values are achieved for all the three options, with increases in efficiency corresponding to  $40 \times 10^{-4}$ ,  $18 \times 10^{-4}$  and  $19 \times 10^{-4}$  respectively (fig.4.22). As expected, the best design still corresponds to the case of the rectangular layout with a low aspect ratio.

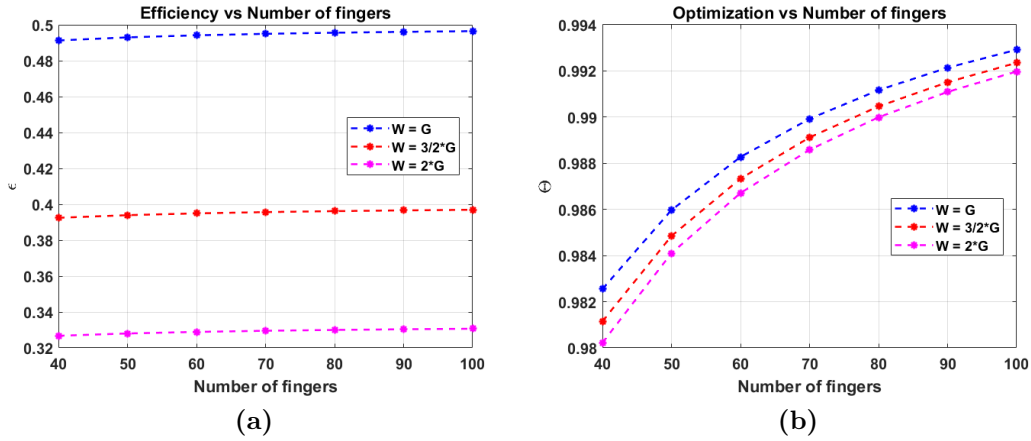


**Figure 4.19:** Efficiency (a) and optimization (b) parameters for a squared layout with rounded concave corners.

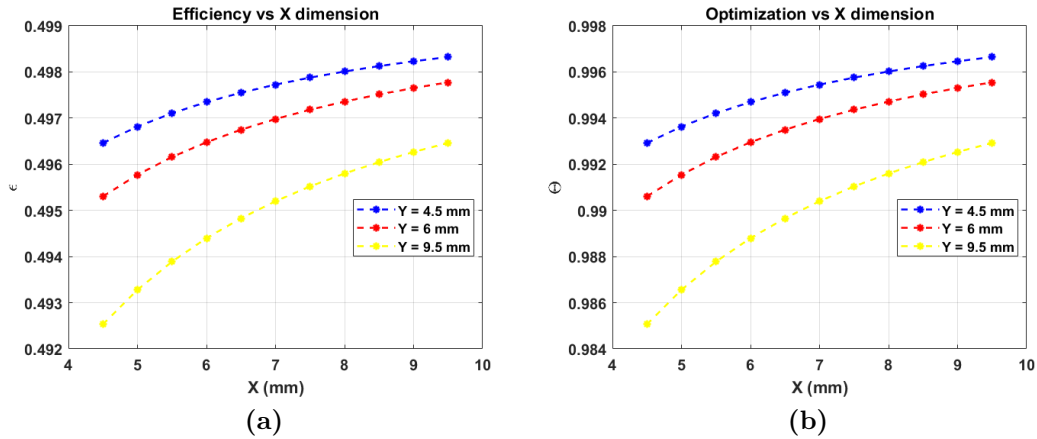


**Figure 4.20:** Efficiency (a) and optimization (b) parameters as function of the horizontal dimension variation when  $W = G$  for a layout with rounded concave corners.

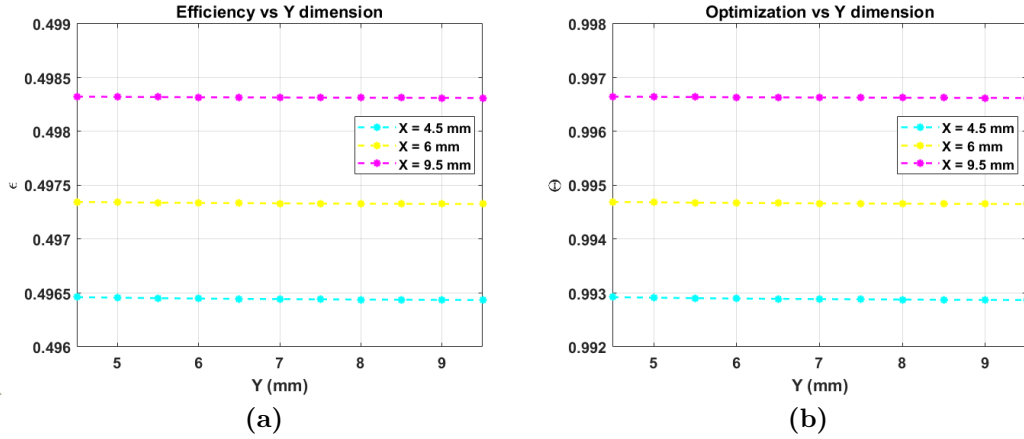


**Figure 4.21:** Efficiency (a) and optimization (b) parameters as function of the vertical dimension variation when  $W = G$  and  $N = 100$  for a layout with rounded concave corners.

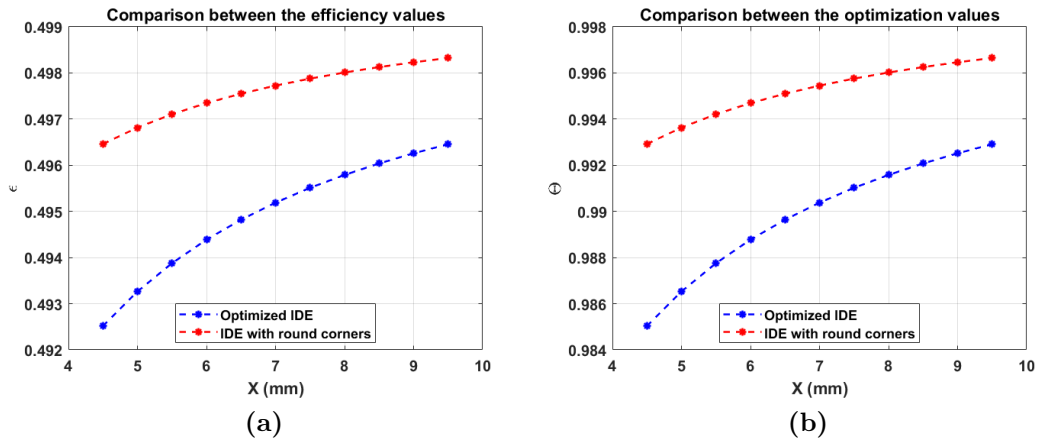


**Figure 4.22:** Comparison of the efficiency (a) and optimization (b) parameters as function of the horizontal dimension variation when  $W = G$  and  $N = 100$  between the optimized IDE and the layout with rounded concave corners.

## 2) Spiral layout with 90° corners.

An interesting alternative to the classical IDE structure may be represented by a layout characterized by two identical electrodes shaped as to form a squared spiral (fig.4.23).

In the proposed design, the width of the electrodes and the dimension of

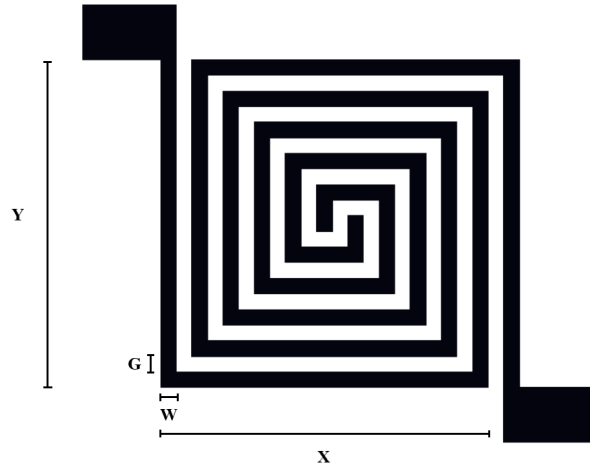


**Figure 4.23:** Schematic representation of an electrode with a spiral layout.

the gap are chosen to be equal and they are set to the value selected for the optimized IDE design (see table 4.1), that is  $22.6 \mu\text{m}$ . As regarding the other dimensions, the choice is performed in order to enhance the efficiency and optimization of the sensor, still defined as in equations 4.4 and 4.7. Also in this case, the sensing area corresponds to the gap area with the exclusion of the regions around the concave corners of the electrodes. From figure 4.23 it is possible to notice that at each turn, both the horizontal and vertical sizes of each electrode decrease by a certain amount, in this specific case corresponding to increasing multiples of the sum between  $W$  and  $G$ . For this reason, to clarify the notation, the width and height of the first turn of the electrodes are labeled as  $X$  and  $Y$ . In this case, only a squared geometry is considered, since a rectangular one does not allow to keep constant both  $W$  and  $G$ . In fact, by keeping  $W$  fixed, at the center of the structure, a gap corresponding at least to the double of the desired one is obtained, because of differences in the vertical and horizontal dimensions, letting the central region be excluded from the sensing area for the reasons explained in Section 4.3. Conversely, by fixing the gap, the width of the electrodes should scale in one dimension to preserve the characteristics of the structure.

Figures 4.24 and 4.25 show the variations of  $\varepsilon$  and  $\Theta$  as function of the number of fingers, in this case corresponding to the number of turns of the electrodes, and of the initial dimension  $X$  (or  $Y$  since they coincide). As expected, both  $\varepsilon$  and  $\Theta$  increase with higher number of fingers, and consequently with the dimension of the device. In particular, the optimization of the sensor reaches a satisfactory value, being close to unity, while the efficiency is still limited.

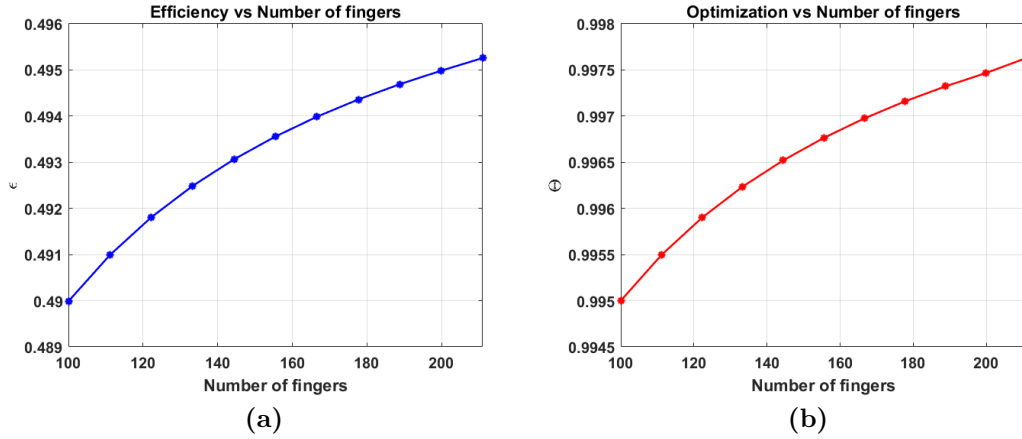


**Figure 4.24:** Efficiency (a) and optimization (b) parameters with varying number of fingers when W and G are fixed to  $22.6 \mu m$ .

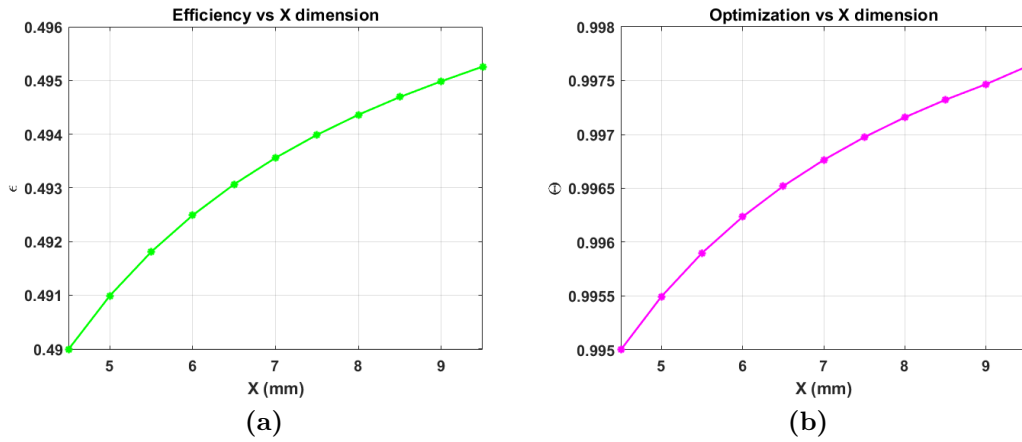


**Figure 4.25:** Efficiency (a) and optimization (b) parameters with increasing horizontal dimension X when W and G are fixed to  $22.6 \mu m$ .

The current layout is compared to the optimized IDE and to the squared IDE designs to analyze the differences between the performances of the three structures (fig.4.26). Even though the efficiency values for the optimized IDE and the spiral layout are similar, the performance is still better in the first case, while the squared IDE design shows a poor behaviour. The situation is reversed when considering the optimization parameter, which shows a promising increase for the layout of fig.4.23, when compared to the others. Based on these remarks, the spiral design seems to be a valid alternative to the classical IDE.

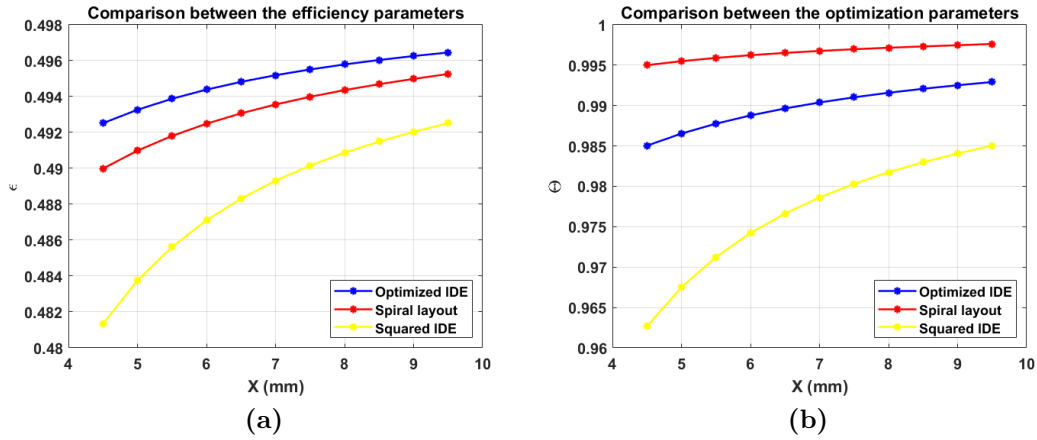


**Figure 4.26:** Efficiency (a) and optimization (b) parameters as function of the horizontal dimension X. For the optimized IDE,  $Y = 4.5$  mm, while for the other options  $X = Y$ . In all the three cases,  $W$  and  $G$  are fixed to  $22.6 \mu m$ .

A further aspect should be considered to complete the analysis. As mentioned at the beginning of Section 4.3, for a generic IDE design, the resistance of the electrodes can be safely neglected, since showing extremely low values compared to the other contributions. This consideration is not valid in the present case. The electrodes can now be modeled as a chain of individual resistors arranged in series. A comparison between the resistance values of the electrodes for the two different layouts is shown in fig.4.27.

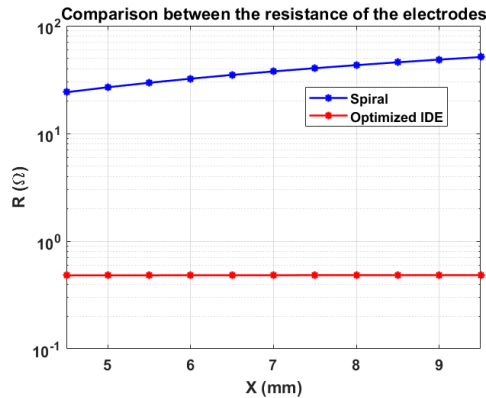


**Figure 4.27:** Comparison between the resistance of the electrodes for a spiral layout and an optimized IDE layout with increasing X dimension when the electrode thickness is set to 100 nm.

As expected, the resistance values for the IDE layout are lower than unity, while those of the spiral design are relevant, so they cannot be ignored. This represents a drawback for the layout, since a high  $R_{Electrode}$  may induce a non negligible noise which is not beneficial for the device operation.

3) **Spiral layout with round concave corners.**

In this case, as done for the IDE, the concave corners of the spiral layout are substituted by round ones, with the aim of increasing the sensing area. Figure 4.28 shows the results for the efficiency and optimization parameters as function of the dimension of the device.

As for IDEs, a relevant increase in both the efficiency and optimization parameters is observed, with  $\Theta$  approaching the value of 1, corresponding to an almost perfect optimization of the device.

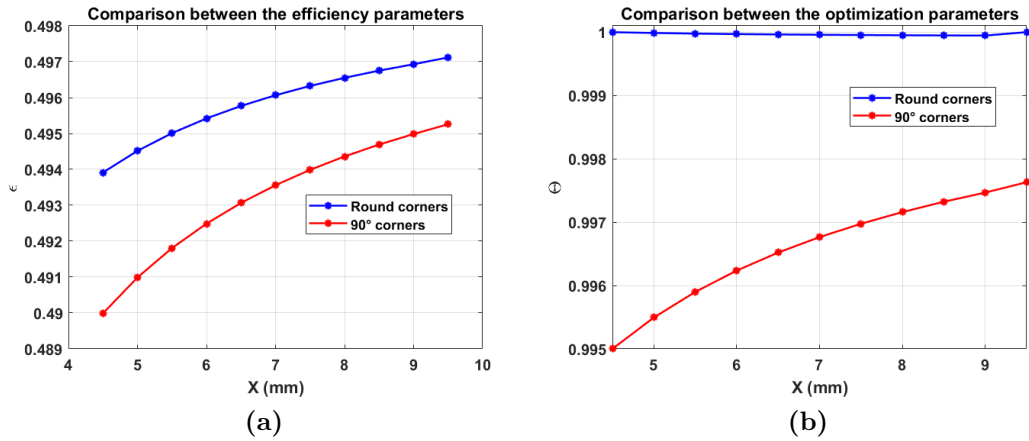


**Figure 4.28:** Comparison between the spiral layout with 90° corners and the layout with round corners of efficiency (a) and optimization (b) parameters as function of the horizontal dimension X.

## 4.4 Fabrication process

The fabrication of the device occurs through a standard photolithography process. The starting substrate is represented by a 4" diameter silicon wafer, provided with an insulating layer, as mentioned at the beginning of the chapter, so as to guarantee a proper insulation to the electrodes which will be deposited on its surface.

The description of the steps involved in the realization of the complete sensor can be divided in two sections, the first concerning the realization of the IDE structure, and the second involving the deposition of the sensing layer.

### 4.4.1 Electrodes fabrication

The schematic representation of the lithographic process is provided by figure 4.31. Before starting the process, the substrate needs to be cleaned with acetone and deionized (DI) water, and subsequently dried, to remove possible residual particles from its surface and improve adhesion of layers' materials. The realization of the electrodes occurs through a lift-off process, so as to guarantee a good resolution for the geometry of the device.

The first step consists in the deposition of a negative photoresist (PR) layer, specifically AZ nLOF 2070 from MicroChemicals, through spin-coating: a certain amount of PR is deposited at the center of the wafer, which is mounted on a vacuum chuck. The platform starts rotating initially at a slow spin rate, 600 rpm for 5 s, and then it ramps up to 3000 rpm for 60 s. The resulting PR layer is characterized by a thickness  $\sim 7 \mu\text{m}$ . A soft-bake process follows, to partially evaporate the remaining PR solvent, so improving adhesion and uniformity of the film and avoiding eventual contamination of the photo-mask. The process is carried on by heating the substrate through a hotplate for 7 minutes at 100 °C [94]. A rehydration is not necessary for this type of PR, so it is possible to directly proceed with the exposure step.

A UV mask containing a replica of the pattern for the realization of the electrodes is placed over the PR layer by employing a mask aligner system. The model for the mask (fig.4.29 and 4.30) is realized through Clewin5 software and allows to obtain 72 IDEs structures from a unique 4" wafer. The mask is realized through a direct laser writing process, which allows to directly transfer the pattern from the CAD design to the substrate. The writing step is performed through the LW405A Laser Writer from MICROTECH, provided with a GaN laser source (405 nm, 60 mW).

The PR is exposed to a UV light source (i-line, wavelength = 365 nm) for 16 s at 11 mW/cm<sup>2</sup>.

A post exposure bake (PEB) is necessary after the exposure to induce a cross-linking of the resist molecules, otherwise in the development step the exposed resist areas would be dissolved at a similar rate as the unexposed resist. It is performed

by heating the wafer over a hot plate for 60 s at 110°C [95]. The development of the PR is computed by employing the AZ MIF 726 developer solution from MicroChemicals. The wafer is immersed in a bath of the solution for 1 minute. Being a negative PR, the areas which were exposed to the UV radiation are less soluble in the developer solution since polymeric chains are more cross-linked, so they are preserved, while the unexposed ones are removed. A negative pattern of the mask is therefore now replicated on the PR. The wafer is then rinsed in DI water to remove residuals of the PR.

Two metallic layers can be now deposited over the PR in the following order by means of an e-beam evaporation process:

- 1) A Titanium (Ti) thin layer ( $\sim 10\text{ nm}$ ) working as adhesion layer;
- 2) Au for the electrodes ( $\sim 100\text{ nm}$ );

The unwanted PR, and consequently the Ti and Au portions deposited over it, are removed by placing the wafer in a bath of DMSO (Dimethyl Sulfoxide)-based stripper solution TechniStrip Micro D350 from MicroChemicals and by sonicating it for 15 minutes.

Images of the device at the end of the lift-off process are shown in the Appendix (fig. A.1).

Having obtained the desired pattern for the electrodes, the wafer can be finally cut to get single devices. The devices are then arranged so as to obtain arrays of two sensors (fig.4.32).

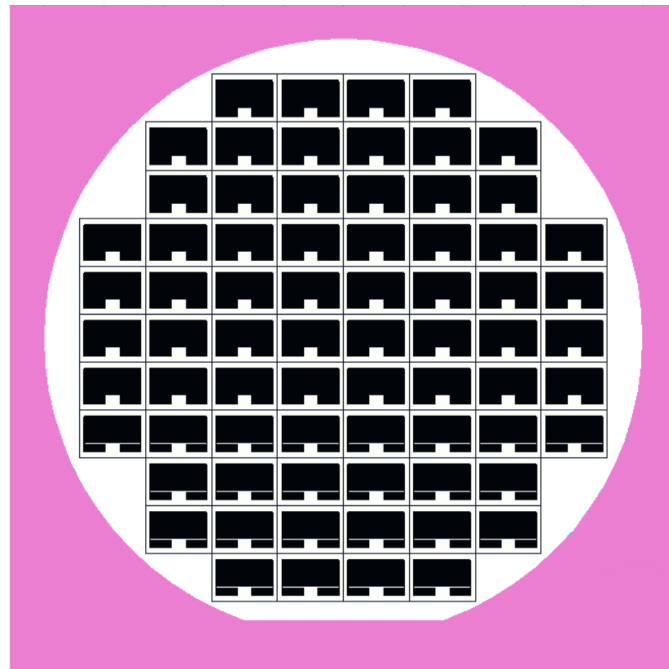


**Figure 4.29:** Virtual mask for the direct laser writing process obtained through CleWin5 software.

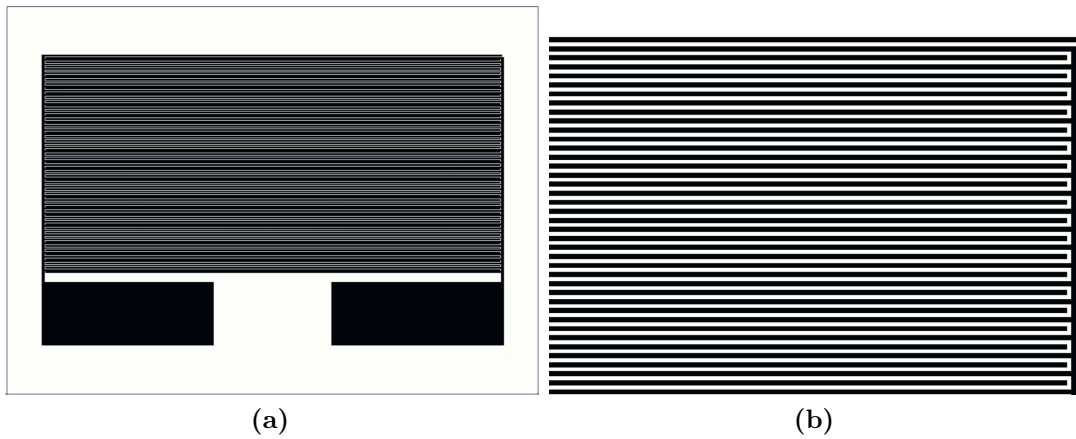


**Figure 4.30:** Details of the sensors' pattern on the mask: (a) whole device and (b) zoom on a portion of the IDEs

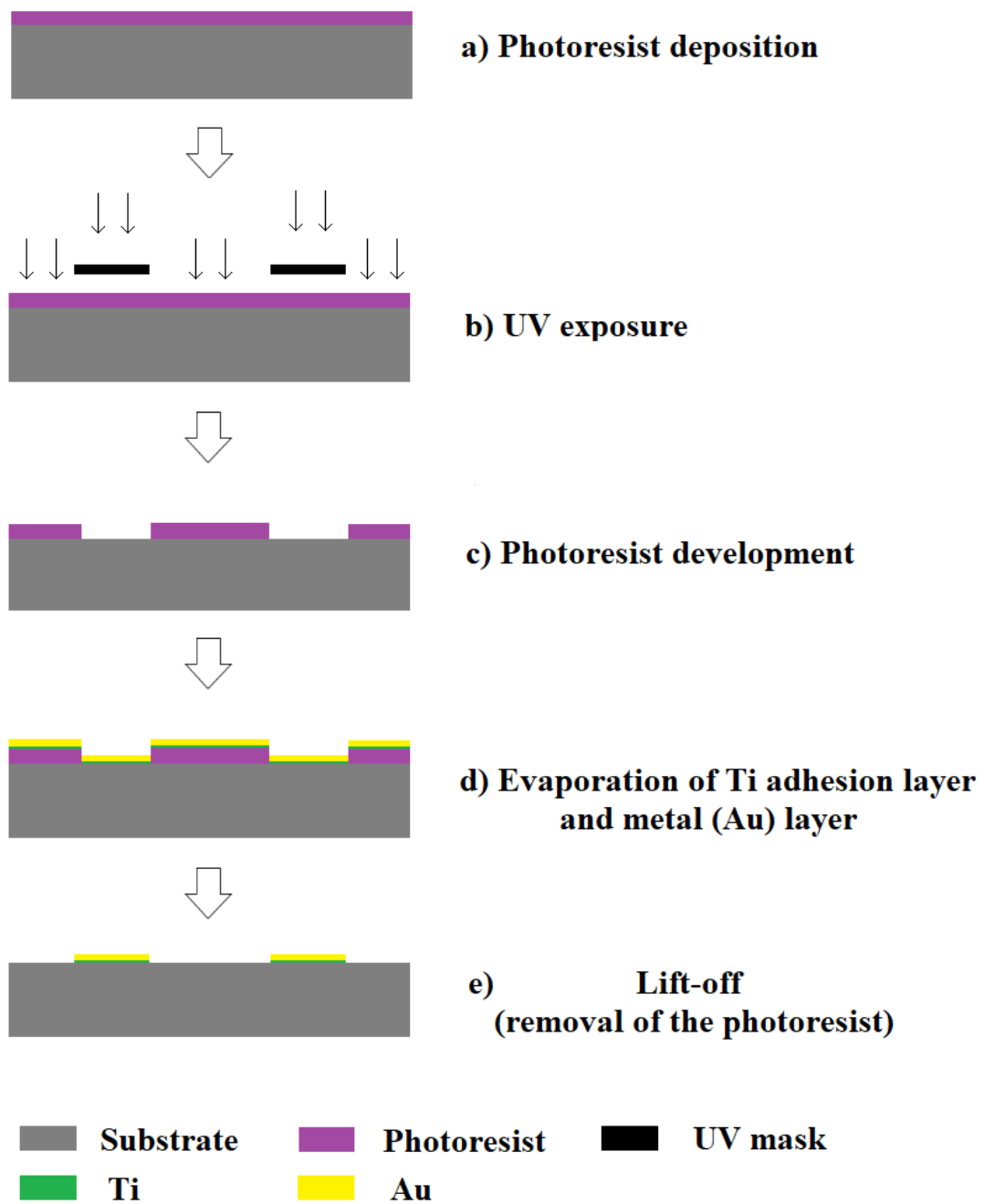


**Figure 4.31:** Schematic representation of the steps involved in the fabrication of the device.

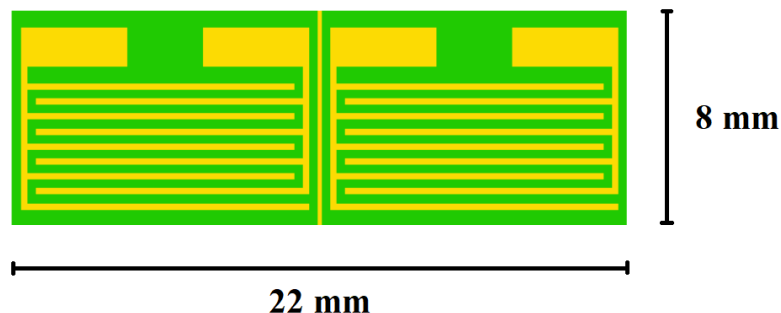


**Figure 4.32:** Schematic representation of the array composed by 2 sensors.

#### 4.4.2 Dispersion of LDH powders and drop-casting of the solution

Starting from the considerations expressed in section 4.1.1, several tests were performed to achieve a stable and homogeneous dispersion of each of the four LDH compositions.

Different solvents were considered, namely water, ethanol and acetonitrile. The former and the latter didn't lead to satisfying results since the powders were poorly dispersed and tended to deposit on the bottom of the vial. These problems were not encountered when using ethanol.

According to the specific LDH powder, different concentrations of solvent were employed (table 4.2).

LDH Powder		Solvent	
ZnAl-Cl	10 mg	Ethanol	0.8 mL
ZnFe-Cl	10 mg	Ethanol	0.7 mL
ZnAl-NO <sub>3</sub>	10 mg	Ethanol	0.9 mL
MgAl-NO <sub>3</sub>	10 mg	Ethanol	0.6 mL

**Table 4.2:** Summary of the dispersions of LDHs realized with ethanol.

A sonication step followed by employing an ultrasonic bath (59 kHz, 100% power) for two consecutive cycles of 10 and 5 minutes each.

This procedure allows to obtain homogeneous and stable dispersions able to maintain their characteristics for several weeks.

To proceed with the fabrication of the sensors, drop-casting was selected for the

deposition of the sensing layer since, as mentioned in section 4.1.2, it represents a simple and fast technique when dealing with substrates having reduced dimensions. A micro syringe was employed to drop 0.1 mL of each solution over the active area of the IDEs. To avoid the spreading of the solution over inactive areas, a PDMS mold was contacted to the device (fig.4.33). A short thermal treatment was performed by heating the samples at 65°C for 10 minutes over a hotplate to speed up the evaporation of the solvent in excess.

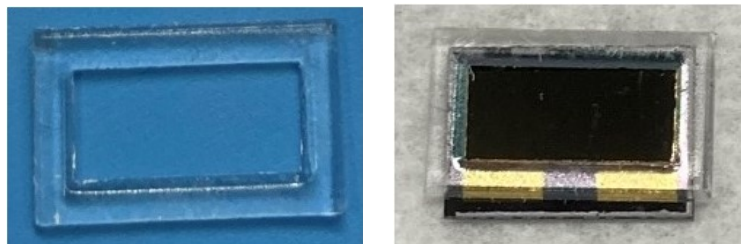


**Figure 4.33:** PDMS mold employed to selectively deposit the LDH solution over the active area of the device.

Images of the sensors obtained following the procedure just described are shown in the Appendix (fig.A.2).

#### 4.4.3 Structure characterizations

The morphology of the LDH structures after the deposition over the electrodes was investigated through a FESEM (Field Emission Scanning Electron Microscopy) analysis. Figure 4.34 shows the results.

It is possible to notice that in all the reported cases, the typical hierarchical flower-like morphology is not clearly visible, but the material tends to assemble in thick and irregular shaped nanoparticles and nanosheets so leading to an overall low porosity aggregation. This behaviour is a consequence of the  $M^{2+}/M^{3+}$  molar ratio, which in all the cases is too low to support the formation of thin and porous nanosheets and induces an extremely high density of layer charge.

A further comment can be provided regarding ZnAl-Cl and ZnAl-NO<sub>3</sub> LDHs. As it will be mentioned later on in this section, through the XPS analysis it was possible to extract the atomic percentage of the chemical species composing the materials. The Al amount for the two samples was found to be higher for ZnAl-NO<sub>3</sub>. This result can be correlated to the morphology of the material, since a larger  $M^{3+}$  content leads to smaller nanosheets aggregates. In general, the size is related to nucleation and growth rates, since as the former increases and the latter decreases the size of grains gets smaller and vice versa.

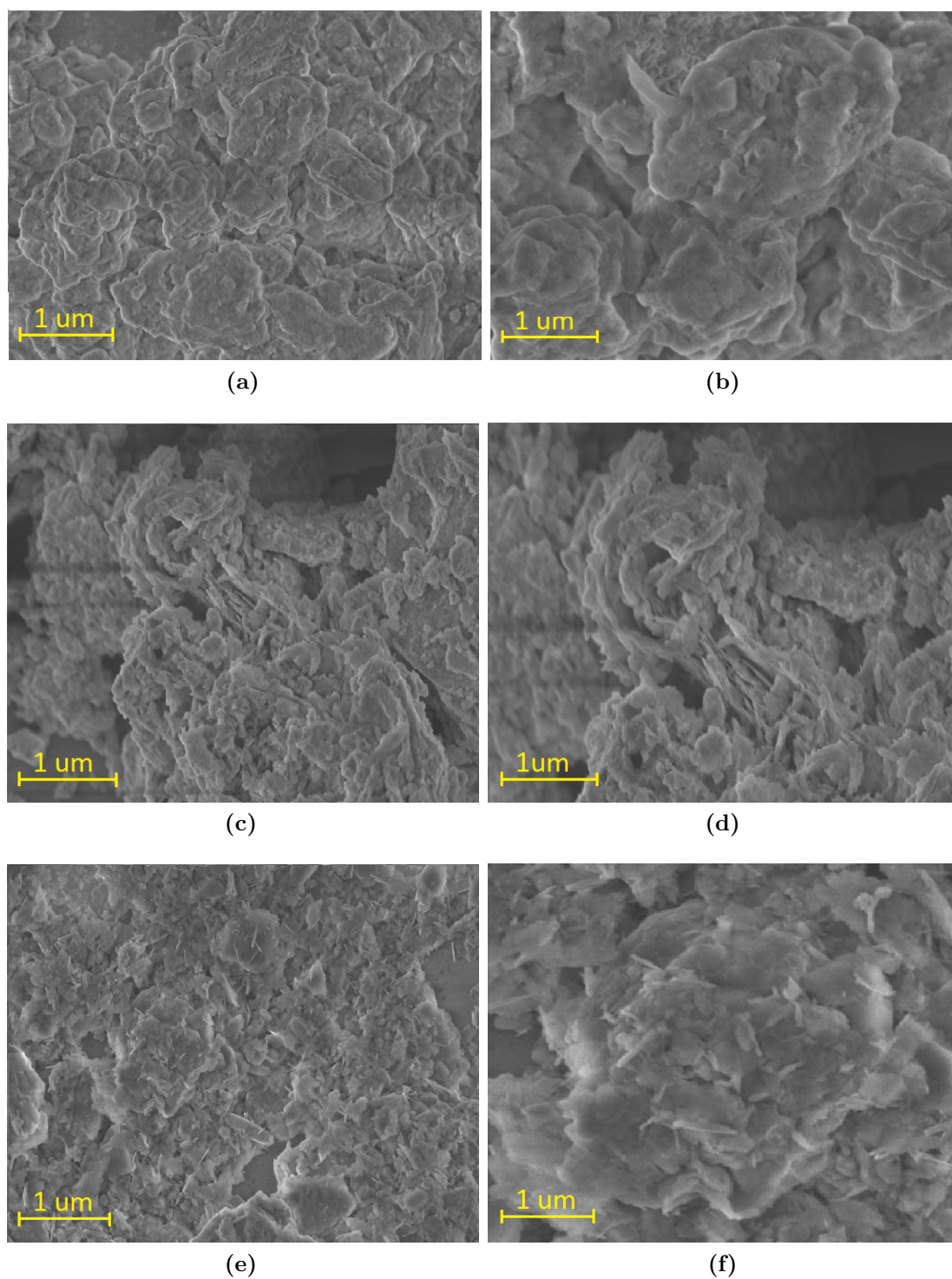


**Figure 4.34:** FESEM images of (a),(b) ZnAl-Cl LDH, (c),(d) ZnFe-Cl LDH and (e),(f) ZnAl-NO<sub>3</sub> LDH.

A high Al content leads to an increase in the number of available nucleation sites, therefore implying a high nucleation rate and smaller grain sizes [96]. These considerations are observable from fig.4.34(b) and fig.4.34(f). In all the reported cases the material still shows a high surface area to volume ratio, typical of layered categories. These results are in agreement with examples reported in literature. To investigate the molecular structure a FTIR analysis was performed in ATR (Attenuated Total Reflection) mode directly over the LDH powders. Figure 4.35 shows the detected spectra corresponding to the four different material compositions.

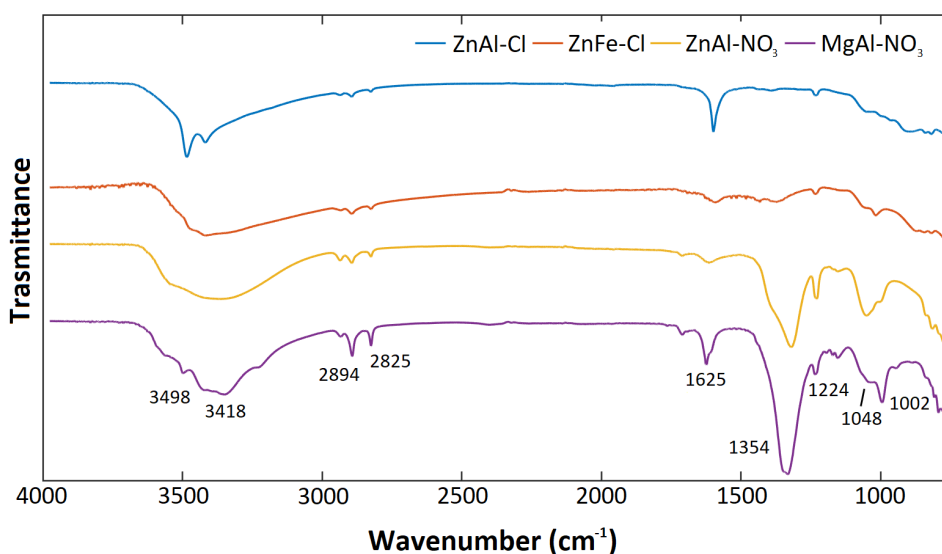


**Figure 4.35:** FTIR spectrum of the four LDH compositions.

As it is possible to notice all the curves present common features since sharing an overall analogous structure. In particular, the narrow absorption peak located at  $3498\text{ cm}^{-1}$  and the broad one at  $3418\text{ cm}^{-1}$  correspond to the stretching vibrations of the  $\text{-OH}$  groups in the brucite-like layers and of the hydrogen-bonded water molecules located in the interlayer space [36]. The absorption peaks at  $2894$  and  $2825\text{ cm}^{-1}$  are due to antisymmetric and symmetric stretching vibrations of  $\text{-CH}_2\text{-}$  from SDS employed for the synthesis of the material. The peak at  $1625\text{ cm}^{-1}$  is instead attributed to the bending mode of water molecules. Three final peaks are identified at  $1227$ ,  $1048$  and  $1002\text{ cm}^{-1}$  characteristic of the antisymmetric and symmetric stretching modes of  $\text{S=O}$  from SDS [37]. An additional peak can be observed in  $\text{ZnAl-NO}_3$  and  $\text{MgAl-NO}_3$  spectra corresponding to the vibration of the intercalated  $\text{NO}_3^-$  molecule [36]. Peaks in the range of  $800\text{-}400\text{ cm}^{-1}$  attributed to the vibrations of  $\text{M-O}$ ,  $\text{O-M-O}$  and  $\text{M-O-M}$  groups should complete the spectra, but they could not be detected because the resolution of the instrument employed

was limited to values around  $1000\text{ cm}^{-1}$ . Table 4.3 shows a summary of these considerations. All the identified peaks are in agreement with the considerations expressed in Section 4.2.2.

Wavenumber ( $\text{cm}^{-1}$ )	3498	3418	2894 2825	1625	1354	1227 1048 1002	800-400
Functional Group	-OH	OH-H <sub>2</sub> O	-CH <sub>2</sub>	H <sub>2</sub> O	NO <sub>3</sub> <sup>-1</sup>	SO <sub>4</sub> <sup>2-</sup>	M-O

**Table 4.3:** Data from the FTIR spectra.

The chemical composition of the samples was evaluated through XPS analysis (fig.4.36), in which the survey details were acquired by scanning the area at a pass energy of 187.85 eV, and EDX (Energy Dispersive X-ray) equipped in the FESEM system (fig.4.37).

In figure 4.36 all the main peaks for the different LDH compositions are highlighted. In all the samples it is possible to observe the O1s peak at BE  $\sim 530$  eV corresponding to the lattice atoms. As detailed in table 4.4, it represents the predominant atomic percentage. A second peak common to all the samples is located at BE  $\sim 289$  eV, and it corresponds to C1s, also referred to as adventitious carbon, which is nearly always present in XPS spectra since introduced on samples by the laboratory environment. Considering the main chemical constituents for the four samples, it is possible to notice that Zn 2p and Al 2p are correctly located at BE  $\sim 1022$  eV and BE  $\sim 75.9$  eV, corresponding respectively to Zn<sup>2+</sup> and Al<sup>3+</sup> oxidation states. The same considerations apply to Mg 2s and Fe 2p, showing peaks at BE  $\sim 89$  eV and BE  $\sim 707$  eV. As regarding the interlayer anions, Cl 2p and N 1s peaks can be observed at BE  $\sim 198$  eV and BE  $\sim 407$  eV. All these results are in perfect agreement with the trends reported in literature.

Table 4.4 summarizes the location of the main peaks for each element together with their atomic percentage. From these data it is therefore possible to estimate the atomic ratio  $M^{2+}/M^{3+}$  for the four compositions.

These results confirm the considerations mentioned regarding the morphology of the samples: the petal size gets smaller when increasing the amount of Al.

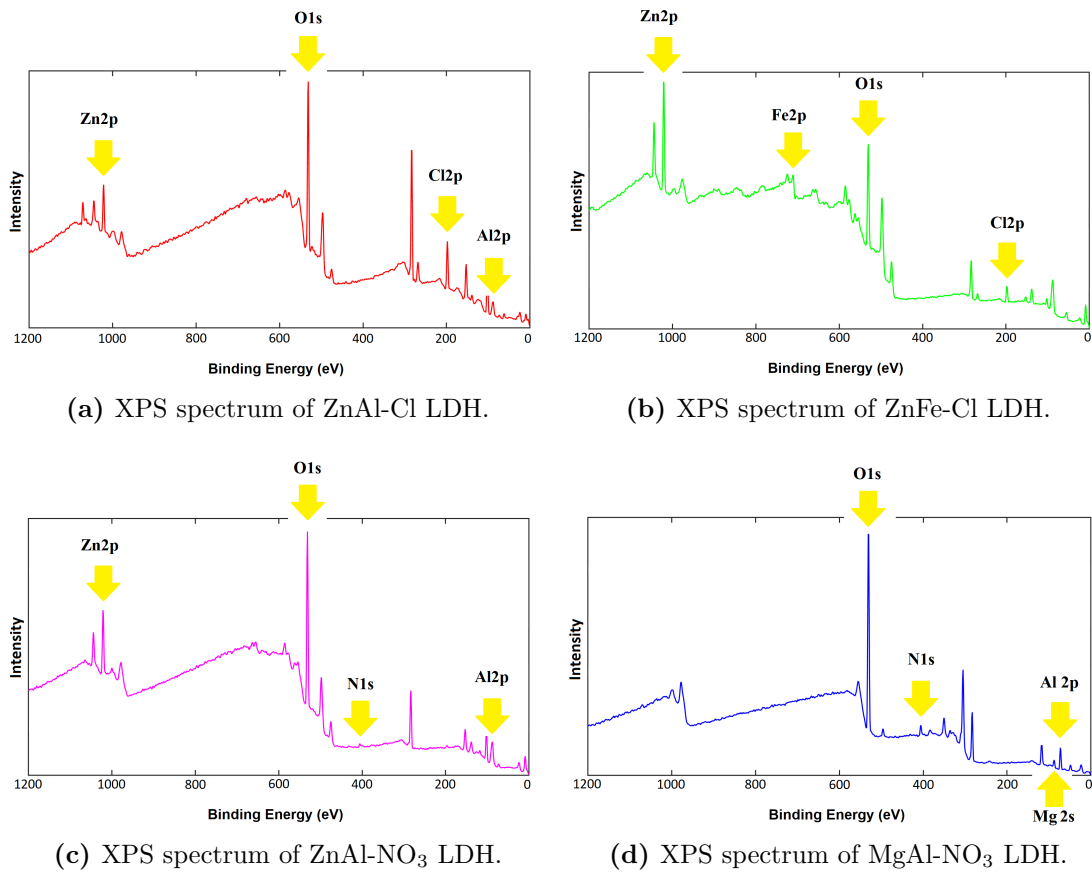
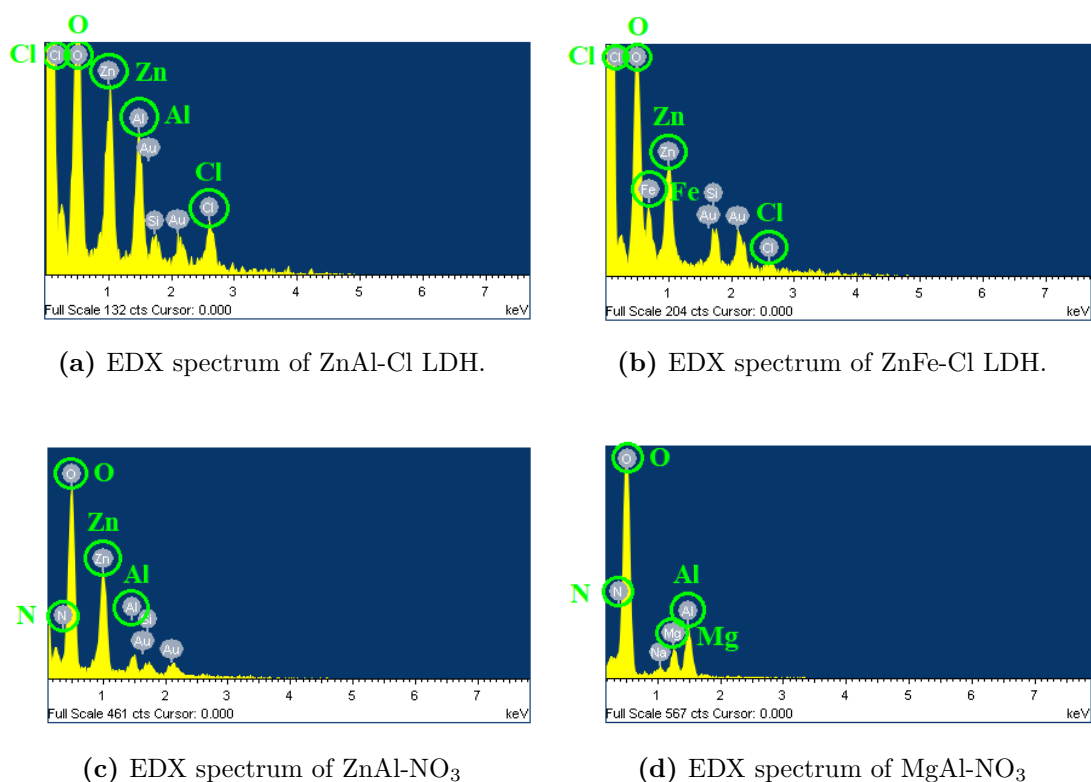


Figure 4.36: XPS spectra of the four different LDH compositions.

	Peak	BE (eV)	Atomic (%)	Atomic Ratio ( $M^{2+}/M^{3+}$ )
<b>ZnAl-Cl</b>	Zn2p <sub>3/2</sub>	1022	1.8	1.5
	Al2p	75.9	1.2	
	Cl2p	198	5.4	
	O1s	530	27.1	
	C1s	289	49.4	
<b>ZnFe-Cl</b>	Zn2p <sub>3/2</sub>	1022	9.1	1.3
	Fe2p <sub>3/2</sub>	89	7.2	
	Cl2p	198	4.1	
	O1s	530	41.0	
	C1s	289	34.1	
<b>ZnAl-NO<sub>3</sub></b>	Zn2p <sub>3/2</sub>	1022	3.8	2.2
	Al2p	75.9	1.7	
	N1s	407	1.0	
	O1s	530	44.7	
	C1s	289	35.0	
<b>MgAl-NO<sub>3</sub></b>	Mg2s	89	5.7	0.5
	Al2p	75.9	11.5	
	N1s	407	3.5	
	O1s	530	49.5	
	C1s	289	26.9	

**Table 4.4:** XPS quantitative results for the analysed samples.

EDX analysis complemented the XPS survey to provide a further estimation of the elemental composition of the active layer. From figure 4.37, it is possible to observe that the main peaks for the four analyzed materials correctly correspond to the chemical elements highlighted in the XPS survey, confirming that the structures are composed by the expected metal constituents Zn, Al, Fe and Mg, by the lattice oxygen and that the two anions, Cl and  $\text{NO}_3$ , were correctly intercalated between the metallic layers. The other peaks can be ignored since corresponding to Au and Si, coming from the electrodes and the underlying  $\text{SiO}_2$  insulating layer respectively.



**Figure 4.37:** EDX spectra of the four different LDH compositions.

Table 4.5 provides an overview of the atomic percentages of the chemical components for the various materials. As it can be noticed, the atomic percentages reported are different if compared to those achieved through the XPS analysis. This behaviour is caused by non-uniformities of the LDH layers, which did not allow a discrimination of the material surface, but involved also small portions of the bulk.

	Element	Atomic (%)
<b>ZnAl-Cl</b>	Zn	11.10
	Al	13.50
	Cl	13.70
	O	56.05
<b>ZnFe-Cl</b>	Zn	11.14
	Fe	16.72
	Cl	3.99
	O	55.54
<b>ZnAl-NO<sub>3</sub></b>	Zn	18.32
	Al	5.69
	N	1.37
	O	67.93
<b>MgAl-NO<sub>3</sub></b>	Mg	7.28
	Al	14.46
	N	1.88
	O	74.8

**Table 4.5:** EDX quantitative results for the analysed samples.

# Chapter 5

## Gas Sensing Measurements

The sensors designed, fabricated and characterized by following the procedures mentioned in Chapter 4 were tested to evaluate their performance in detecting different VOCs at room temperature.

### 5.1 Sensing Setup

The gas sensing tests were performed by employing a custom-made sensing setup composed of a detection chamber (fig.A.3a and b) connected to a gas mixing system able to produce and deliver selected concentrations of different solvent vapours (fig. A.3c), to a data logger needed to register the real-time response of the sensors (fig. A.3c) and to a bubbler evaporator (fig.A.3 d). A stream of dry air is employed both as carrier and diluting gas. As it enters the gas mixing system, it gets separated in two fluxes, regulated by means of a couple of Mass Flow Controllers (MFC). One of these fluxes passes through the bubbler evaporator containing an appropriate solvent, and it recombines with the other before entering the gas detection chamber. A schematic representation of this setup is provided by fig.5.1.

Given the dimensions of the chamber, two sensors could be tested at the same time, and to help their positioning and contacting, a specific structure was realized starting from a PMMA fixture and inserting two couples of electrical contacting probes (see fig. A.3a).

All the gas tests were carried out by setting a constant flow of dry air to 100 sccm<sup>1</sup>, and by varying the concentration of the diluted gases from 1% to 10% (1-10 sccm). The response of the sensors was evaluated for four different analytes: acetone,

---

<sup>1</sup>Standard Cubic Centimeters per Minute. It is used as the flow rate unit and it indicates the amount of gas or volume of gas that passes through a given point in a unit time.

ethanol, ammonium hydroxide and sodium hypochlorite. The results are discussed in the following section.

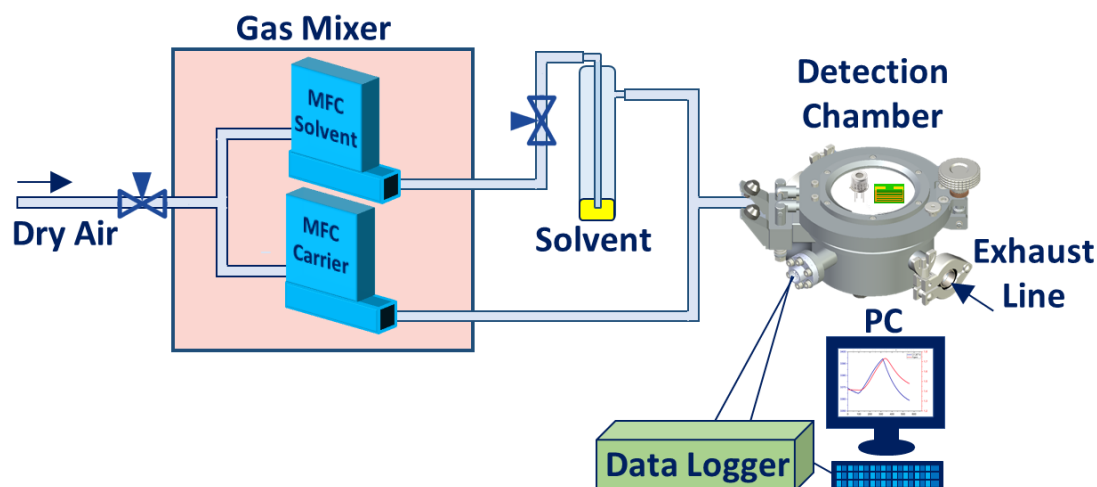


**Figure 5.1:** Schematic representation of the setup employed for the gas sensing measurements [97].

## 5.2 Discussion of results

The real-time response of the sensors, expressed as a variation in electrical resistance, was registered, and their performance was evaluated on the basis of the parameters reported in Chapter 2. In addition, the behaviour of LDH-based sensors was also compared to that of a commercial chemiresistive sensor, the Figaro 2600 series. Differently from the former, which is able to correctly operate at room temperature, the latter is a thick film MOS device employing tin dioxide ( $\text{SnO}_2$ ) as sensing material and which needs a heater to favour the operations of adsorption and desorption of the gases.

For each test, dry air was fluxed in the chamber for 40 s to get a baseline value for the resistance ( $R_a$ ), and the sensors were then exposed to the analyte for 240 s, followed by 360 s of exposure to dry air to recover.

Between successive measurements, to avoid the influence of contamination coming from previous tests or when changing the analytes, the chamber lid was opened and dry air was fluxed for a few minutes.

Each of the sensors showed different sensitivities, selectivities, and response and recovery times according to the LDH employed as active material. Table 5.1 summarizes the main results achieved for the four types of tested sensors.

	Sensor 1	Sensor 2	Sensor 3	Sensor 4
<b>LDH type</b>	ZnAl-Cl	ZnFe-Cl	ZnAl-NO <sub>3</sub>	MgAl-NO <sub>3</sub>
<b>Selectivity</b>	NH <sub>4</sub> OH	All four analytes	NH <sub>4</sub> OH	C <sub>3</sub> H <sub>6</sub> O
<b>Sensitivity</b>	3.8%	4.9%	5%	5.6%
<b>Response time</b>	216 s	188 s	235 s	137 s
<b>Recovery time</b>	243 s	137 s	221 s	194 s
<b>LOD</b>	2 sccm	2 sccm	6 sccm	6 sccm

**Table 5.1:** Summary of the performance parameters of the tested sensors. They refer to the case of 10% concentration of the analyte. When the sensor was sensitive to more than one VOC, as in the case of ZnFe-Cl, only the values related to the best achieved performance were reported.

### 5.2.1 Sensor 1 - ZnAl-Cl LDH

Sensor 1 was able to detect ammonia vapours even at low concentrations (up to 2%). The real-time response of the sensor to 10% concentration of the analyte is shown in figure 5.2a, while the curves for concentrations varying from 2% to 8% are reported in the Appendix (fig.A.4). It is possible to observe that as soon as the sensor detects the gas, the resistance of the sensing element drops down reaching a limiting minimum value. By removing the gas from the chamber and fluxing dry air, the original resistance value is recovered after a certain time. The sensor therefore shows a completely reversible response. The sensitivity could then be evaluated as  $S(\%) = \frac{R_{gas} - R_{air}}{R_{gas}} \cdot 100$  (fig.5.2b). As expected, the sensitivity increases with the concentration of gas fluxed in the chamber, arriving to a maximum value of 3.83%. Figure 5.2c shows the response and recovery times of the sensor as function of the gas concentration. Two opposite behaviours can be observed, since as the quantity of gas entering the chamber increases, quicker is the sensor in detecting it, but larger is the time required to recover after the gas is removed. Figure 5.2d finally shows the repetition of three consecutive cycles obtained by fluxing ammonia vapours at 10% concentration, demonstrating that the sensor possesses good stability and repeatability of results.

In figure 5.2 it is also possible to observe the comparison between the ZnAl-Cl based sensor and the Figaro. The two sensors have two opposite responses, with the commercial one showing an increase in resistance as it is exposed to the analyte. Even if the latter reaches higher sensitivity values, the trend as function of the concentration is the same as the former. As regarding response and recovery times,

the commercial sensor has a faster response to the gas, but a slower recovery, even if provided by an heater element, which should favour the desorption operation.

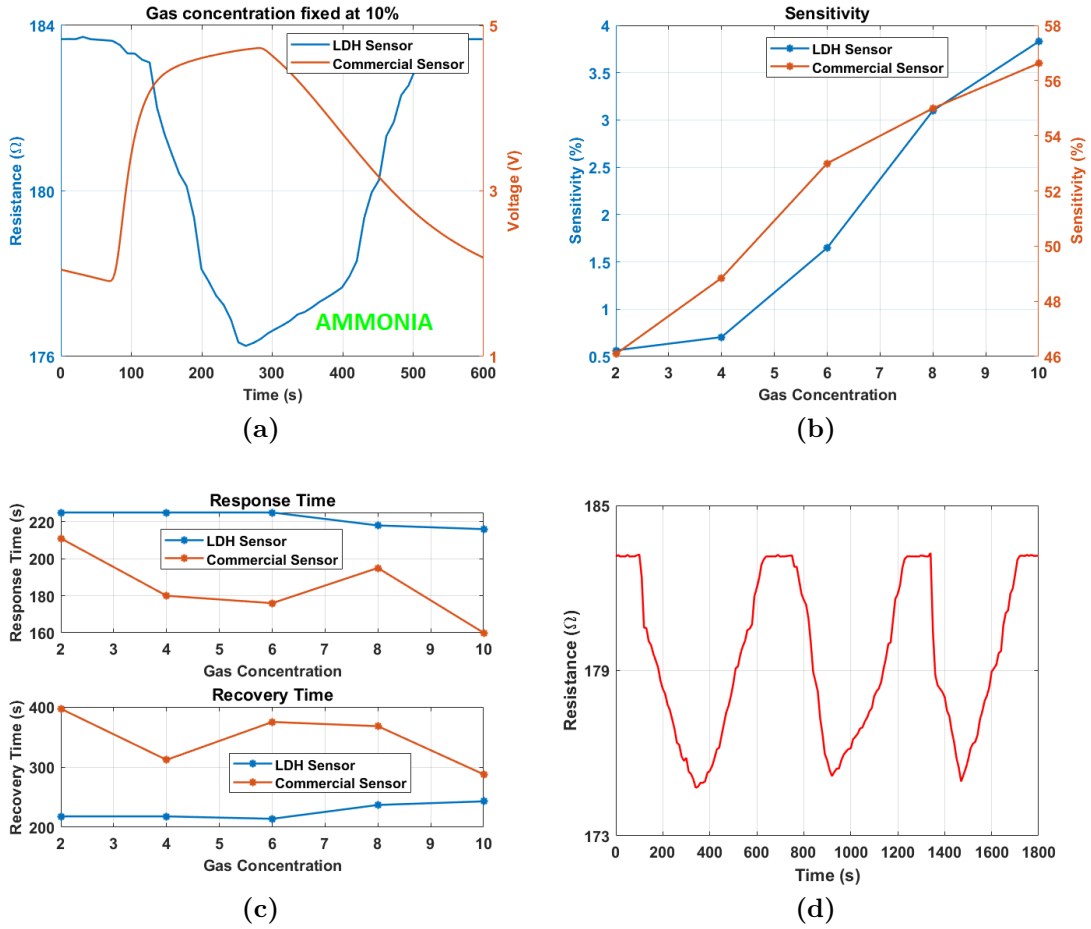


**Figure 5.2:** (a) Real-time response of the sensors to 10% of ammonia vapours. (b) Sensitivity vs Concentration. (c) Response/Recovery time vs Concentration. (d) Three response cycles of the ZnAl-Cl-based sensor to 10% ammonia vapours.

### 5.2.2 Sensor 2 - ZnFe-Cl LDH

Sensor 2 showed a readable response to all the analytes for which it was tested. Figures 5.3, 5.4, 5.5 and 5.6 display the real-time response and performance parameters to acetone, ethanol, ammonia and chlorine vapours at 10% concentration (see fig.A.5, A.6, A.7 in the Appendix for the curves at lower concentrations). As happened for Sensor 1, also in this case a decrease in the resistance values of the active material was observed upon interaction with the analytes. In particular, the best responses were achieved when fluxing ethanol and chlorine vapours, reaching similar values of sensitivity  $\sim 4.9\%$ , while only  $1.1\%$  and  $0.6\%$  were observed when considering acetone and ammonia vapours, even if lower concentrations of this last could be detected (up to  $2\%$ ). Shorter response times characterize Sensor 2 with respect to Sensor 1, and as it will be discussed in the following section, Sensor 3, for all the tested analytes, while it shows the fastest recovery of all the realized sensors. Also in this case, good stability and repeatability of results were observed (fig.5.4d), with just a small loss in sensitivity in the last cycle.

By comparing the LDH-based sensor to the commercial one, the same considerations of the previous section are confirmed. An additional remark can be performed only for the response times of the sensors when fluxing acetone and ammonia vapours at the maximum concentration. From figures 5.3c and 5.5c it is in fact possible to observe that the commercial sensor and the LDH-based one provide a response to the analyte in the same time interval.

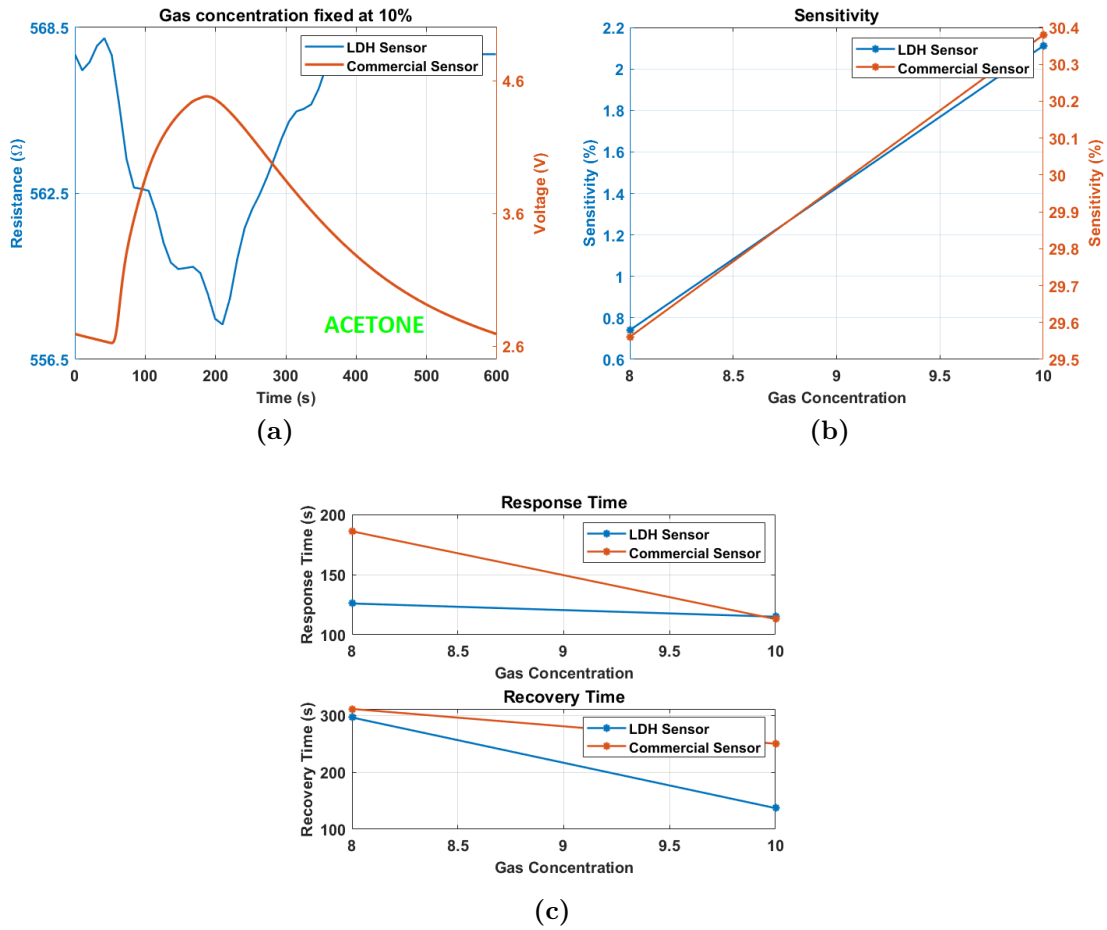


**Figure 5.3:** (a) Real-time response of the sensors to 10% of acetone vapours. (b) Sensitivity vs Concentration. (c) Response/Recovery time vs Concentration.

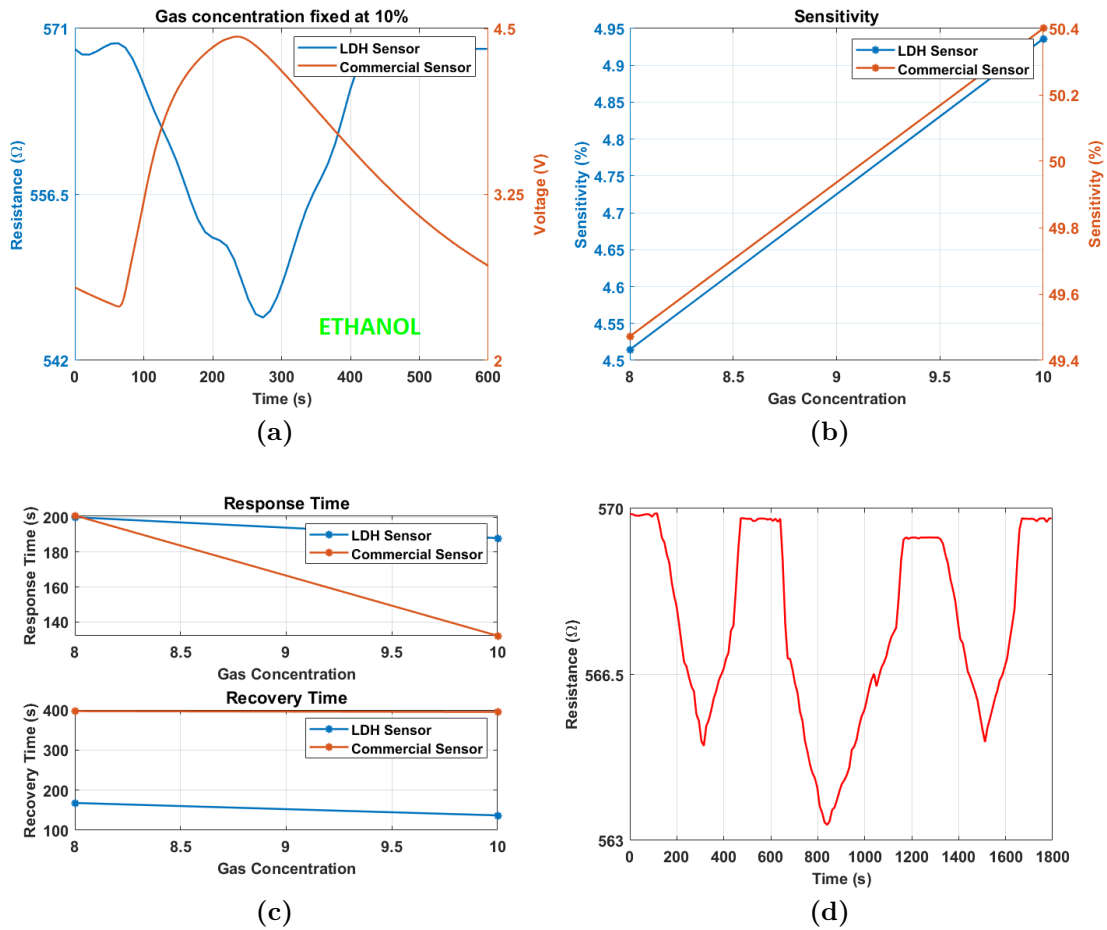


**Figure 5.4:** (a) Real-time response of the sensors to 10% of ethanol vapours. (b) Sensitivity vs Concentration. (c) Response/Recovery time vs Concentration. (d) Three response cycles of the ZnFe-Cl-based sensor to 10% of ethanol vapours.

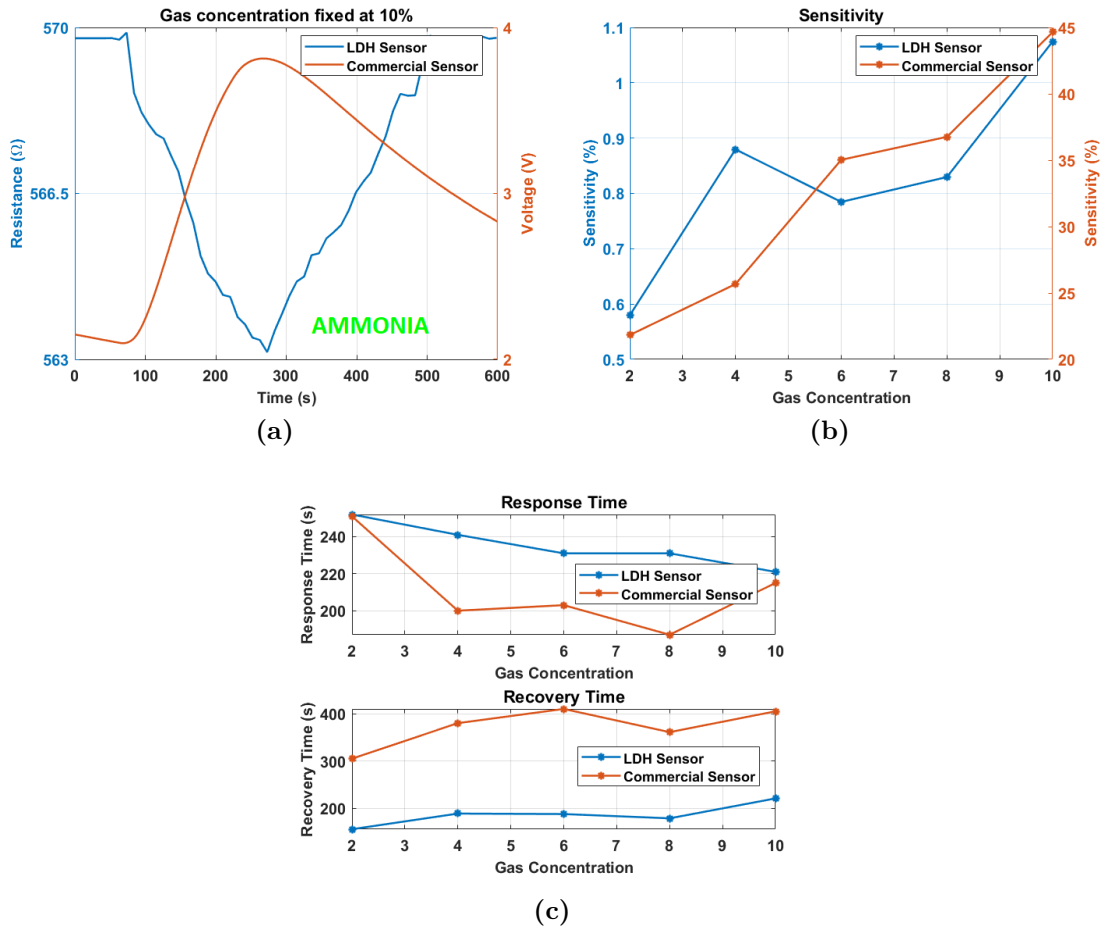


**Figure 5.5:** (a) Real-time response of the sensors to 10% of ammonia vapours. (b) Sensitivity vs Concentration. (c) Response/Recovery time vs Concentration.

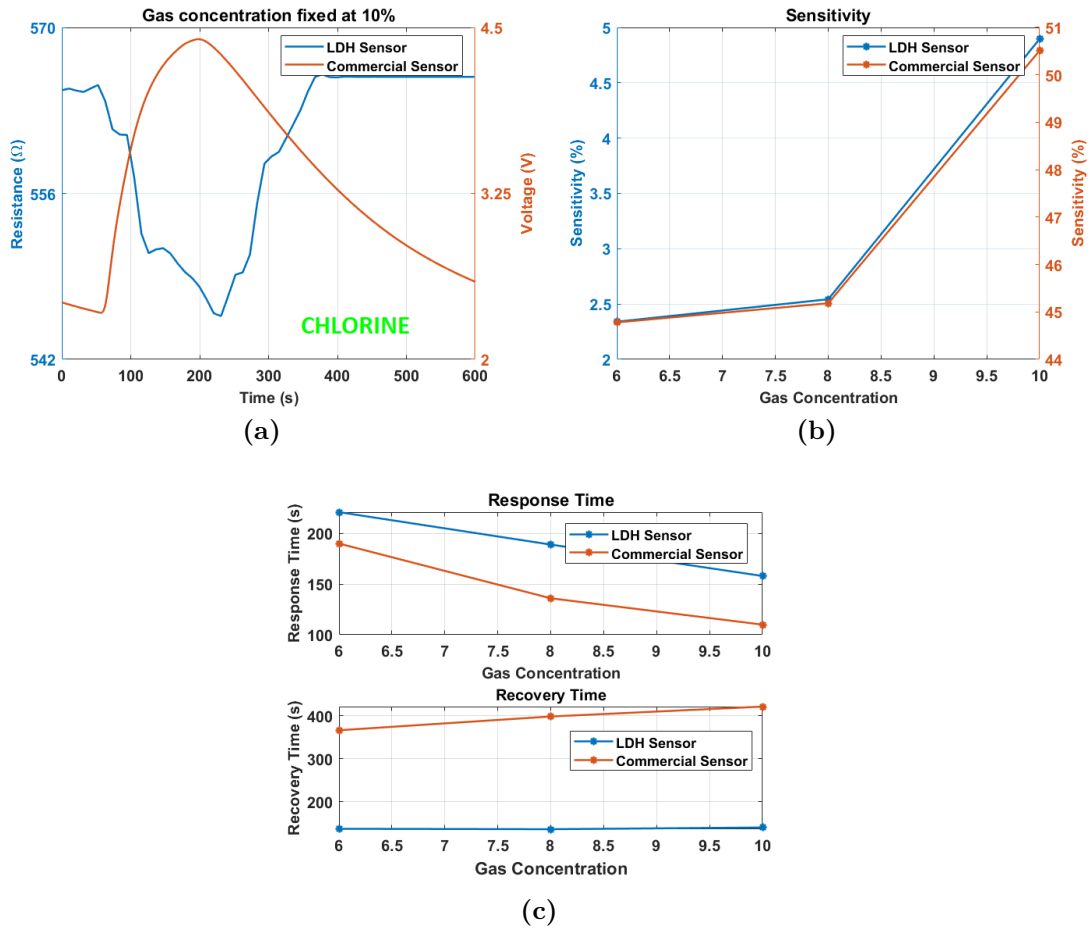


**Figure 5.6:** (a) Real-time response of the sensors to 10% of chlorine vapours. (b) Sensitivity vs Concentration. (c) Response/Recovery time vs Concentration.

### 5.2.3 Sensor 3 - ZnAl-NO<sub>3</sub> LDH

Sensor 3 managed to detect ammonia vapours in a range of 6-10%. The real-time response curve at 10% concentration, together with sensitivity, response/recovery times and stability parameters are shown in figure 5.7 (see fig.A.8 in the Appendix for the response curves at lower concentrations). It shows a sensitivity to ammonia vapours over 5%, so almost 2 points larger than the values achieved by Sensor 1 and Sensor 2, but when compared to the other three LDH-based sensors, it is the slowest in detecting the presence of the analyte. Its superior performance, when compared to Sensor 1, in detecting ammonia vapours could be explained on the basis of two factors: (1) as evidenced by the FESEM and XPS analysis, ZnAl-NO<sub>3</sub> LDH shows a higher Al content, which leads to the formation of smaller nanosheets aggregates, so to platelets having a reduced thickness which favour gas diffusion throughout the material surface and bulk; (2) the intercalation of NO<sub>3</sub> anions instead of Cl ones acts on the overall three-dimensional structure of the material, since enlarging the spacing between successive positive cationic layers, so resulting in larger pathway galleries for the transportation of gas.

As regarding the comparison with the commercial sensor, the considerations performed in the previous sections remain valid.

### 5.2.4 Sensor 4 - MgAl-NO<sub>3</sub> LDH

Sensor 4 only responded to acetone vapours at concentrations varying from 6% to 10%. Its real-time response curve at 10% concentration, together with the other performance parameters are displayed in figure 5.8 (see fig.A.9 in the Appendix for the response curves at lower concentrations). It shows the highest sensitivity value between the four LDH-based sensors, reaching a value  $\sim 5.6\%$  and it is faster than Sensor 2 in detecting acetone vapours.

When compared to the Figaro, not only it shows a superior performance relative to the recovery operation, but it also has a fastest response when detecting the analyte both at 8% and 10%.

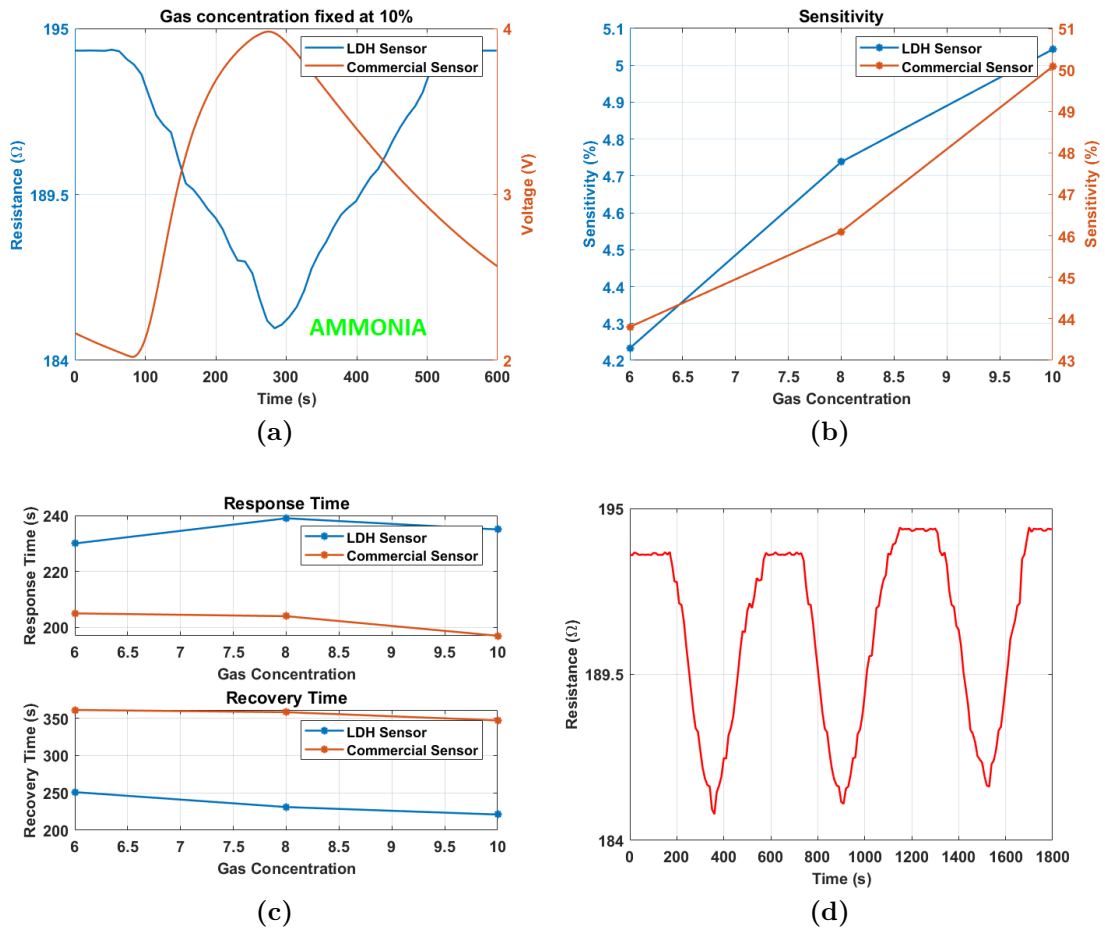


**Figure 5.7:** (a) Real-time response of the sensors to 10% of ammonia vapours. (b) Sensitivity vs Concentration. (c) Response/Recovery time vs Concentration. (d) Three response cycles of the ZnAl-NO<sub>3</sub>-based sensor to 10% ammonia vapours.

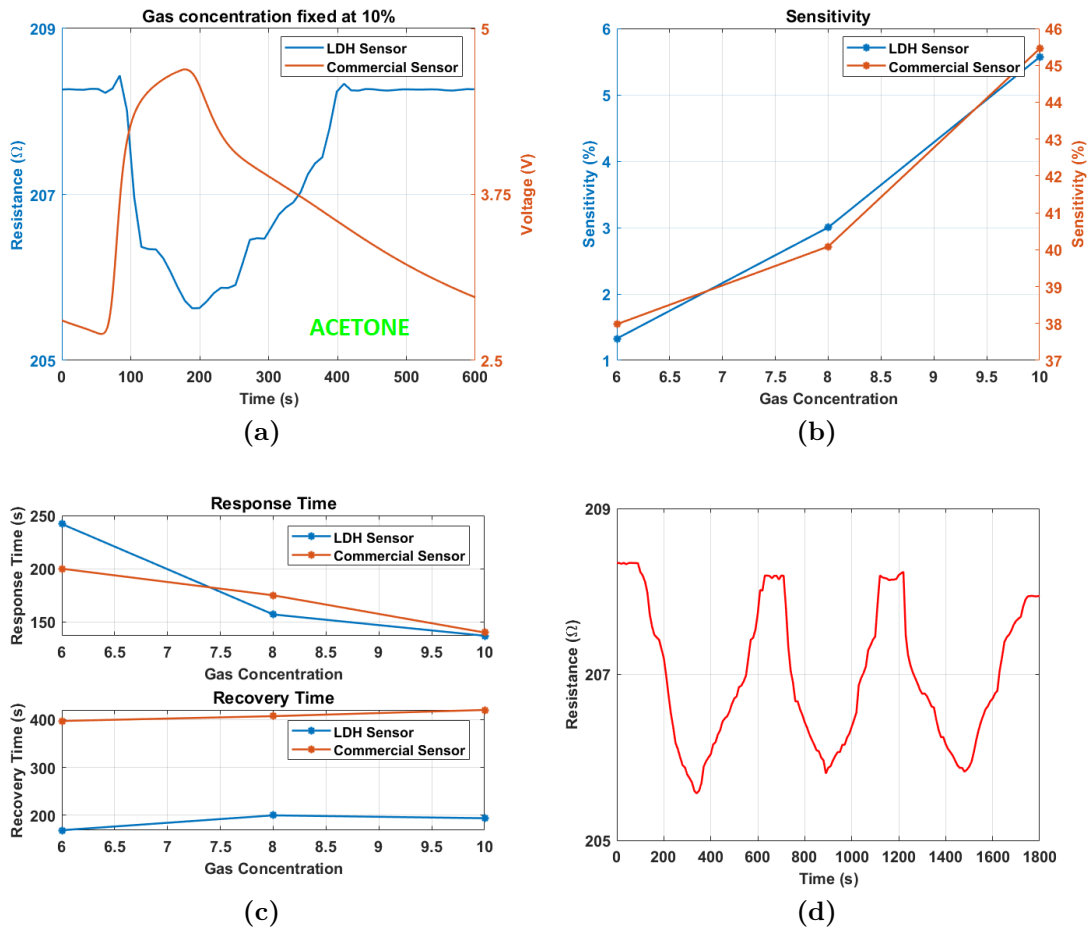


**Figure 5.8:** (a) Real-time response of the sensor to 10% of acetone vapours. (b) Sensitivity vs Concentration. (c) Response/Recovery time vs Concentration. (d) Three response cycles of the MgAl-NO<sub>3</sub>-based sensor to 10% acetone vapours.

As discussed in the previous sections, each sensor showed different responses to the tested analytes. By collecting this information, it was possible to construct a selectivity plot (fig.5.9). It can be observed that Sensor 1 (ZnAl-Cl), Sensor 3 (ZnAl-NO<sub>3</sub>) and Sensor 4 (MgAl-NO<sub>3</sub>) showed an excellent selectivity at room temperature, being able to discriminate a unique analyte.

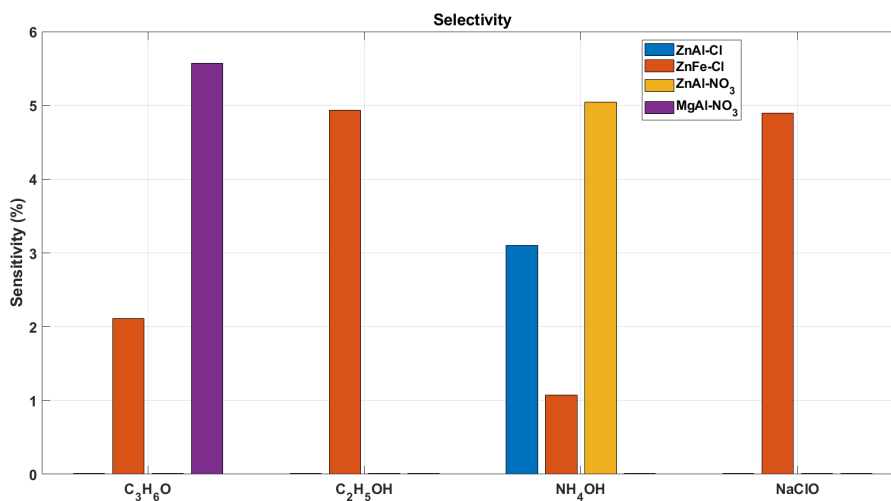


**Figure 5.9:** Selectivity results of the 4 LDH-based sensors to acetone, ethanol, ammonia and chlorine vapours at 10% concentration.

## Chapter 6

# Conclusions and future works

A set of chemiresistive gas sensors employing Layered Double Hydroxides as sensing element were successfully designed, fabricated, characterized and tested for the detection of volatile organic compounds. The gas sensing tests showed that all the LDH-based sensors were correctly able to reversibly detect acetone, ethanol, ammonia and chlorine vapours at room temperature, reaching sensitivity values up to  $\sim 6\%$ , comparable to many results reported in literature. From stability tests, performed by evaluating the sensors' response on three consecutive cycles, satisfying results were achieved. A good repeatability was in fact observed, with all the sensors showing a complete recovery, making them suitable for reversible long-time applications.

As explored through SEM, FTIR, XPS and EDX analysis, each considered LDH showed sensitivities and selectivities to the tested VOCs which varied according to the material chemical composition and to its morphology. As an example, the variation of the interlayer anion from Cl to  $\text{NO}_3$  in ZnAl-LDH structures caused an increase in sensitivity to ammonia vapours, since the gas could easily penetrate and diffuse throughout the material bulk.

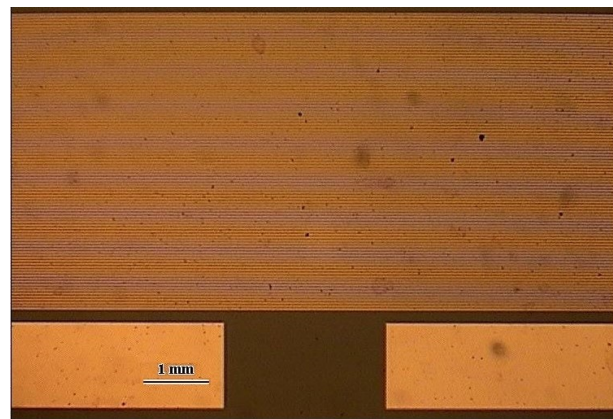
Thanks to their excellent selective behaviour, it may be suitable to employ them for the realization of small electronic noses. As an example, in our specific case, by testing at the same time the responses of ZnAl-LDH (either intercalated with Cl or  $\text{NO}_3$ ) and MgAl-LDH it is possible to discriminate ammonia from acetone vapours. The performance of the LDH-based sensors was compared to that of a commercial sensor, the Figaro 2600 series, a thick film MOS device whose sensing material is  $\text{SnO}_2$  and provided by a heater to favour the gas adsorption/desorption operations. The latter showed better sensitivity values, but comparable response time intervals, and a slower recovery than the former, which represent a remarkable result since

the LDH-based sensors completely operate at room temperature, without the requirement of a heating element.

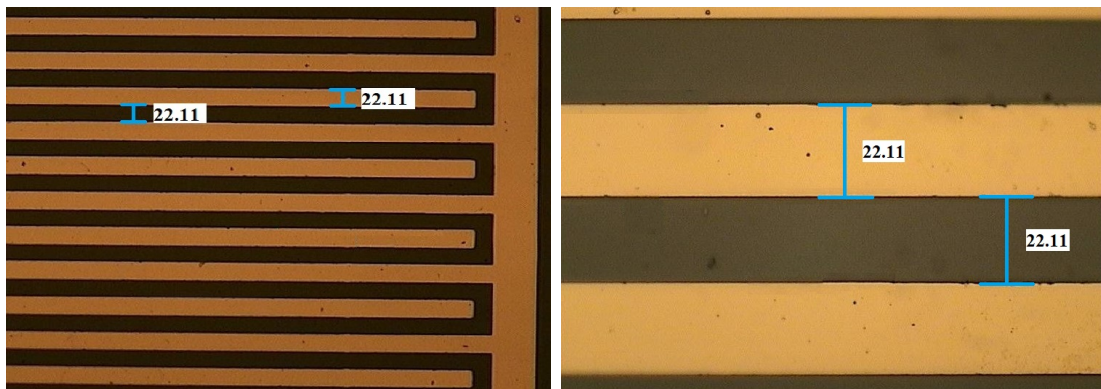
In conclusion, the LDH-based gas sensors show an incredible range of potentialities to be explored. To improve their performances, a possibility to consider could be to act on the chemical composition of the LDHs, by considering different cations and anions combinations, and by tuning the  $M^{2+}/M^{3+}$  ratio, attempting to obtain highly hierarchical and ordered structures, with the typical flower-like morphology. Attempts should also be made towards the optimization of the dispersion and deposition steps, which in this work lead to sensing layers showing an extremely poor uniformity. As an example, it may be possible to proceed in performing different drop-casting cycles of the dispersed LDH solution by repeatedly dropping controlled amounts of the dispersion over the electrodes, followed by short thermal treatments, until a uniform film is obtained. Through this operation, also the porosity of the material could be improved. In this way, different analytes could eventually be detected, even at lower concentrations.

# Appendix A

## Supplementary figures



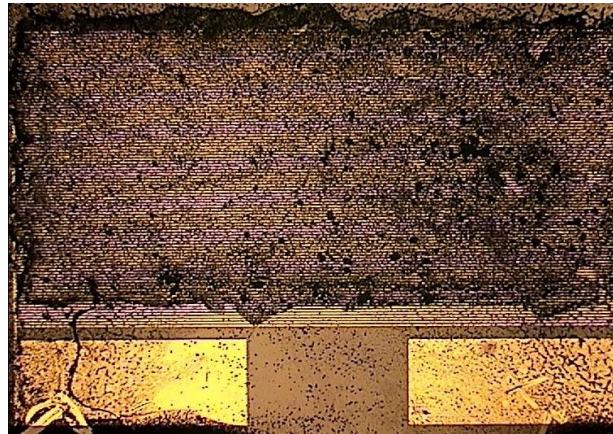
(a)



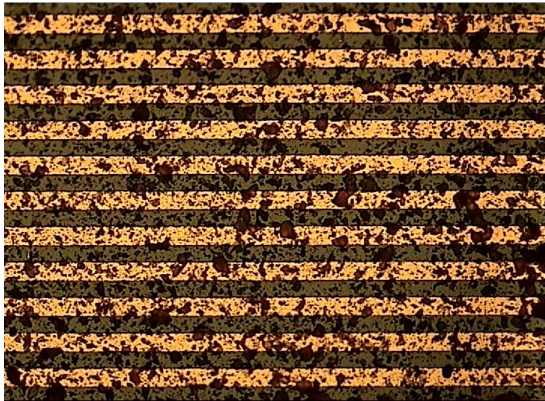
(b)

(c)

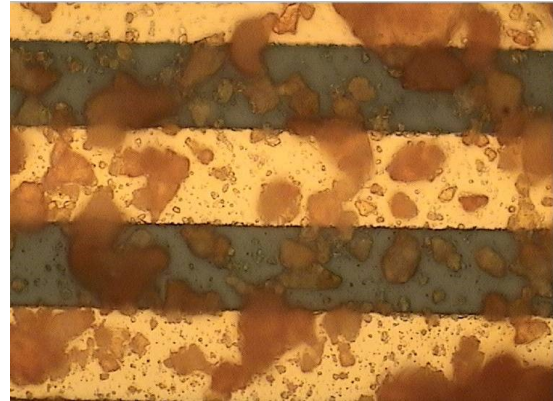
**Figure A.1:** Details of the gap distance and of the width of IDE fingers after the lift off process.



(a)

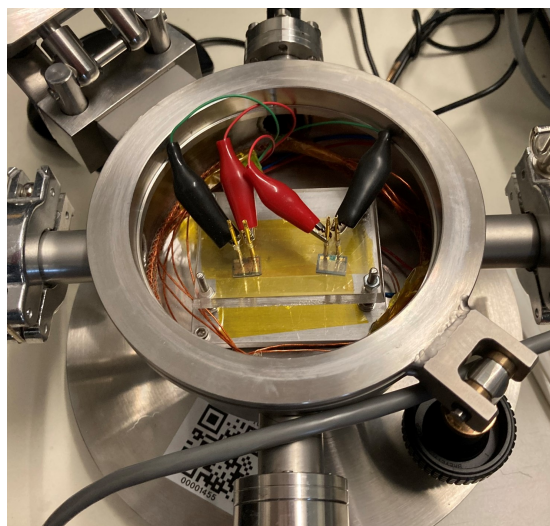


(b)

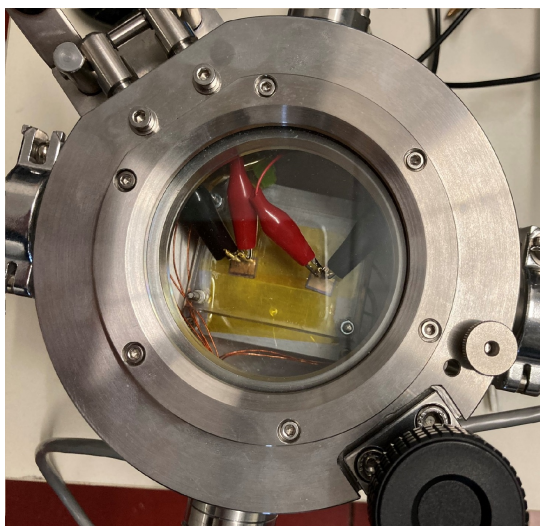


(c)

**Figure A.2:** Images of the sensor at the end of the fabrication process. The LDH layers, as mentioned, are deposited only over the IDEs.



(a) Gas sensing chamber (open).



(b) Gas sensing chamber (closed).



(c) Data logger (up) and gas mixing system (down).



(d) Bubbler evaporation system.

**Figure A.3:** Experimental setup of the gas sensing system employed to test the response of the LDH-based sensors.

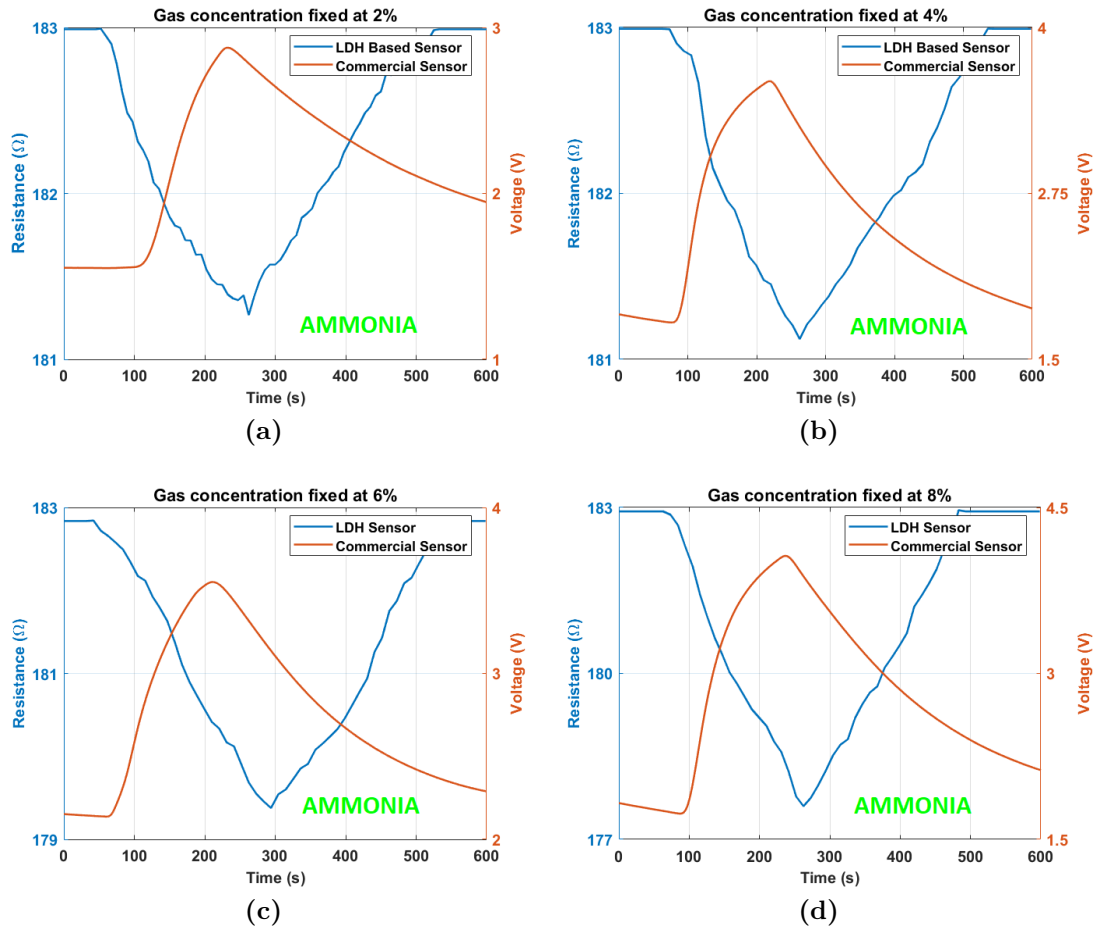


**Figure A.4:** Real-time response curves for Sensor 1 (ZnAl-Cl LDH) to ammonia vapours at (a) 2%, (b) 4%, (c) 6% and (d) 8% concentration.

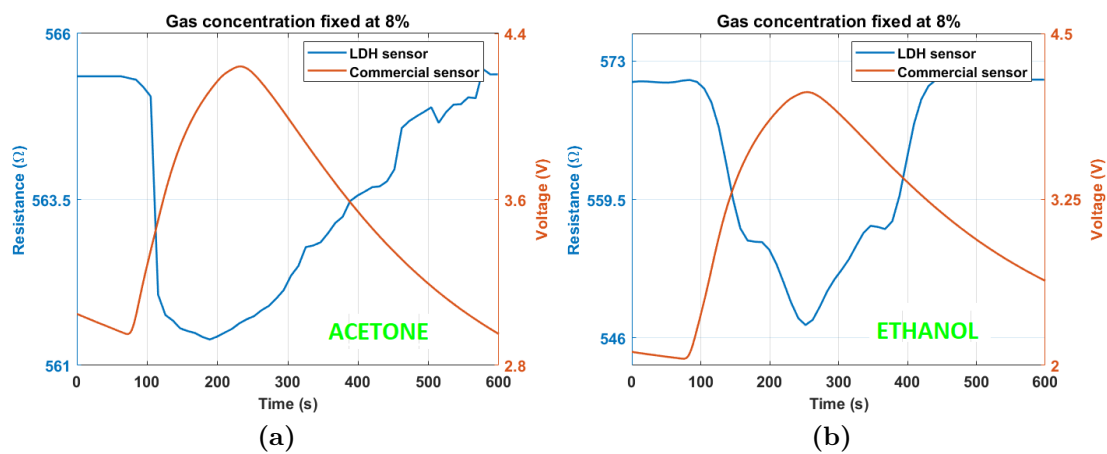


**Figure A.5:** Real-time response curves for Sensor 2 (ZnFe-Cl) to (a) acetone and (b) ethanol at 8% concentration.

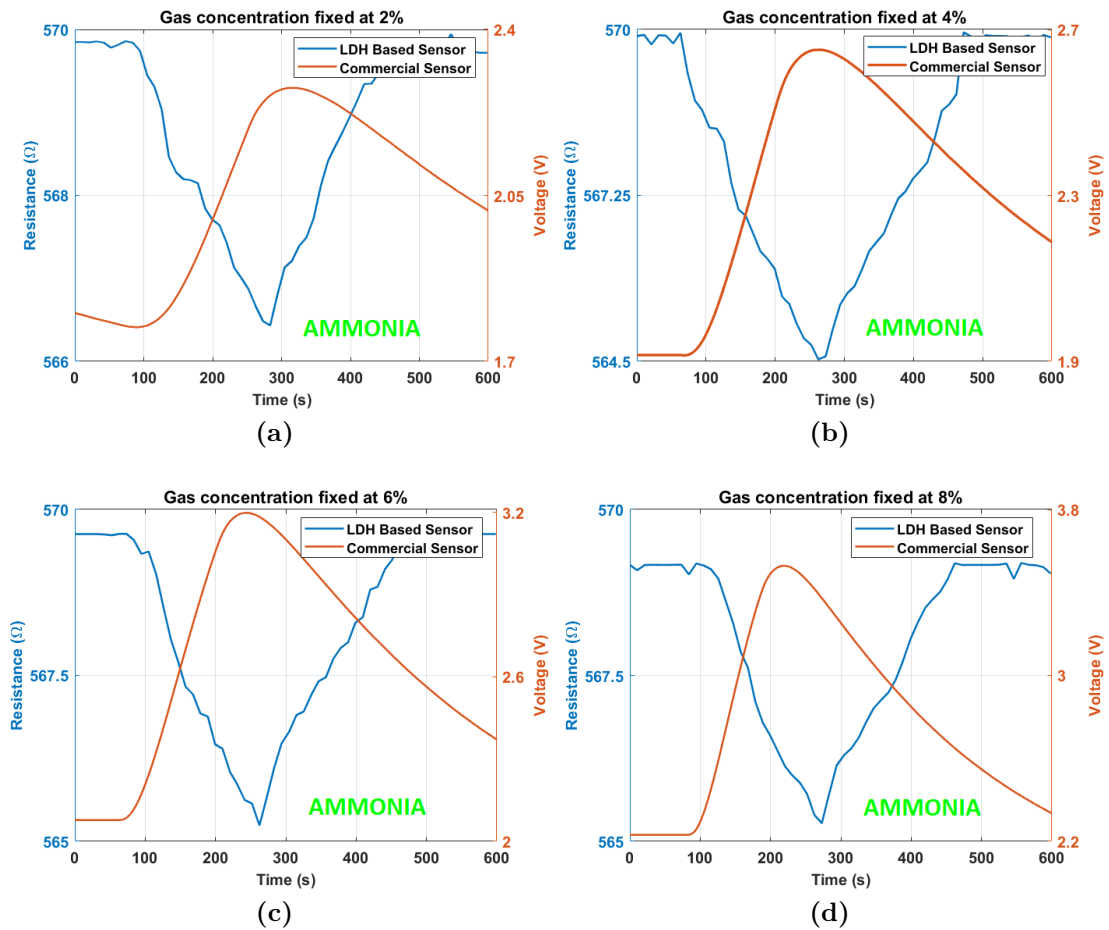


**Figure A.6:** Real-time response curves for Sensor 2 (ZnFe-Cl) to ammonia vapours at (a) 2%, (b) 4%, (c) 6% and (d) 8% concentration.

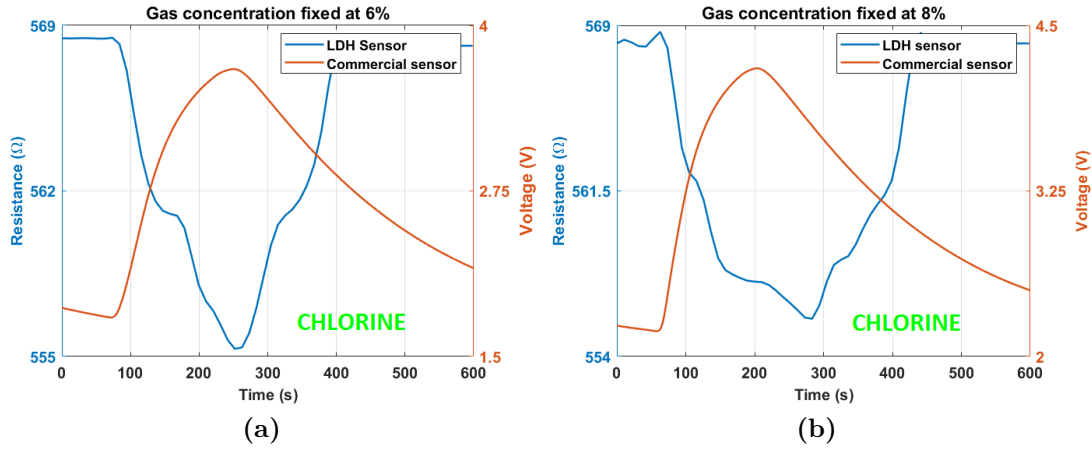


**Figure A.7:** Real-time response curves for Sensor 2 (ZnFe-Cl) to chlorine vapours at (a) 6% and (b) 8% concentration.

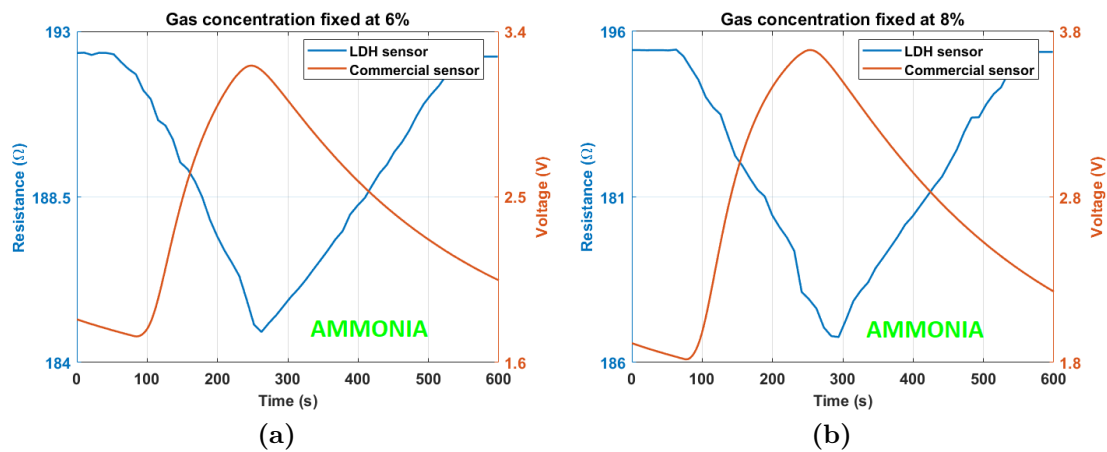


**Figure A.8:** Real-time response curves for Sensor 3 (ZnAl-NO<sub>3</sub>) to ammonia vapours at (a) 6% and (b) 8% concentration.

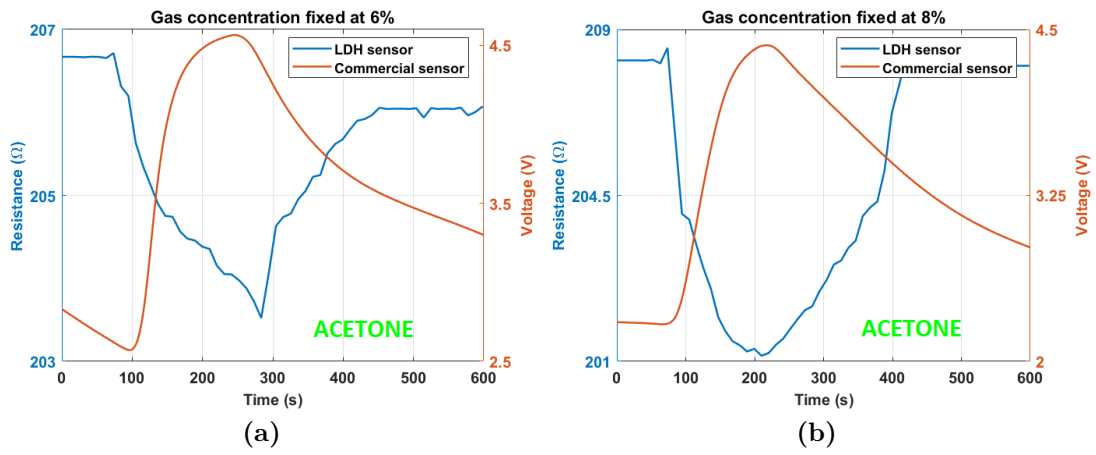


**Figure A.9:** Real-time response curves for Sensor 4 ( $\text{MgAl-NO}_3$ ) to acetone vapours at (a) 6% and (b) 8% concentrations.

# Bibliography

- [1] K. Arshak; E. Moore; G.M. Lyons; J. Harris; S. Clifford. «A review of gas sensors employed in electronic nose applications». In: *Sensor Review* 24.2 (2004), pp. 181–198 (cit. on pp. 14, 21, 27–29, 31–37, 42–46, 48, 50).
- [2] H.T. Nagle; S.S. Schiffman; R.G. Gutierrez-Osuna. «The How and Why of Electronic Noses». In: *IEEE Spectrum* 35.9 (1998), pp. 22–34 (cit. on pp. 14–16, 18, 54).
- [3] J.W. Gardner. «A brief history of electronic noses». In: *Sensors and Actuators B* 18 (1994), pp. 211–220 (cit. on p. 15).
- [4] A.M. Kotecha; A.D.C. Correa; K.M. Fisher; J.V. Rushworth. «Olfactory Dysfunction as a Global Biomarker for Sniffing out Alzheimers Disease: A Meta-Analysis». In: *Biosensors* 8 (2018), p. 41 (cit. on p. 16).
- [5] A.P.F. Turner; N. Magan. «Electronic noses and disease diagnostics». In: *Nature Reviews Microbiology* 2 (2004), pp. 161–166 (cit. on p. 18).
- [6] A.D. Wilson; M. Baietto. «Advances in electronic-nose technologies developed for biomedical applications». In: *Sensors* 11 (2011), pp. 1105–1176 (cit. on p. 18).
- [7] E.A. Baldwin; J. Bai; A. Plotto; S. Dea. «Electronic Noses and Tongues: Applications for the Food and Pharmaceutical Industries». In: *Sensors* 11 (2011), pp. 4744–4766 (cit. on p. 18).
- [8] F. Rock; N. Barsan; U. Weimar. «Electronic Nose: Current Status and Future Trends». In: *Chemical Reviews* 108.2 (2008), pp. 705–725 (cit. on pp. 18, 53, 54).
- [9] F. Tsow; E. Forzani; A. Rai; W. Rui; R. Tsui; S. Mastroianni; C. Knobbe; A.J. Gandolfi; N.J. Tao. «A Wearable and wireless sensor system for real-time monitoring of toxic environmental volatile organic compounds». In: *IEEE Sensors Journal* 9 (2009), pp. 1734–1740 (cit. on p. 18).

- 
- [10] L. Zhang; F. Tian; H. Nie; L. Dang; G. Li; Q. Ye; C. Kadri. «Classification of multiple indoor air contaminants by an electronic nose and a hybrid support vector machine». In: *Sensors and Actuators B: Chemical* 174 (2012), pp. 114–125 (cit. on p. 18).
- [11] G. Korotchenkov; V. Brynzari; S. Dmitriev. «SnO<sub>2</sub> thin film gas sensors for fire-alarm systems». In: *Sensors and Actuators B: Chemical* 54 (1999), pp. 191–196 (cit. on p. 18).
- [12] J. Goschnick; M. Harms. «Landmine detection with an electronic nose mounted on an airship». In: *NATO Science Series* 66 (2002), pp. 83–91 (cit. on p. 18).
- [13] A.D. Wilson; M. Baietto. «Applications and Advances in Electronic-Nose Technologies». In: *Sensors* 9 (2009), pp. 5009–5148 (cit. on p. 19).
- [14] D.K. Aswal; S.K. Gupta. *Science and Technology of Chemiresistor Gas Sensors*. Nova Science Publishers, 2007 (cit. on pp. 21, 24, 37).
- [15] P.K. Kannan; D.J. Late; H. Morgan; C.S. Rout. «Recent Developments in 2D Layered Inorganic Nanomaterials for Sensing». In: *Nanoscale* 7 (2015), pp. 13293–13312 (cit. on p. 21).
- [16] S. Yang; C. Jiang; S. Wei. «Gas sensing in 2D materials». In: *Applied Physics Reviews* 4 (2017) (cit. on pp. 22–24).
- [17] T.C. Pearce; S.S. Schiffman; H.T. Nagle; J.W. Gardner. *Handbook of Machine Olfaction*. WILEY-VCH Verlag GmbH Co. KGaA, 2003 (cit. on pp. 22, 24–26, 40–43, 45, 46, 51, 52).
- [18] C. Lupan; A. Schtt; A. Brnaz; M. Hoppe; R. Adelung. «Sensorial and Local Reflectivity Properties of the Columnar ZnO:Eu Films». In: *Tiginyanu I., Sontea V., Railean S. (eds) 4th International Conference on Nanotechnologies and Biomedical Engineering. ICNBME 2019. IFMBE Proceedings* 77 (2019), pp. 253–257 (cit. on p. 23).
- [19] B. Munoz; G. Steinthal; S. Sunshine. «Conductive polymer-carbon black composites-based sensor arrays for use in an electronic nose». In: *Sensor Review* 19.4 (1999), pp. 300–305 (cit. on pp. 27–30).
- [20] K. Albert; N. S. Lewis; C.L. Schauer; G. A. Sotzing; S.E. Stitzel; T.P. Vaid; D.R. Walt. «Cross-Reactive Chemical Sensor Arrays». In: *Chemical Reviews* 100.7 (2000), pp. 2595–2626 (cit. on pp. 27, 28, 30, 31, 35, 36, 41, 42, 45, 48).
- [21] F. Zee; J.W. Judy. «Micromachined polymer-based chemical gas sensor array». In: *Sensors and Actuators B: Chemical* 72.2 (2001), pp. 120–128 (cit. on pp. 29, 30).

- [22] H.J. Kim; J.H. Lee. «Highly sensitive and selective gas sensors using p-type oxide semiconductors: Overview». In: *Sensors and Actuators B: Chemical* 192 (2014), pp. 607–627 (cit. on pp. 32–37).
- [23] K. Ihokura; J. Watson. *The Stannic Oxide Gas Sensor : Principles and Applications*. 2000 Corporate Blvd., N.W., Boca Raton, Florida 33431: CRC Press, Inc, 1994 (cit. on p. 37).
- [24] M. Heule; L.J. Gauckler. «Miniaturised arrays of tin oxide gas sensors on single microhotplate substrates fabricated by micromolding in capillaries». In: *Sensors and Actuators B* 93 (2003), pp. 100–106 (cit. on p. 38).
- [25] I. Simon; N. Barsan; M. Bauer; U. Weimar. «Micromachined metal oxide gas sensors: opportunities to improve sensor performance». In: *Sensors and Actuators B* 73 (2001), pp. 1–26 (cit. on pp. 38, 39).
- [26] S.L. Marasso; A. Tommasi; D. Perrone; M. Cocuzza; R. Mosca; M. Villani; A. Zappettini; D. Calestani. «A new method to integrate ZnO nano-tetrapods on MEMS micro-hotplates for large scale gas sensor production». In: *Nanotechnology* 27.38 (2016), p. 385503 (cit. on pp. 39, 40).
- [27] G. Faglia; E. Comini; A. Cristalli; G. Sberveglieri; L. Dori. «Very low power consumption micromachined CO sensors». In: *Sensors and Actuators B* 55 (1999), pp. 140–146 (cit. on p. 39).
- [28] D. Briand; A. Krauss; B. van der Schoot; U. Weimar; N. Barsan; W. Gopel; N.F. de Rooij. «Design and fabrication of high-temperature micro-hotplates for drop-coated gas sensors». In: *Sensors and Actuators B* 68 (2000), pp. 223–233 (cit. on p. 39).
- [29] T. Ishihara; S. Matsubara. «Capacitive Type Gas Sensors». In: *Journal of Electroceramics* 2.4 (1998), pp. 215–228 (cit. on p. 40).
- [30] A.S. Yuwono; P.S. Lammers. «Odor Pollution in the Environment and the Detection Instrumentation». In: *Agricultural Engineering International: the CIGR Journal of Scientific Research and Development* 6 (2004) (cit. on p. 42).
- [31] J. Devkota; P.R. Ohodnicki; D.W. Greve. «SAW Sensors for Chemical Vapors and Gases». In: *Sensors* 17 (2017) (cit. on pp. 43, 44).
- [32] P. Bergveld. «The Impact of MOSFET-based Sensors». In: *Sensors and Actuators* 8 (1985), pp. 109–127 (cit. on pp. 46, 47, 49, 50).
- [33] M. Adalchi-Pagano; C. Forano; J.P. Besse. «Synthesis of Al-rich hydrotalcite-like compounds by using the urea hydrolysis reaction control of size and morphology». In: *Journal of Materials Chemistry* 13 (2003), pp. 1988–1993 (cit. on pp. 49, 69).
- [34] J.N. Zemel. «Future directions for thermal information sensors». In: *Sensors and Actuators A* 56 (1996), pp. 57–62 (cit. on p. 51).

- [35] W.J. Buttner. «An Integrated Amperometric Microsensor». In: *Sensors and Actuators B* 1 (1990), pp. 303–307 (cit. on p. 52).
- [36] Qiang Wang; Dermot OHare. «Recent Advances in the Synthesis and Application of Layered Double Hydroxide (LDH) Nanosheets». In: *Chem. Rev.* 112 (2012), pp. 4124–4155 (cit. on pp. 55, 111).
- [37] Yuxiang Qin; Liping Wang; Xiaofei Wang. «Hierarchical layered double hydroxides with Ag nanoparticle modification for ethanol sensing». In: *Nanotechnology* 29 (2018). 275502 (cit. on pp. 55, 70, 71, 111).
- [38] D. Polese; A. Mattoccia; F. Giorgi; L. Pazzini; L. Di Giamberardino; G. Fortunato; P.G. Medaglia. «A phenomenological investigation on Chlorine intercalated Layered Double Hydroxides used as room temperature gas sensors». In: *Journal of Alloys and Compounds* 692 (2017), pp. 915–922 (cit. on p. 56).
- [39] Faiza Bergaia; Benny K.G. Theng; Gerhard Lagaly. *Handbook of Clay Science*. The Boulevard, Langford Lane, Kidlington, Oxford OX5 1GB, UK; Radarweg 29, PO Box 211, 1000 AE Amsterdam, The Netherlands: Elsevier, 2006. Chap. 13 (cit. on pp. 57, 61–63, 67, 69, 75, 76).
- [40] F.L.Theiss; G.A. Ayoko; R.L. Frost. «Synthesis of layered double hydroxides containing  $Mg^{2+}$ ,  $Zn^{2+}$ ,  $Ca^{2+}$  and  $Al^{3+}$  layer cations by co-precipitation methods A review». In: *Applied Surface Science* 383 (2016), pp. 200–213 (cit. on p. 57).
- [41] A. de Roy; C. Forano; K.El Malki; J.P. Besse. «Anionic Clays: Trends in Pillaring Chemistry». In: *M.L. Occelli; H.E. Robson (eds) Expanded Clays and Other Microporous Solids*, Springer, Boston, MA (1992) (cit. on p. 59).
- [42] M. Bellotto; B. Rebours; O. Clause; J. Lynch; D. Bazin; E. Elkaim. «A Reexamination of Hydrotalcite Crystal Chemistry». In: *The Journal of Physical Chemistry* 100.20 (1996), pp. 8527–8534 (cit. on p. 60).
- [43] M. Vucelic; W. Jones; G.D. Moggridge. «Cation Ordering in Synthetic Layered Double Hydroxides». In: *Clay and Clay Minerals* 45.6 (1997), pp. 803–813 (cit. on p. 60).
- [44] A.S. Bookin; V.I. Cherkashin; V.A. Drits. «Polytype Diversity of the Hydrotalcite-like Minerals II. Determination of the Polytypes of Experimentally Studied Varieties». In: *Clay and Clay Minerals* 41.5 (1993), pp. 558–564 (cit. on pp. 60, 61).
- [45] J.T.Klopprogge; D. Wharton; L.Hickey; R.L. Frost. «Infrared and Raman study of interlayer anions  $CO_3^{2-}$ ,  $NO_3^-$ ,  $SO_4^{2-}$  and  $ClO_4^-$  in Mg/Al hydrotalcite». In: *American Mineralogist* 87 (2002), pp. 623–629 (cit. on p. 61).

- [46] U. Costantino; F. Leroux; M. Nocchetti; C. Mousty. «LDH in Physical, Chemical, Biochemical, and Life Sciences». In: *Developments in Clay Science* 5B (2013), pp. 765–791 (cit. on p. 62).
- [47] Z.P. Xu; H.C. Zeng. «Abrupt Structural Transformation in Hydrotalcite-like Compounds  $Mg_{1-x}Al_x(OH)_2(NO_3)_x \cdot nH_2O$  as a Continuous Function of Nitrate Anions». In: *Journal of Physical Chemistry* 105 (2001), pp. 1743–1749 (cit. on p. 63).
- [48] Z.P. Xu; H.C. Zeng. «Decomposition Pathways of Hydrotalcite-like Compounds  $Mg_{1-x}Al_x(OH)_2(NO_3)_x \cdot nH_2O$  as a Continuous Function of Nitrate Anions». In: *Chemistry of Materials* 13 (2001), pp. 4564–4572 (cit. on p. 63).
- [49] S.M. Xu; T. Pan; Y.B. Dou; H. Yan; S.T. Zhang; F.Y. Ning; W.Y. Shi; M. Wei. «Theoretical and Experimental Study on  $M^{II}M^{III}$ -Layered Double Hydroxides as Efficient Photocatalysts toward Oxygen Evolution from Water». In: *The Journal of Physical Chemistry* 119 (2015), pp. 18823–18834 (cit. on pp. 63–65).
- [50] J. Oh; S. Hwang; J. Choy. «The effect of synthetic conditions on tailoring the size of hydrotalcite particles». In: *Solid State Ionics* 151 (2002), pp. 285–291 (cit. on pp. 65–68).
- [51] M. del Arco; V. Rives; R. Trujillano. «Surface and textural properties of hydrotalcite-like materials and their decomposition products». In: *Studies in Surface Science and Catalysis* 87 (1994), pp. 507–515 (cit. on pp. 69, 70).
- [52] J.I. Di Cosimo; V.K. Diez; M. Xu; E. Iglesia; C.R. Apestagua. «Studies in Surface Science and Catalysis». In: *Journal of Catalysis* 178 (1998), pp. 499–510 (cit. on p. 69).
- [53] S. Mandal; S. Mayadevi. «Adsorption of fluoride ions by ZnAl layered double hydroxides». In: *Applied Clay Science* 40 (2008), pp. 54–62 (cit. on p. 70).
- [54] F. Malherbe; J.P. Besse. «Investigating the Effects of Guest-Host Interactions on the Properties of Anion-Exchanged Mg-Al Hydrotalcites». In: *Journal of Solid State Chemistry* 155 (2000), pp. 332–341 (cit. on p. 70).
- [55] H. Sun; Z. Chu; D. Hong; G. Zhang; Y. Xie; L. Li; K. Shi. «Three-dimensional hierarchical flower-like MgAl-layered double hydroxides: Fabrication, characterization and enhanced sensing properties to  $NO_x$  at room temperature». In: *Journal of Alloys and Compounds* 658 (2016), pp. 561–568 (cit. on pp. 71, 72).
- [56] Z. Liu; L. Teng; L. Ma; Y. Liu; X. Zhang; J. Xue; M. Ikram; M. Ullah; L. Li; K. Shi. «Porous 3D flower-like CoAl-LDH nanocomposite with excellent performance for  $NO_2$  detection at room temperature». In: *The Royal Society of Chemistry* 9 (2019), pp. 21911–21921 (cit. on pp. 71–73, 88, 89).

- [57] G. Arrabito; A. Bonasera; G. Prestopino; A. Orsini; A. Mattoccia; E. Martinelli; B. Pignataro; P.G. Medaglia. «Layered Double Hydroxides: A Toolbox for Chemistry and Biology». In: *Crystals* 9, 361 (2019) (cit. on p. 74).
- [58] T. Hibino; Y. Yamashita; K. Kosuge; A. Tsunashima. «Decarbonation Behaviour of Mg-Al-CO<sub>3</sub> Hydrotalcite-like Compounds During Heat Treatment». In: *Clay and Clay Minerals* 43.4 (1995), pp. 427–432 (cit. on p. 75).
- [59] X. Zhang; L. Teng; Y. Liu; Z. Liu; J. Xue; M. Ikram; M. Ullah; L. Li; K. Shi. «3D flower-like NiZnAl multimetal oxide constructed by ultra-thin porous nanosheets: A long-term and stable sensing material for NO<sub>x</sub> at room temperature». In: *Sensors and Actuators B: Chemical* 300 (2019), p. 126899 (cit. on pp. 77, 80, 90).
- [60] G. Kang; Z. Zhu; B.H. Tang; C.H. Wu; R.J. Wu. «Rapid detection of ozone in the parts per billion range using a novel NiAl layered double hydroxide». In: *Sensors and Actuators B: Chemical* 241 (2017), pp. 1203–1209 (cit. on p. 77).
- [61] D.M. Xu; M.Y. Guan; Q.H. Xu; Y. Guo. «Multilayer films of layered double hydroxide/polyaniline and their ammonia sensing behavior». In: *Journal of Hazardous Materials* 262 (2013), pp. 64–70 (cit. on p. 78).
- [62] S. Morandi; F. Prinetto; M. Di Martino; G. Ghiotti; O. Lorret; D. Tichit; C. Malag; B. Vendemiati; M.C. Carotta. «Synthesis and characterisation of gas sensor materials obtained from Pt/Zn/Al layered double hydroxides». In: *Sensors and Actuators B* 118 (2006), pp. 215–220 (cit. on p. 78).
- [63] Q. Wang; X. Zhang; J. Zhu; Z. Guo; D. O’Hare. «Preparation of stable dispersions of layered double hydroxides (LDHs) in nonpolar hydrocarbons: new routes to polyolefin/LDH nanocomposites». In: *Chemical Communications* 48 (2012), pp. 7450–7452 (cit. on p. 78).
- [64] B. Wang; H. Zhang; D.G. Evans; X. Duan. «Surface modification of layered double hydroxides and incorporation of hydrophobic organic compounds». In: *Materials Chemistry and Physics* 92 (2005), pp. 190–196 (cit. on p. 78).
- [65] D. Hong; J. Zhang; A.U. Rehman; L. Gong; J. Zhou; K. Kan; L. Li; K. Shi. «One-step synthesis of hierarchical Ni-Fe-Al layered double hydroxide with excellent sensing properties for NO<sub>x</sub> at room temperature». In: *RSC Advances* 6 (2016), pp. 103192–103198 (cit. on pp. 78, 79, 87–89).
- [66] D. Hong; J. Zhang; A.U. Rehman; L. Gong; J. Zhou; K. Kan; L. Li; K. Shi. «Stable Suspension of Layered Double Hydroxide Nanoparticles in Aqueous Solution». In: *Journal of the American Chemical Society* 128.1 (2006), pp. 36–37 (cit. on p. 78).

- [67] E. Bormashenko; Y. Bormashenko; M. Frenkel. «Formation of Hierarchical Porous Films with Breath-Figures Self-Assembly Performed on Oil-Lubricated Substrates». In: *Materials* 12 (2019), p. 3051 (cit. on p. 79).
- [68] S.A. Kandjani; S. Mirershadi; A. Nikniaz. «Inorganic-Organic Perovskite Solar Cells». In: (2015), pp. 223–246 (cit. on p. 80).
- [69] Shlomo Magdassi. *The Chemistry of Inkjet Inks*. 5 Toh Tuck Link, Singapore 596224; USA office: 27 Warren Street, Suite 401-402, Hackensack, NJ 07601; UK office: 57 Shelton Street, Covent Garden, London WC2H 9HE: World Scientific Publishing Co. Pte. Ltd., 2010. Chap. 1 (cit. on p. 81).
- [70] S. Khan; L. Lorenzelli; R. S. Dahiya. «Technologies for Printing Sensors and Electronics Over Large Flexible Substrates: A Review». In: *IEEE SENSORS JOURNAL* 15.6 (2015), pp. 3164–3185 (cit. on p. 81).
- [71] J. Xu; C. Zhong; C. Fu. «Novel method for printing high quality metal wires». In: *SPIE Newsroom* (2007) (cit. on p. 82).
- [72] *MicroFab Technote 99-02 Fluid Properties Effects on Ink-Jet Device Performance*. MicroFab Technologies. 1999. URL: [www.microfab.com/images/pdfs/technote99-02.pdf](http://www.microfab.com/images/pdfs/technote99-02.pdf) (cit. on p. 81).
- [73] F. Cavani; F. Trifir; A. Vaccari. «Hydrotalcite-Type Anionic Clays: Preparation, Properties and Applications». In: *Catalysis Today* 11 (1991), pp. 173–301 (cit. on p. 82).
- [74] T. Aradi; V. Hornok; I. Dekany. «Layered double hydroxides for ultrathin hybrid film preparation using layer-by-layer and spin coating methods». In: *Colloids and Surfaces A* 319 (2008), pp. 116–121 (cit. on p. 82).
- [75] L. Albiston; K.R. Franklin; E. Lee; J.B. Smeulders. «Rheology and microstructure of aqueous layered double hydroxide dispersions». In: *Journal of Materials Chemistry* 6 (1996), pp. 871–877 (cit. on p. 82).
- [76] S. Chakraborty; I. Sarkar; K. Haldar; S.K. Pal; S. Chakraborty. «Synthesis of CuAl layered double hydroxide nanofluid and characterization of its thermal properties». In: *Applied Clay Science* 107 (2015), pp. 98–108 (cit. on p. 82).
- [77] J. Huang; Z. Yuan; S. Gao; J. Liao; M. Eslamian. «Understanding Spray Coating Process: Visual Observation of Impingement of Multiple Droplets on a Substrate». In: *Journal of Shanghai Jiaotong University (Science)* 23 (2018), pp. 97–105 (cit. on p. 83).
- [78] M. Eslamian; F. Soltani-Kordshuli. «Development of multiple-droplet drop-casting method for the fabrication of coatings and thin solid films». In: *Journal of Coatings Technology and Research* 15 (2018), pp. 271–280 (cit. on p. 83).
- [79] R.C. Tucker. «Introduction to Coating Design and Processing». In: *ASM International* 5A (2013), pp. 76–88 (cit. on pp. 83, 84).

- [80] B. Moore; E. Asadi; G. Lewis. «Deposition Methods for Microstructured and Nanostructured Coatings on Metallic Bone Implants: A Review». In: *Advances in Materials Science and Engineering* (2017) (cit. on p. 84).
- [81] J.J. Bravo-Suarez; E.A. Paez-Mozo; S.T. Oyama. «Review of the Synthesis of Layered Double Hydroxides: A Thermodynamic Approach». In: *Quimica Nova* 27.4 (2004), pp. 601–614 (cit. on pp. 84, 85).
- [82] M.L. Parello; R. Rojas; C.E. Giacomelli. «Dissolution kinetics and mechanism of MgAl layered double hydroxides: A simple approach to describe drug release in acid media». In: *Journal of Colloid and Interface Science* 351 (2010), pp. 134–139 (cit. on p. 85).
- [83] P. Zhou; Y. Wang; C. Xie; C. Chen; H. Liu; R. Chen; J. Huo; S. Wang. «Acid-etched Layered Double Hydroxides with Rich Defects for Enhancing the Oxygen Evolution Reaction». In: *Chemical Communications* 53 (2017), pp. 11778–11781 (cit. on p. 85).
- [84] A.W. Musumeci; T.L. Schiller; Z.P. Xu; R.F. Minchin; D.J. Martin; S.V. Smith. «Synthesis and Characterization of Dual Radiolabeled Layered Double Hydroxide Nanoparticles for Use in In Vitro and In Vivo Nanotoxicology Studies». In: *The Journal of Physical Chemistry* 114 (2010), pp. 734–740 (cit. on p. 86).
- [85] Z. Cao; L. Xue; M. Wu; B. He; J. Yu; M. Chen. «Effect of etched Layered double hydroxides on anti ultraviolet aging properties of bitumen». In: *Construction and Building Materials* 178 (2018), pp. 42–50 (cit. on p. 86).
- [86] W. Zhou; Z.L. Wang. *Scanning Microscopy for Nanotechnology Techniques and Applications*. 233 Spring Street, New York, NY 10013, USA: Springer Science+Business Media, LLC, 2006. Chap. 1 (cit. on pp. 86, 87).
- [87] G.H. Michler. *Electron Microscopy of Polymers*. Springer, 2008. Chap. 3 (cit. on p. 87).
- [88] H. Ibach; H. Luth. *Solid-State Physics An Introduction to Theory and Experiment*. Springer-Verlag, 1990. Chap. 3 (cit. on p. 88).
- [89] M.A. Mohamed; J.Jafaar; A.F. Ismail; M.H.D. Othman; M.A. Rahman. «Fourier Transform Infrared (FTIR) Spectroscopy». In: *Membrane Characterization* (2017), pp. 3–29 (cit. on p. 89).
- [90] H. Luth. *Solid Surfaces, Interfaces and Thin Films*. Springer-Verlag, 2010. Chap. 6 (cit. on p. 89).
- [91] W.H. Grover. «Interdigitated Array Electrode Sensors: Their Design, Efficiency, and Applications». MA thesis. University of Tennessee Honors Thesis Projects, 1999 (cit. on pp. 90–92, 95, 97).

- [92] Y.G. Song; Y.S. Shim; S. Kim; S.D. Han; H.G. Moon; M.S. Noh; K. Lee; H.R. Lee; J.S. Kim; B.K. Ju; C.Y. Kang. «Downsizing Gas Sensors based on Semiconducting Metal Oxide: Effects of Electrodes on Gas Sensing Properties». In: *Sensors and Actuators B* 248 (2017), pp. 946–956 (cit. on p. 91).
- [93] M. Ibrahim; J. Claudel; D. Kourtiche; M. Nadi. «Geometric parameters optimization of planar interdigitated electrodes for bioimpedance spectroscopy». In: *Journal of Electrical Biomedicine* 4 (2013), pp. 13–22 (cit. on p. 93).
- [94] *AZ nLOF 20xx Negative Resist*. MicroChemicals. URL: [https://www.microchemicals.com/micro/az\\_nLof\\_20xx\\_additional\\_informations.pdf](https://www.microchemicals.com/micro/az_nLof_20xx_additional_informations.pdf) (cit. on p. 104).
- [95] *Processing of AZ Negative Resists*. MicroChemicals. URL: [https://www.microchemicals.com/technical\\_information/negative\\_resist\\_processing.pdf](https://www.microchemicals.com/technical_information/negative_resist_processing.pdf) (cit. on p. 105).
- [96] M. Richetta; L. Digiamberardino; A. Mattoccia; P.G. Medaglia; R. Montanari; R. Pizzoferrato; D. Scarpellini; A. Varone; S. Kaciulis; A. Mezzi; P. Soltani; A. Orsini. «Surface spectroscopy and structural analysis of nanostructured multifunctional (Zn, Al) layered double hydroxides». In: *Surface and Interface Analysis* (2016), pp. 1–5 (cit. on p. 111).
- [97] Vigna et al. «The effects of secondary doping on ink-jet printed PEDOT:PSS gas sensors for VOCs detection (submitted)». In: (2020) (cit. on p. 118).